THE UNIVERSITY *of* EDINBURGH

Polydispersity effects on colloidal phase transitions and kinetic arrest

Siobhan M. Liddle

Doctor of Philosophy
The University of Edinburgh
2014

Abstract

I have studied the effects of polydispersity in systems of hard-sphere, colloidal PMMA particles with and without short-range attraction.

In hard-sphere, colloidal systems, the parameter controlling phase behaviour is ϕ, the volume fraction of colloids in the solvent. As ϕ increases in polydisperse systems, theory predicts a transition from a single phase fluid to a fluid coexisting with a solid (crystal), to a fluid coexisting with multiple solid phases. By considering a volume fraction series of particles with 12% polydispersity and comparing the results with previous experimental results and predictions of the volume fractions within the coexistence regions, we concluded that this system may be exhibiting both fluid-solid and fluid-solid-solid behaviour within the experimental coexistence region.

Theory also predicts that coexisting phases in polydisperse hard-sphere systems will fractionate: they will contain different particle size distributions (psds). This was investigated by directly measuring psds for one sample within the coexistence region at different time points. The results show that no statistically significant size fractionation was present after 28 days but by 120 days the solid phase contained a slightly narrower distribution of larger particles than the coexisting fluid phase.

At ϕ higher than the coexistence region in this polydisperse system, the expected coexisting solids are not observed. Instead, a novel, non-equilibrium phase is present. The dynamics were probed using 3-dimensional dynamic light scattering, which confirmed the non-equilibrium nature of the phase: significant dynamical heterogeneities and anomalous ageing behaviour were present. These experimental dynamics are compared with dynamics obtained from simulations of different hard-sphere psds, including the experimental particle size distribution.

The effect of adding a short-range, depletion attraction to a polydisperse colloidal

system was systematically explored. Phase boundaries and the position of the metastable gas-liquid binodal were determined experimentally. The resultant phase diagram topology is qualitatively different to a system of monodisperse particles with the same attraction range. Furthermore, within the metastable binodal region, three-phase gas-liquid-solid samples were observed, which is neither an equilibrium or metastable state in monodisperse systems. The coexisting samples were again characterised using electron microscopy and also small-angle x-ray scattering, which revealed significant size fractionation in the gas-liquid separated samples but not in the samples which eventually crystallised.

Lay Summary

A "colloid" is the general term to describe a particle with a size on the order of 1 nanometre to 10 microns in size. The particles used in this study are made of a solid polymer, suspended in a solvent, creating a colloidal suspension. Colloidal suspensions are useful as they display a lot of the same physics as atomic systems, whose constituents are too small to study directly, but they also have interesting physics of their own.

In this thesis I limit my study to uncharged, spherical colloidal particles. First, I investigate the behaviour of the colloidal suspension when the concentration of particles is varied. The state of the system is controlled just by the fraction (of the total volume) of particles in the suspension, f. Increasing f, identical particle suspensions transition from a well-mixed colloidal fluid, to two phases consisting of a fluid and an ordered crystal phase. Next with increasing volume fraction, a fully ordered crystal phase is observed and above 58% of particles, a colloidal glass phase is observed.

In this thesis I consider how these phases are changed when, instead of having identical particles, a range of particle sizes are used. The particles have a distribution of sizes, with an average diameter of approximately 300 nm. In this case, the fully ordered phase no longer appears; I observe evidence for both arrested and fluid-like, mobile particles. Furthermore, I observe phase behaviour consistent with the system attempting to reach an equilibrium of a fluid coexisting with multiple solid phases, which has not been experimentally verified until now.

I then consider the different phases that occur when the particles are attracted to one other over small distances. The phase diagram of observed phases is significantly different when the particles have a range of sizes compared to identical particles: new phases are observed and even the known phases occur in different regions of the diagram.

A challenge in this work was carefully measuring the sizes of the particles in different phases, so I describe my method of extracting sizes from electron microscopy images and how these compare to average size measurements from other methods, such as x-ray scattering. The new phases and behaviour I investigated in this thesis are a direct consequence of the distribution of sizes in the colloidal suspension; my work highlights the importance of measuring size distributions in research involving colloidal particles.

Declaration

I declare that this thesis was composed by myself, that the work contained herein is my own except where explicitly stated otherwise in the text, and that this work has not been submitted for any other degree or professional qualification except as specified.

The candidate confirms that the work submitted is his/her own, except where work which has formed part of jointly-authored publications has been included. The contribution of the candidate and the other authors to this work has been explicitly indicated below. The candidate confirms that appropriate credit has been given within the thesis where reference has been made to the work of others.

Parts of this work have been published in [61] [123].

(*Siobhan M. Liddle, 2014*)

Chapter 6 was based on reference [61]: S.M. Liddle, T. Narayanan and W.C.K. Poon, *Polydispersity effects in colloid-polymer mixtures*, published in the Journal of Physics: Condensed Matter in April 2011. I performed all of the experimental work except the initial characterisation by SAXS of the particles, which was performed by T. Narayanan.

The discussions at the end of section 5.3 are based on reference [123]: E. Zaccarelli, S.M. Liddle and W.C.K. Poon *On polydispersity and the hard-sphere glass transition* (submitted). I provided the experimental size distribution used in the simulations and was closely involved in discussions with E. Zaccarelli during her time in Edinburgh to ensure the simulations were comparable with the experimental system we were trying to understand.

Acknowledgments

Thanks to everyone. There are too many people to thank individually, but a few need a special mention:

For the academic support, encouragement and advice throughout my PhD, thanks to my supervisor, Wilson Poon, and also to Paul Clegg and Rosalind Allen. Thanks to Andy Schofield for making such interesting particles and both Andy and Job Thijssen for useful experimental advice and discussions.

To my collaborators, Emanuela Zaccarelli, Marco Laurati, Stefan Egelhaaf and Theyencheri Narayanan, thanks for some excellent trips and interesting discussions.

Thanks to my office-mates, past and present, particularly Diarmuid, who has been lucky enough to sit behind me for almost my entire PhD - thank you for answering many stupid questions, proof reading and procrastination. Thanks also go to all those with whom I've tutored, had coffee, lunchtime conversations and everyone who made cake on Fridays.

Thanks to Nick and all my family and friends for their support throughout, even when they had no idea what I was talking about.

Finally, thanks to my mum for all of the support, love and encouragement from the very beginning.

Contents

Chapter 1

Introduction

1.1 Colloids

Products with colloidal constituents are prevalent in everyday life, including milk, paint, ink, and cosmetics. A colloid is a particle with a lengthscale of the order of a few nanometers to a few microns; a particle which undergoes Brownian motion.

Brownian motion has been long studied, since Robert Brown's experiments on pollen grains in the early 19th century [14]. Brown observed random motions of small particles ejected from pollen grains suspended in water. In order to discern the source of the erratic motion, Brown studied first pollen from different species, preserved and dried plants, then later any material from which he could obtain small 'molecules'[1]. He concluded that, while he did not understand the source, the motion was universal to these small particles and not due to evaporation of the water. Later, Perrin utilised Brownian (colloidal) particles to determine Avogadro's constant, confirming Einstein's statistical analysis of molecular motion, thus precipitating a change of paradigm to the current modern atomic theory [27, 76].

An interesting feature of colloids is that they experience colloid-colloid interactions as well as Brownian motion, so experience phase changes with increasing concentration of particles, analogous to the phase transitions in atomic systems. This has provided a driving force behind much of colloidal research, as, in contrast to atoms, colloidal particles have lengthscales large enough that they can be

[1]These materials included minerals, metals, hair and a fragment of the Sphinx.

directly visualised. Furthermore, timescales of colloids tend to be slow enough that previously inaccessible atomic mechanisms, such as crystal nucleation, can be directly investigated.

To use colloids to model atomic systems, the particles should be ideally identical hard spheres. This is possible in theoretical models but experimental particles have an inherent polydispersity - they are not identical. A small degree of variation does not lead to significant deviations from theoretical monodisperse behaviour, but eventually the particles' polydispersity will have some effect on the behaviour of the system.

1.2 Polydispersity

Polydispersity is a dimensionless measure of the variation of some feature, for example, particle size, charge or shape. Since phase behaviour is controlled primarily by particle concentration, it is perhaps obvious that having a distribution of particle sizes within the system will have an interesting effect on phase behaviour; the geometry of the packing of the spheres will be markedly different from that of identically-sized particles. Furthermore, the dynamics of the smallest and largest particles may differ to an extent great enough to have an effect on the average dynamics of the whole system.

The effect of size polydispersity on hard sphere phase behaviour and dynamics has been studied experimentally in this thesis and will be presented in the order outlined below.

1.3 Thesis Layout

Chapter 2 first introduces hard spheres and theoretical phase behaviour, and the way this is realised in experimental colloidal systems. Methods of adding attraction to the system are discussed and the resultant experimental and theoretical attractive phase diagrams are presented, including a discussion of equilibrium and non-equilibrium behaviours.

Polydispersity is discussed in chapter 3, starting with a general introduction, then a review of the known effects of size polydispersity on phase behaviour in hard-

sphere and attractive hard-sphere colloidal systems. This chapter also includes a discussion of binary colloidal systems, the most basic example of a 'polydisperse' system, and a description of various distributions commonly used to describe size-polydisperse particle distributions.

Chapter 4 contains the experimental methods and techniques used within this thesis: basic colloidal experimental techniques, light (and x-ray) scattering theory and experimental setup, and transmission electron microscopy.

Chapters 5 and 6 contain the main experiments and results. The experiments in chapter 5 investigate the effects of size polydispersity on hard-sphere colloidal systems. Distributions of particles in phase separated samples have been carefully measured using transmission electron microscopy to discover any possible segregation of particles by size (fractionation) between coexisting phases. The last part of this chapter regards a new, non-crystallising phase, discovered at high volume fractions. The dynamics of this phase were probed using dynamic light scattering.

The work of chapter 5 is extended in chapter 6 by the addition of attraction to polydisperse hard spheres. The complete phase behaviour was mapped and the new phases, not present in an equivalent monodisperse system, are discussed. Possible fractionation in coexisting phases was again explored using both transmission electron microscopy and small-angle x-ray scattering. A method to compare directly the results of these two techniques was developed and is described in this chapter.

Finally, conclusions and routes for future work can be found in chapter 7.

Chapter 2

Colloidal Physics

> First of all, we must note that the universe is spherical.
>
> *Nicolaus Copernicus*

2.1 Hard Spheres

Condensed matter studies liquids and solids. In the atomic world, liquids and solids have a density of approximately 1 amu per unit (atomic) volume, so the simplest possible model for a condensed matter system is one which the particle shape a configuration of impenetrable (hard) spheres.

Hard spheres are still an active research topic. Figure 2.1 shows the results of a search for "hard AND spher$*$" in the Web of Knowledge core database, where the $*$ enables alternative suffixes to the word "sphere" to be included in the same search. The results show that the output of reasearch on this topic increased rapidly between 1955 and 1990 and has remained at an almost steady rate since the mid-1990s. A hard sphere with radius R is one which experiences the simple potential illustrated in figure 2.2: infinite at a distance $r = 2R$ and zero elsewhere. The simplicity of hard spheres lends them well to simulations [47, 89] and analytic theories [1].

For example, atoms and molecules can be modelled as spherical objects [8]. Considering a molecule as a sphere is obviously an oversimplification, however a lot of the important physics can be modelled and understood from the hard

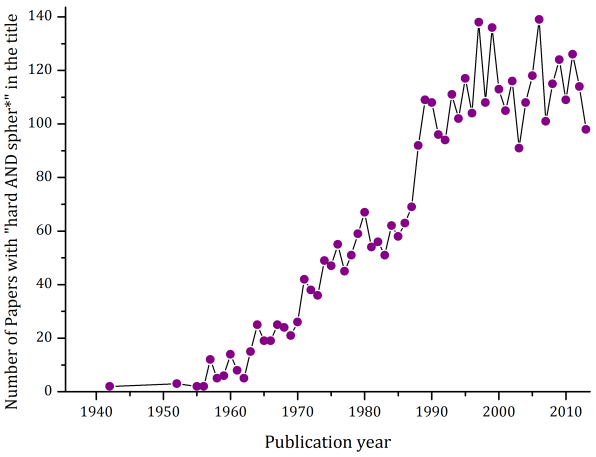

Figure 2.1 Number of publications with the words "hard sphere(s)" in the title per publication year, from 1930 to 2012. This data was extracted from Web of Knowlege's publication search analysis tool.

sphere model. Using hard spheres as a model for molecular liquids was first proposed by Widom in response to the failure of lattice gas models to predict any solid states [120]. The lattice gas model provides an excellent model for liquids near the critical point, where attractive forces dominate, however it does not contain any states with long range order. Widom noted that the treatment of forces in the lattice gas model did not allow any possibility of propagation of repulsive forces; this must be the origin of the failure of the model to contain a crystalline state.

In a dense liquid, *i.e.* near the triple point, attractive forces between molecules largely cancel because they are relatively weak compared to the short-ranged repulsive forces, which largely add [120]. Widom suggested that this means each molecule is situated within a deep, uniform, background potential. The depth of the background potential is proportional to the number of molecules, N, contributing to it, or the density of particles in the system, so simply contributes a term proportional to $(N/V)^2$ in the equation of state of the system ($p = [\delta F/\delta V]_T$). In other words, the equation of state mainly depends on the entropic part of the free energy, so molecular liquids can be effectively modelled by a (entropic) hard-sphere system.

In the atomic scenario, different states of matter can be conceptualised as arrangements of different numbers of spheres contained in a certain volume, as illustrated in figure 2.3. Gas (a) and liquid (b) phases are both spatially

homogeneous, disordered phases, so we can only distinguish between them if they are coexisting and there is a meniscus separating them [17]. Figure 2.3(c) shows a fully ordered, crystalline phase and figure 2.3(d) illustrates random close packing of identical spheres, which has a packing (volume) fraction of $\phi \approx 0.64$ [23].

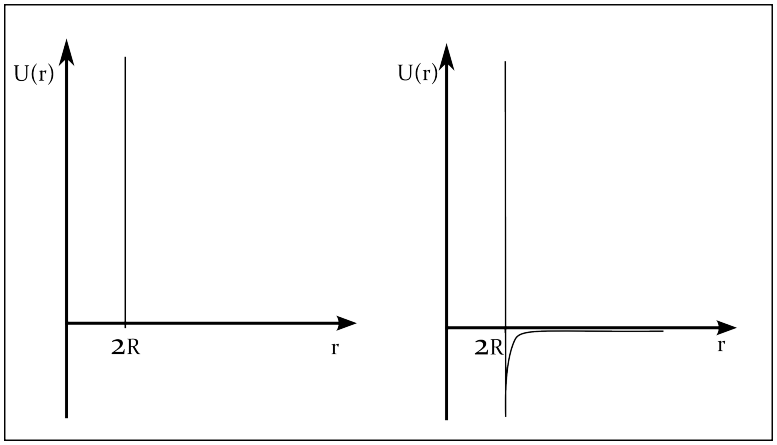

Figure 2.2 Hard Sphere potential (left) and with short range attraction (right).

Simulating hard sphere crystallisation was one of the first successes of modern computer simulations. Hoover and Ree performed simulations in 1968, concluding that above a packing fraction of $\phi = 0.545$, spheres prefer to arrange in an ordered crystal structure, rather than a disordered configuration [47]. Below $\phi = 0.494$, particles exist in a disordered fluid phase; when ϕ is between 0.494 and 0.545, fluid coexists with an ordered crystallising phase. The fraction of crystal in this region increases with increasing ϕ, until above $\phi = 0.545$ it is completely crystalline. It is entropically favourable to have an ordered structure at large packing fractions: the configurational entropy of the sphere decreases, but an ordered structure allows greater movement of the sphere around its lattice point, leading to an increase of the vibrational entropy.

Even the most groundbreaking theories and simulations cannot be verified without rigorous experimental testing.[1] Hard sphere systems can be experimentally realised using colloidal particles.

[1] At the time of writing, Peter Higgs, along with his collegue Francois Engelert, have recently been awarded the Nobel Prize in Physics for their contributions to the theory predicting the particle known as the Higgs Boson [45], thought to be the origin of mass in subatomic particles. They were only awarded the prize when the existence of the particle was experimentally verified, at much expense [16], almost 50 years after the initial theory was published.

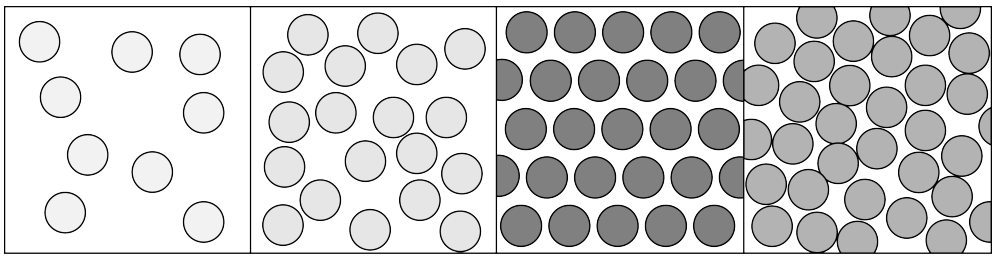

Figure 2.3 Illustrations of hard sphere arrangements: a) "Gas" and b) "liquid" are experimentally indistinguishable disordered phases unless they are coexisting with a meniscus between them, c) fully crystalline phase: $\phi > 54.5\%$, random close packing: $\phi = 64\%$.

Table 2.1 Colloidal suspensions can be classified by the combination of states of the particle and the dispersion medium. The particles used in this thesis are solid, dispersed in a liquid medium.

Particle type→ dispersion medium	gas	liquid	solid
gas		mist	aerosol
liquid	shaving foam	mayonnaise	ink
solid	expanded polystyrene	jelly	Ruby glass

2.2 Colloids

Although it is possible to perform experiments on the bulk properties of atomic or molecular materials,the small scale means that it is very difficult (but not impossible [46]) to visualise what is happening at the single atom level. Colloids are particles that experience Brownian motion and can be classified depending on which combination of states are present in the system. Illustrative examples of the different classifications of colloidal systems are noted in table 2.1.

Hard-sphere, solid colloids can be made from various materials. A synthetic latex is commonly used; the resultant particles have a tunable size, dependent on the growth method [12]. Furthermore, fluorescent dyes can be incorporated into the latex, which can be utilised in confocal microscopy to obtain three dimensional images [15]. Colloidal suspensions are useful models for atomic systems because they can be easily designed to have the appropriate state [79], experiments are readily accessible at ambient conditions, and the particles can be large enough to be visualised using optical microscopy.

In the argument for using hard spheres as a model for molecular liquids at the

start of this chapter, it was noted that the phase behaviour of dense liquids, which is dominated by long-range repulsive forces, can be effectively modelled using hard spheres, which have repulsive forces dependent on the excluded volume around each sphere [120]. The total excluded volume in a system of dilute, identical spheres is additive but as the number of spheres in the volume increases, the exclusion zones necessarily overlap. This leads to a smaller value for the total excluded volume than just the sum of the excluded volumes around each sphere. Therefore the configuration of particles dictates the total excluded volume and thus the volume fraction of particles in a hard-sphere, colloidal system is the only relevant parameter for determining phase behaviour.

2.2.1 Measuring volume fractions

Conceptually, the simplest method of measuring volume fraction would be to calculate the volume occupied by a number of particles of known size in a region of known volume. With confocal microscopy it is possible to track the positions of thousands of particle centres in three dimensions [26], so if the radius of each particle is known, the volume fraction can be calculated [57]. This method is of course limited by the size of the particles; those on the smaller end of the colloidal scale are too small to be accurately tracked using light microscopy. Furthermore, measuring the radii of particles is itself far from straightforward. This leads to large systematic errors and variation between measurement methods [12].

The experimental freezing behaviour of colloidal hard spheres was investigated by Pusey in colloidal samples in 1986 [88], confirming the phase behaviour encountered with increasing volume fraction. Using knowledge of the theoretical freezing and melting volume fractions of the crystal, ϕ_f and ϕ_m respectively, it is possible to measure the volume fraction of a crystallising sample: measurement of the fractional height of crystal allows immediate determination of the volume fraction, illustrated in figure 2.4, assuming the fraction of crystal increases linearly across the coexistence gap. This linear relationship follows from conservation of particle mass, when the volume fractions are known. Details of the calculation can be found in section 2.3.2.

The time taken for particles to crystallise depends on the difference of the volume fraction from ϕ_f (particles at higher volume fractions have a larger entropic driving force to crystallise), during which time the particles will sediment. Individual crystallites will be more dense than the surrounding bulk suspension

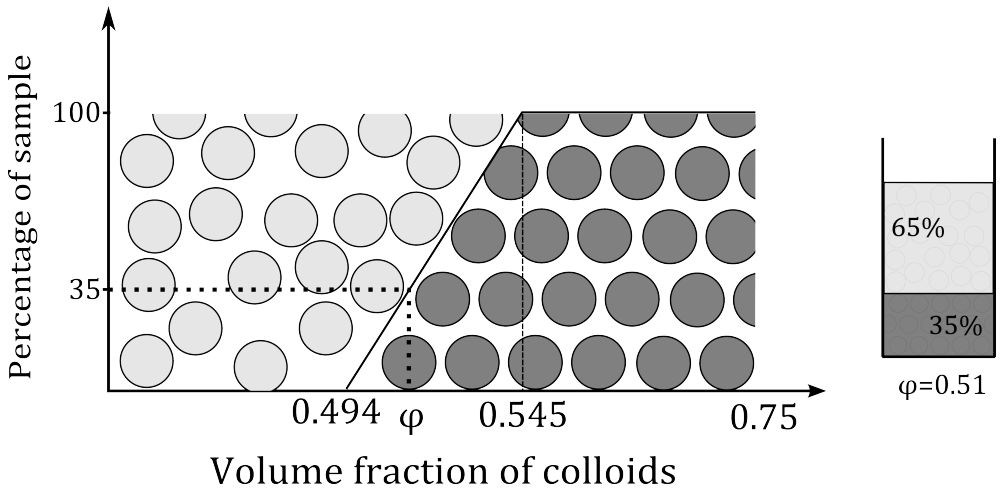

Figure 2.4 Phase behaviour of identical spheres with increasing volume fraction, predicted by simulation in 1968 by Hoover and Ree [47] and verified in colloidal experiments by Pusey *et al.* [88]. To the right of the phase diagram is a schematic example of a phase-separating sample with 35% crystal; the volume fraction is calculated to be $\phi = 0.51$.

and will settle to the bottom of the vial, eventually creating a measurable layer, the height of which will change over time. The bottom layer of particles may become compressed, creating a denser sediment below the crystalline layer. To properly calculate the fraction of crystal phase, it is necessary to measure the fractional heights of the crystal and bottom sediment over several days and extrapolate the heights [73]. Another issue, which makes this technique slow to implement, is the parent particles may not initially have a volume fraction within the coexistence region. Adjusting the volume fraction and waiting to see if the new sample crystallises can be a tedious process.

A closely related method, still utilising fluid-solid coexistence, is to prepare a series of samples with volume fractions equally spaced around the coexistence region. The fully crystalline sample that has the lowest volume fraction is identified and set as the upper boundary of the coexistence region; all other samples can then be calibrated from this point. One obvious limitation of both methods is it cannot by used on non-crystallising samples. Furthermore, the volume fraction must be determined before any experiments take place, thus it is not a good technique for individual samples or retrospective volume fraction measurement.

A method not limited by the crystallisation of particles is the centrifugation technique. Assuming the centrifuge spins at a rate fast enough that the particles are not able to rearrange and crystallise, the resulting particle sediment will

have a random close packed (rcp) configuration. If ϕ_{rcp} is known, the volume fraction of the particle suspension can then be readily calculated by measuring the fractional height of the sediment in the suspension. Unfortunately the value of ϕ for random-close-packed particle sediment is debated and depends on the experimental conditions [57]. Simulations also produce different values of ϕ_{rcp}, as it is dependent on the protocol used. Some researchers even take umbrage with the name, suggesting a true rcp state (where there is minimal ordering but the particles are maximally jammed, such that none can move) should be more accurately described as *maximally random jammed* [113].

Both of these height-measurement techniques rely on established knowledge of crystalline or random close-packed particle packings. While there is still some debate on the exact value of ϕ_{rcp} for uncharged, identical particles, the situation is complicated further when the particles are not identical in size or shape. Size polydispersity will be discussed in the next chapter, but packings of different shapes of particles is also an active area of research. It important to note that although the exact volume fraction of the calibration sample may have some systematic error, the relative volume fractions of the samples prepared subsequently will be very precise. Therefore one must be wary of making quantitative comparisons with published work, particularly if the authors have not disclosed their method of volume fraction determination.

The above methods were utilised for the experiments in this thesis, and the practicalities of doing so will be discussed in chapter 4. Another, more traditional technique is again in theory straightforward: one simply has to measure the weight of particles in suspension, then evaporate the solvent. This method is described in detail elsewhere [31] however, it too is flawed, as the particles may have different properties when dried than they have *in situ*.

Volume fractions can be further complicated if there is charge present, which depends on the method of particle stabilisation used. Different methods of stabilising particles are described in the following section.

2.2.2 Experimental Hard Spheres

Experimental hard spheres interact via a van der Waals attraction: an attractive force induced by fluctuating electron densities on the particles. Without stabilisation, this would lead to irreversible aggregation of the particles.

One method of stabilising particles is by grafting a layer of polymer hairs onto the surface of the particle *i.e.* steric stabilisation, as illustrated in figure 2.5(a). The length of the polymer hairs must be longer than the range of the van der Waals force, which depends on the combination of particle and solvent used (in particular, it depends on the Hamaker constants of each of these). The polymer for the stabilising layer is chosen such that the solvent is a "good solvent" for the hairs. In a good solvent, the polymer layer extends radially outwards from the surface of the particle. When two particles come together, the grafted polymer hairs overlap. This is energetically unfavourable - the hairs would rather be in the solvent than touching each other - resulting in a hard sphere repulsion. These types of particles have long been used, and are accepted to behave like theoretical hard spheres [88].

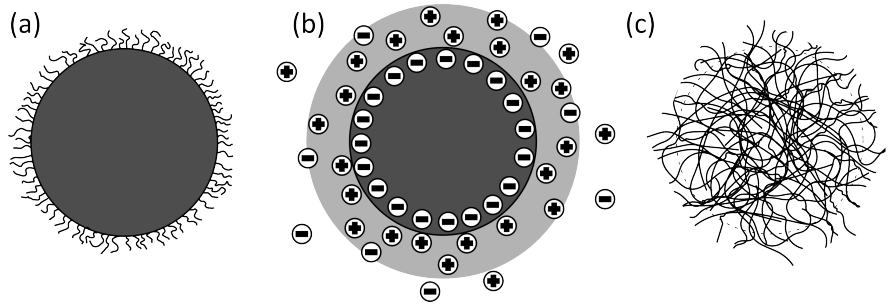

Figure 2.5 Schematic drawings of types of colloids used in experiments as models for hard spheres (a)Sterically stabilised particles with grafted polymer hairs. (b) Charged particles with an electrostatic double layer (light grey), which needs to be screened in order to approximate a hard-sphere potential. (c) Microgel particle, consisting of crosslinked polymer.

It is not always practical to use steric stabilisation. Simple hard sphere particles, such as polystyrene, are often charged. Such charge creates an electrostatic double layer around the particle, illustrated in figure 2.5(b), leading to long range repulsion. To proceed with hard sphere models, the charge must be screened by adding a salt. This must be tuned carefully, because too much screening will expose the van der Waals minimum, resulting in attraction.

Without screening of the electrostatic double layer, charged colloidal systems crystallise at a much lower volume fraction than $\phi = 0.545$. Charged colloidal crystals can be easily identified in micrographs by their large interparticle spacing, an example of which can be see in figure 2.6.

The third type of particle, shown in figure 2.5(c), are microgel particles, which consist of heavily crosslinked polymers. The particle radii are tunable by changing the solvent properties: In a good solvent, polymers are extended and the radius

Figure 2.6 An example of a low volume fraction ($\phi = 0.02$), charged colloidal crystal, with the characteristically large spacing (26.7 μm) between particles observed in charged systems. Taken from [122].

is large, while in a poor solvent, the polymer chains collapse onto one another, reducing the effective radius. This system has the covetable advantage that the volume fraction can be controlled by the temperature (since solvent quality is affected by temperature), reducing the need to create a new sample for every volume fraction point in phase space. Unfortunately, with tunability comes softness [106]; microgel particles are the least accurate approximation to hard spheres of the three examples outlined above.

Royall *et al.* recently wrote a comprehensive review on the search for the perfect hard sphere [94]. They conclude that charge is difficult to avoid, even in steric systems, particularly if the particles are large enough for confocal microscopy. Therefore, the system with the fewest components which best approximates hard spheres is small, sterically stabilised particles suspended in a good solvent (for the stabilising hairs). This is the system used for the experiments in this thesis.

Once a good hard-sphere system has been established, it is then possible to extend phase space in another dimension by adding attraction. Methods of controlling the range and depth of this attraction are discussed in the following section.

2.3 Attractive phase behaviour

2.3.1 Depletion attraction

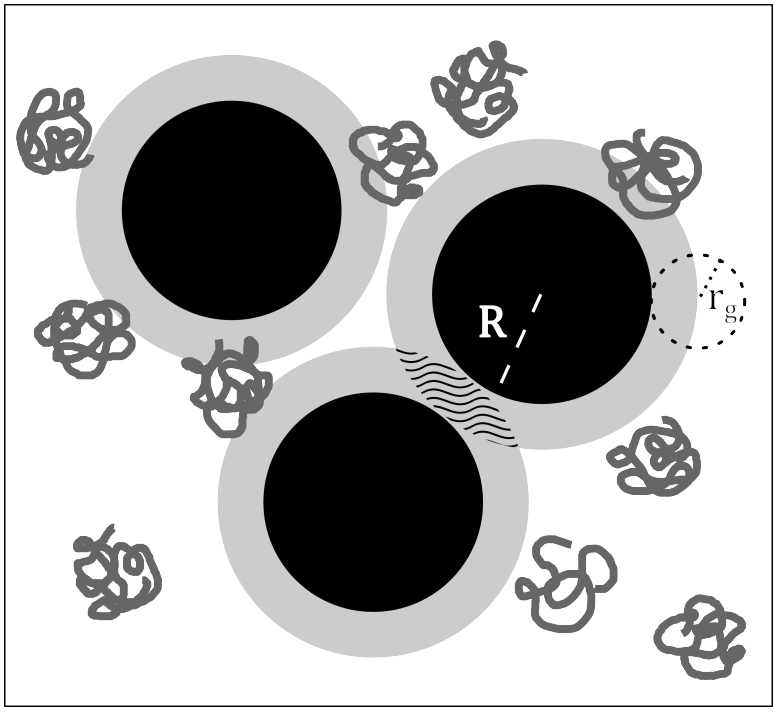

Figure 2.7 Colloidal particles (black) of radius R and polymers with a radius of gyration r_g. The centres of the polymers are excluded from a region around each particle (grey). When two exclusion regions overlap (wavy lines), there is an imbalance of osmotic pressure between the particles compared to the rest of the free volume, creating an effective attraction.

In sterically stabilised particle systems, it is common practice to introduce attraction into the system by adding a depletant. This is illustrated in figure 2.7; polymer coils with a small radius of gyration, r_g, are added to the particle suspension. The centres of the polymer coils are excluded from a region around each particle. Thus when two particles come close to one another, the overlap of the excluded volumes from each particle creates a region in which no polymer can enter, the resultant imbalance of osmotic pressure around the particles results in the particles coming together. An alternative way to visualise this concept is to think of the polymer randomly hitting the surface of the particles. The polymer can push against the particles at all points except those in the overlap region; there is, on average, more force pushing the particles together than apart, leading to an effective attraction. The range of this attraction is controlled by the radius of the polymer, while the depth (strength) of the attraction is controlled by

changing the concentration of polymer, c_p. Phase diagrams are usually plotted in terms of c_p (or osmotic pressure, Π) *versus* ϕ.

The osmotic pressure is calculated using the concentration of polymer in the free volume, c_p^{free}, rather than the concentration of polymer in the entire volume, c_p. The free volume fraction, α, can be easily calculated to be

$$\alpha = 1 - \phi(1+\xi)^3, \tag{2.1}$$

where $\xi = r_g/R$ is the ratio of sizes of the polymer and colloid. We can now derive an expression for the osmotic pressure of the polymer solution.

Van't Hoff's law states that, equivalently to the ideal gas expression [54], the osmotic pressure is proportional to the number density of polymer in the free volume, n_p:

$$\Pi = n_p k_B T, \tag{2.2}$$

where k_B is Boltzmann's constant and T is the temperature of the solution. n_p can be easily related to known and measurable quantities:

$$n_p = \frac{N_p}{V_{free}} \tag{2.3}$$

$$= \frac{N_A}{M_w}\frac{c_p}{\alpha}, \tag{2.4}$$

so:

$$\Pi = \frac{N_A}{M_w}\frac{c_p}{\alpha}k_B T. \tag{2.5}$$

N_A and k_B are Avogadro's number and Boltzmann's constant respectively and M_w is the average molecular weight of the polymer. Equation 2.5 is of course an approximation: in practice neither the polymer or colloid are dilute. As the concentration of polymer increases, the contribution of overlapping coils must be taken into effect. However, typical concentrations of polymer in colloid-polymer phase diagrams are low - lower than the polymer overlap concentration, $c^* = \frac{3M_W}{4\pi N_A r_g^3}$ - so the dilute polymer approximation of equation 2.5 is still valid.

However, as the concentration of colloids increases, the free volume α has to take into account overlapping exclusion regions. The free volume can be obtained by comparing expressions for the chemical potential of a test hard sphere according

to Widom [120] and that from scaled particle theory [59, 91]:

$$\alpha = (1-\phi)\exp\left[-A\gamma - B\gamma^2 - C\gamma^3\right], \tag{2.6}$$

where $\gamma = \phi/(1-\phi)$, $A = 3\xi + 3\xi^2 + \xi^3$, $B = 9\xi^2/2 + 3\xi^2$ and $C = 3\xi^3$.

Equation 2.6 then allows for a more accurate analysis of the polymer concentration in colloid-polymer mixtures. The concentration of polymer in the free volume is directly related to the polymer chemical potential, μ_P:

$$c_p^{free} = \frac{c_p}{\alpha} = exp[(\mu_P - \mu_P^0)/kT], \tag{2.7}$$

where μ_P^0 is a reference chemical potential [60]. The chemical potential in all coexisting phases must be equal, thus tie-lines joining coexisting phases in the $c_p^{free} - \phi$ representation are horizontal (figure 2.8(a) to (c)). On the other hand, the concentration of polymer in coexisting phases need not be equal, hence tie-lines in a $c_p - \phi$ phase diagram (figure 2.8(d) to (f)) will be slanted. The statistical mechanical approach resulting in equation 2.6 still requires approximations to the free volume and assumes dilute polymers, but phase diagrams calculated using this agree reasonably well with experimental phase behaviour [83].

With a robust description of the strength of the depletion attraction in colloid-polymer mixtures, we can turn to the effect on equilibrium phase behaviour of the range of the attraction. There exist three regimes of equilibrium phase behaviour, characterised by the size ratio, $\xi = r_g/R$, where R is the average radius of the colloidal particles. For small range, adding attraction simply increases the range of volume fractions at which fluid coexists with solid (crystals), illustrated in figure 2.8(d). At the intermediate range, figure 2.8(e), the liquid phase starts to become stable and the triple line is present; finally 2.8(f) shows long range attraction, where gas-liquid separation is dominant at low polymer concentrations.

An alternate visualisation of the phase diagram is to consider the polymer concentration in the free volume, as depicted in figure 2.8(a) to (c). The phase boundaries are horizontal in this case and the three-phase triangle in figures 2.8(e) and (f) is a three-phase line in figures 2.8(b) and (c). These equilibrium phase diagrams were calculated using the method of reference [60]. The basis of this common tangent method is that the free energy, $F = U - TS$ has a minimum for each phase at equilibrium. By plotting free energy density, $f(\rho) = F/V$ as a

function of the density of each phase, the minima can be connected by a straight line, the tangent of which is the chemical potential and the intercept with the y-axis is the osmotic pressure in the system [31, 54]. Ilett and coworkers provided an experimental example in each of the three attraction regimes, confirming the topology of the theoretical phase diagrams [52].

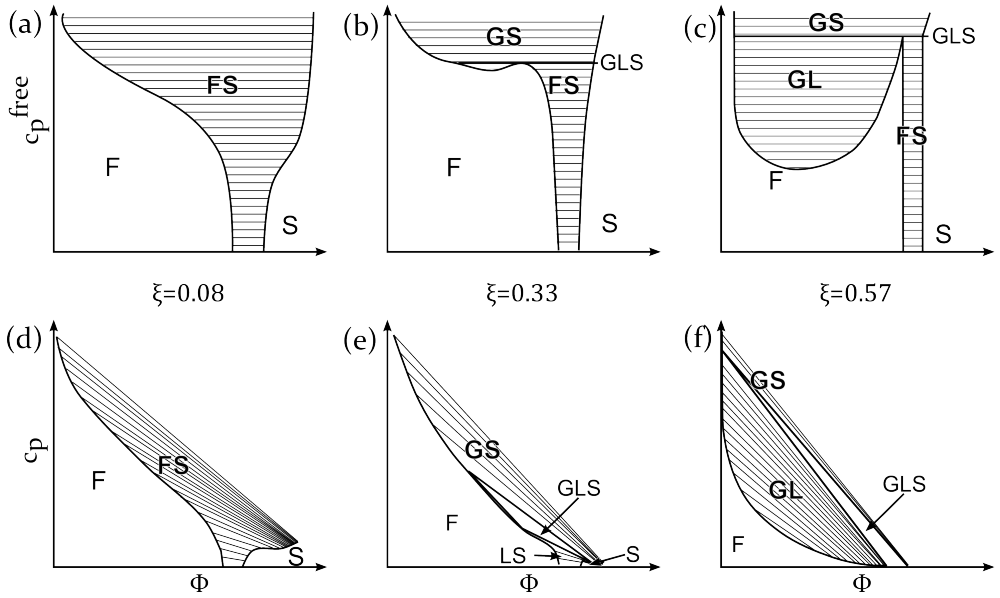

Figure 2.8 Theoretical phase diagram topologies of colloid volume fraction against the free polymer concentration, in figures (a) to (c), and the measured polymer concentration in the total volume, in figures (d) to (f), calculated according to the method in [60]. Tie-lines joining coexisting phases are horizontal in the top row but are tilted in the experimental $\phi - c_p$ diagrams. Figures (a) and (d) are those for low size ratio, where the equilibrium phases are fluid (F), fluid+solid (FS) and crystal (S). The middle column is for intermediate size ratios, where a stable liquid starts to appear; here there are distinct liquid (L) and gas (G) fluid phases, each coexisting with a crystal phase, as well as a three phase gas-liquid-crystal (GLS). Finally, figures (c) and (f) are for high size ratio, where gas-liquid separation is a prominent equilibrium phase. Redrawn from [52].

These three regimes of phase diagram topologies are generally accepted in the colloid-polymer community [39], although the exact size ratio where the behaviour switches from being low range to intermediate is still debated. The theoretically predicted crossover size ratio is $\xi = 0.3$ [41], while experimentally it is found to have a lower value, $\xi = 0.24$ [52].

The attractive phase behaviour presented in chapter 6 uses polymer with radius less than 10% of the colloid radius, well within the short range regime.

2.3.2 Lever Rule

Predicting equilibrium phase boundaries is complex [39, 52]. However, the lever rule provides us with a method of relating volume fractions of coexisting phases with their fractional volumes [11, 43], so if, for example, the volume fraction of each phase and the fractional composition of each is known, points on the phase boundaries can be determined. The lever rule is derived from the basis of particle conservation: take a sample with N particles of volume V_p in total volume V_T and initial volume fraction ϕ_T, which separates into two phases with volume fractions ϕ_a and ϕ_b. Particle number conservation tells us:

$$\begin{aligned} N &= N_a + N_b \\ NV_p &= N_aV_p + N_bV_p \\ \phi_T V_T &= \phi_a V_a + \phi_b V_b \\ \phi_T &= \phi_a f_a + \phi_b f_b, \end{aligned} \tag{2.8}$$

where f_a and f_b are the fractional volumes of phases a and b. This equation can be rearranged to give an expression relating the measurable fractional volumes with the volume fractions of each phase:

$$\frac{f_a}{f_b} = \frac{\phi_b - \phi_T}{\phi_T - \phi_a}. \tag{2.9}$$

Equation 2.9 can be used to determine the volume fraction of each phase when the fractional heights are easily measured and hence the phase boundaries. Conversely, if the the volume fraction of each phase is known, the fractional volumes can be calculated. An example putting equation 2.9 to use in the case of a short-range attractive colloid-polymer mixture can be seen in figure 2.9. In this scenario, the particles separate into a crystalline phase and a liquid phase, which are clearly separated by an interface. The initial volume fraction and volume fraction of each phase is known, and by measuring the fractional heights of each phase, points on the phase boundary can be calculated. Coexisting phases are joined by tie-lines in the phase diagram.

The lever rule can be generalised and used for samples where the sizes of each particle are not identical [53, 108], and is applicable in metastable phase separation.

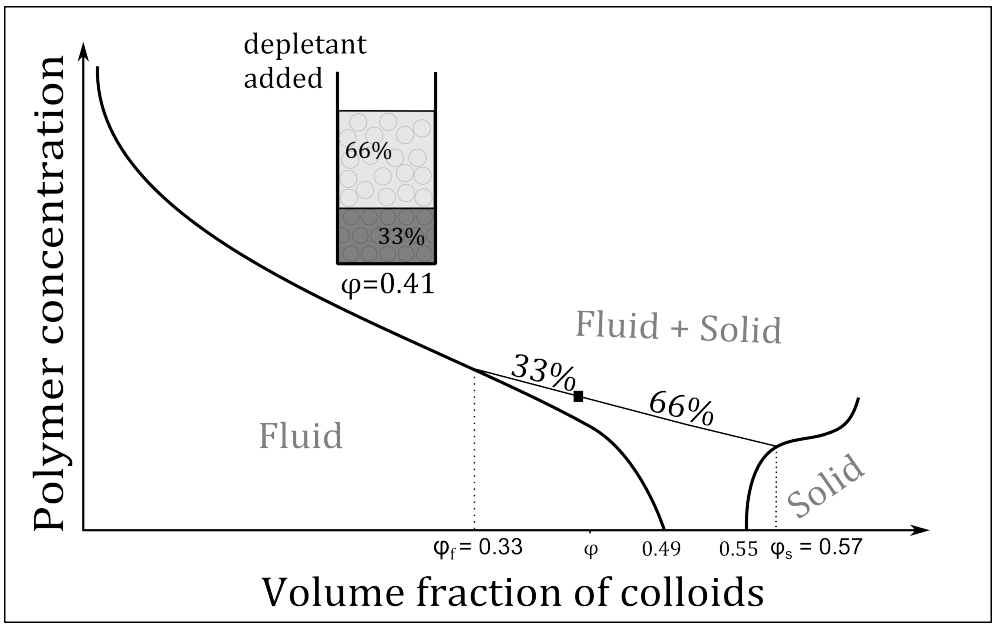

Figure 2.9 An example of the lever rule: if the volume fractions of fluid and solid phases, ϕ_f and ϕ_s, and the starting volume fraction ϕ are known, two points of the phase boundary can be determined. Using multiple samples, the entire phase boundary can be estimated [11].

2.3.3 Non-equilibrium features

As well as the equilibrium phases described above, which depend on the colloid volume fraction and polymer concentration and size, there are also non-equilibrium features that are often metastable and can prevent the equilibrium phases forming. The three most studied features in a short-range attractive system are illustrated in the schematic in figure 2.10 and are discussed below: the gas-liquid binodal, the colloidal glass, and gels.

Gas-liquid binodal

Phase behaviour is driven by the minimisation of the free energy of the system, which (in the free energy *versus* ϕ plane) has a fluid and a solid curve. As the concentration of polymer in the system increases, the free energy of the fluid develops a second minimum; the lowest free energy state is coexistence of two colloidal fluid phases with different volume fractions, which are usually given the labels of gas and liquid, in analogy to an atomic system.

In systems with small polymer, the free energy minimum of the solid curve is much lower than that of the coexisting gas and liquid, so, using the common tangent

method tells us the equilibrium state would be a coexisting fluid and solid [31]. The reason the gas-liquid coexistence persists (and hence its metastability) is that it would take a large fluctuation of the free energy to escape from the gas-liquid minima and reach the lowest free energy, equilibrium fluid-solid state.

Samples prepared in region A of the phase diagram (figure 2.10) separate via spinodal decomposition [54] into non-equilibrium gas and liquid phases. In region B, phase separation occurs through nucleation and growth of small droplets of gas or liquid phase, depending whether it is the low ϕ or high ϕ branch of the binodal [54].

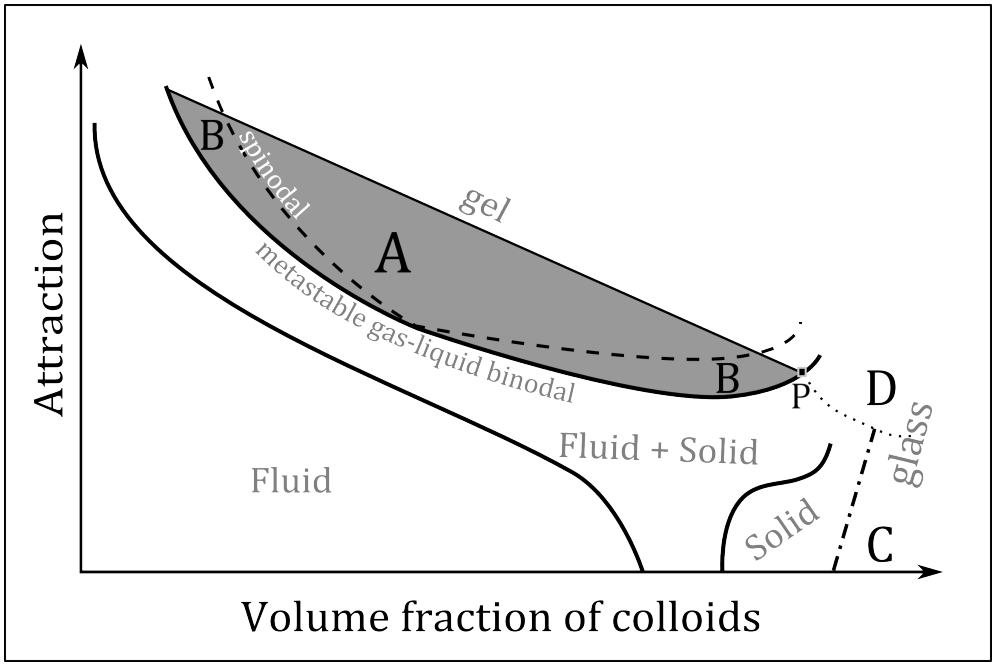

Figure 2.10 Regions of non-equilibrium behaviour in a colloidal system with a short-range attraction. See the text for a description of the regions *A*-*D*

Colloidal glass

At high volume fractions and low polymer concentration, region C of figure 2.10, the equilibrium phase is pure solid, so we expect the particles to crystallise fully. In fact, the volume fraction is so high that on experimental timescales the particles become arrested in a disordered, non-ergodic configuration known as a (repulsive) colloidal glass. Particles are surrounded by a cage of their neighbours; in order for large scale rearrangements, there must be cooperative motion or cage-hopping to melt the glass [54]. Addition of a short-range attraction to a glass first melts

it - the glass is re-entrant - then a different type of (attractive) glass is formed, region D [22]. In this case, the particles need not be so tightly packed to become arrested: even if a gap appears in the surrounding cage of neighbouring particles, the particle is attracted to its neighbours and is thus unable to escape.

There is some ongoing debate about whether colloids actually experience a glass transition. Evidence suggests that, above volume fractions of ≈ 0.58, colloidal particles show the slowing dynamics and ageing behaviour characteristic of a glass [89]. Others claim that they observe ergodic behaviour present at volume fractions above $\phi = 0.58$, which therefore precludes the existence of such a state [13]. In the last case, the use of particles with a distribution of sizes could be having unforeseen effects on the results. It turns out that our work throws light on this debate - see chapter 3.2.

Gels

The final type of non-equilibrium behaviour commonly found in short-range, attractive colloidal systems is a combination of the metastable gas-liquid binodal and the attractive glass. The tie-line ending at point P, where the phase boundaries meet, is the lower boundary of the colloidal gel [81]: an arrested, spinodal network that percolates through the system. These gels are characterised by their timescale of collapse, which has a particular shape [112].

Most of the concepts in this chapter are founded on the basis that the colloidal particles are identical in size. Experimentalists aim to use particles with as narrow a distribution of sizes as possible, but particle synthesis is a chemical process and is subject to stochasticity; this means there will inevitably be some size variation present in the particle suspension. While it is true that suspensions with a narrow distribution of particle sizes do not deviate from the theoretically predicted behaviour [83], there must be some limit where size variation does have an effect.

The experiments in this thesis use colloids with a significantly wide size distribution, which turns out to have qualitative effects on both hard-sphere (chapter 5) and attractive hard-sphere phase behaviour (chapter 6) compared to identical particle dispersions. The next chapter discusses the known effects of using colloidal particles with a distribution of sizes.

Chapter 3

Polydispersity

Polydispersity, σ, is defined as the standard deviation of a probability distribution, normalised by its mean. In mathematical statistics, this quantity is known as the coefficient of variation, which perhaps better describes its meaning - it is a dimensionless measure of the degree of variation in a distribution.

Variation is ubiquitous in nature and colloidal suspensions are no exception to this. For example, a batch of colloidal particles will have some distribution of radii. The polydispersity of the size distribution can be calculated using equation 3.1:

$$\sigma = \frac{\sqrt{\langle R^2 \rangle - \langle R \rangle^2}}{\langle R \rangle}, \tag{3.1}$$

where the triangular brackets denote the average over all N particles in the particle size distribution: $\langle R\ rangle = \frac{1}{N} \sum_{i=1}^{N} R_i$.

Size polydispersity is not a feature limited to colloidal physics. It appears in varied examples such as the physics of comet formation, where the size distribution of the 'cometesimals' have a large effect on the cohesiveness of the comet [58], or at the other extreme of magnitude where separation of small-scale carbon nanotubes is complicated by size and charge dispersity [63, 125]. Another example is in circulating fluidizing bed technology [19], which is a way of transporting suspensions of solid, granular, particles in a fluid or gas. Chew *et. al.* recently investigated the effect of size distribution on the formation of these particle clusters and found that those samples with narrower distributions formed smaller

clusters. Furthermore, a distribution consisting of two discrete peaks behaved differently from the continuous polydisperse distribution [19]. Chew noted that "a predictive understanding of the impact of polydispersity remains elusive ... which can lead to poor performance and undesirable flow behaviour".

This last example highlights the fact that, when a large degree of polydispersity is present, a lack of understanding can impact on the interpretation (and prediction) of results. However, even though in many cases polydispersity is an unwanted complication, it can also precipitate interesting and novel behaviour.

3.1 Polydispersity in hard-sphere colloids

Equal sized hard spheres, introduced in section 2.1, undergo phase transitions dependent solely on their volume fraction, ϕ. Colloidal particles with narrow size distributions have been used successfully in experiments to confirm the theoretical freezing behaviour of hard spheres [88], but what effect does a wider size distribution have on this system? Three general concepts are relevant for discussing the phase behaviour: phase boundaries, the slower kinetics and eventual termination of crystallisation, and fractionation, where coexisting phases have different size distributions. While these ideas are not independent of each other, I will discuss them separately in the following sections.

3.1.1 Phase boundaries

The phase behaviour of monodisperse hard spheres, discussed in section 2.1, can be summarised thus: as the volume fraction of the particles increase, entropy dictates that the most efficient packing for $\phi > 0.545$ is an ordered, crystalline lattice. Between $\phi_f = 0.494$ and $\phi_m = 0.545$, a colloidal crystal at $\phi = 0.545$ coexists with a fluid at $\phi = 0.494$, the fraction of crystals being proportional to $(\phi - \phi_f)$, as illustrated in figure 2.4. When $\phi < 0.494$, the particles exist as a disordered fluid.

Polydisperse phase behaviour is more difficult to predict, due to the increased degree of complication of the free energy, which must be minimised and solved to find volume fractions of coexisting phases. The full free energy depends on all of the details of the distribution; the free energy is a non-linear function of

the moments of the density distribution and, although solutions can be found in principle using computational algorithms, it is apparently nontrivial to generate an initial point from which the algorithm will converge [107]. Furthermore, there is not a straightforward geometric interpretation of the resultant phase diagram using the full free energy [107].

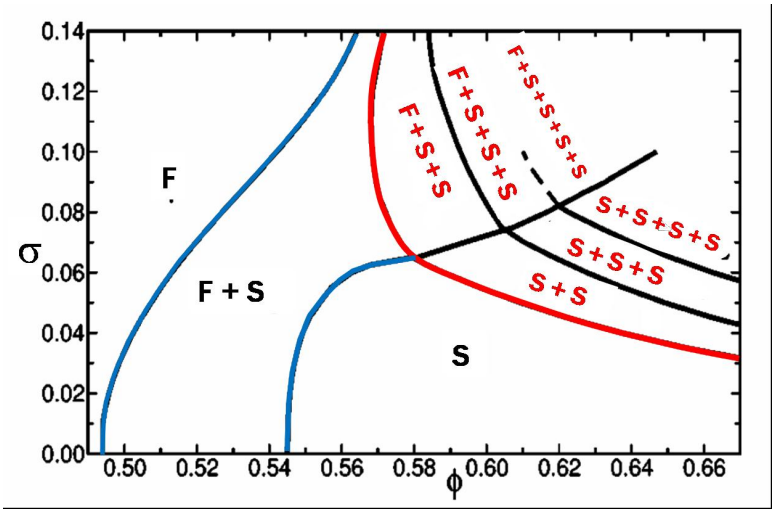

Figure 3.1 Effect of increasing polydispersity (vertical axis) on crystallisation volume fractions (horizontal axis) in hard-sphere mixtures from[33]. F+S denotes coexisting fluid+solid phases and S+S+..etc indicated multiple coexisting fractionated solids. Redrawn from [107].

The moment free energy (MFE) method, used by Fasolo and Sollich [34], addresses these problems by mapping the full free energy of the system to a free energy which depends only on a finite number of moments of the distribution and is therefore finite and exactly solvable for the onset of phase coexistence. Including a greater number of moment densities in the free energy allows for the possibility of more coexisting phases. For the interested reader, further details of this method can be found in references [34, 35, 107]. The results of the MFE calculations of Fasolo and Sollich are illustrated in figure 3.1. As the polydispersity increases the fluid stays stable to higher volume fractions, with an eventual narrowing of the fluid-solid coexistence region, but the width of this region remains approximately constant for polydispersities $< 6\%$. This was in contrast to a previous theoretical approach based on the geometry of the system. Bartlett predicted that, as the polydispersity of the particles increased, the width of the FS coexistence gap would decrease; when $\sigma = 8\%$, the volume fractions of the coexisting fluid and solid would be equal [4].

An important feature of the MFE method is that it allows for fractionation. In particular, for particles with polydispersities $\sigma > 7\%$ in figure 3.1, multiple

solids with different size distributions are present in all predicted phases with volume fractions $\phi > 0.58$. Sollich and Wilding continued this work, using both MFE calculations and Monte Carlo simulations [121]. Their simulations agreed qualitatively with MFE calculations, predicting no significant narrowing of the FS coexistence gap and significant fractionation in coexisting phases. Furthermore, experiments performed to measure the width of the FS coexistence region by Fairhurst [31] did not reveal any significant narrowing of the coexistence region with increasing polydispersity.

While Sollich and Wilding believe they have pinned down the true equilibrium behaviour, they admit that it may not be attainable in experimental systems [109]. Indeed, multiple, coexisting solid phases have not yet been observed in systems with polydisperse distributions, possibly due to the slow crystal nucleation and kinetics in polydisperse systems [102, 103].

3.1.2 Crystallization kinetics and terminal polydispersity

The MFE calculations discussed in the previous section (and illustrated in figure 3.1) predicted that all hard-sphere particle systems with polydispersities up to 14% undergo fluid+solid coexistence. The higher ϕ phases are predicted to be either multiple coexisting solids, or a fluid coxisting with multiple solids. However, multiple coexisting solids have not been observed in experimental polydisperse systems. The equilibrium phase behaviour supports crystallisation; the lack of crystallisation observed in experiments must therefore come from a kinetic source. There has been some interest in the nucleation kinetics of polydisperse hard spheres [2, 64, 102]. However, since the equilibrium multiple solid phases at high polydispersities are not observed, the experiments exploring polydisperse nucleation kinetics have necessarily had to utilise particles with relatively low polydispersities.

Martin *et. al.* presented crystallization kinetics for two polydisperse hard-sphere suspensions in 2003 [64]. The particles were made of a copolymer latex which is tunable in such a way as to index-match the suspending solvent, allowing application of scattering methods to characterize and study the particles. The particles were measured to have polydispersities of 4 and 6.8%, as fit by a Gaussian and Weibull distribution respectively. The lower polydispersity system first appears to act like the monodisperse model, crystallizing in the expected way, but above $\phi = 0.56$, where the particles are expected to be fully crystalline, they

no longer show any crystallization. The particles with the higher polydispersity were reported to have crystals coexisting with a fluid for a smaller range of volume fractions, between 0.52 and 0.56, but again no crystals were observed for volume fractions above $\phi = 0.56$. In light of the knowledge of the predicted equilibrium hard-sphere phase boundaries, it is probable that the "4%" sample is in the region of the phase diagram close to (but below) 6%, where the expected phase behaviour with increasing particle concentration is F $\rightarrow$ FS $\rightarrow$ S $\rightarrow$ SS, while that at "6.8%" would be F $\rightarrow$ FS $\rightarrow$ FSS. This would account for the reported lack of crystallization at high volume fractions in both cases, since we do not expect that experimental systems can separate into multiple coexisting solids, regardless of the presence of a fluid. So it is likely that the decreased nucleation kinetics of the crystals in the FS region of the 6.8% sample is an intrinsic feature of polydisperse crystallization, and not due to the system attempting to form multiple crystal phases.

A later, more systematic, study by Schöpe *et. al.* in 2006 considered the effect of particle polydispersity on the crystallization kinetics of hard spheres [102]. They studied three polydispersities in the range of 4.8 and 5.8%, as characterized by electron microscopy. The crystallisation kinetics were measured using Bragg scattering techniques, and they observed the striking result that by increasing the polydispersity by 1%, the main nucleation event is delayed by an order of magnitude. The larger polydispersity samples also contained a larger number of crystals with a smaller average crystal size than those in suspensions with a lower polydispersity.

Simulations have also been performed to explore polydisperse nucleation. Auer and Frenkel in 2001 [2] compared the free energy barrier for crystal nucleation for particles with a range of polydispersities, from monodisperse to 10%. They do not report the specific size distribution used but they do find that, up to 5% polydispersity, the system acts almost identically to the monodisperse case. Above 5%, increasing the polydispersity increases the crystal nucleation free energy barrier, *i.e* crystals are less likely to be able to form. Auer and Frenkel also observe that the coexisting fluid and solid phases have different distributions of particles, with the crystal phase containing more of the larger particles. They conclude from this work that the fact that crystallisation is not seen for polydispersities above 12% is because the nucleation energy barrier is too high and crystals are highly unlikely to form. This in turn suggests that glass phases with polydispersities above 12% should be truly amorphous, rather than

microcrystalline.

Terminal polydispersity

A sizable proportion of the early work on polydisperse hard spheres was dedicated to trying to predict at what polydispersity hard spheres stopped crystallising - the terminal polydispersity, σ_t. A simple criterion for crystal melting in atomic substances was proposed by Lindemann in 1910 [62]. The melting of a crystal structure can be explained by considering the vibrations of atoms: as the temperature of a crystal increases, the amplitude of the vibrations increase. At some point, when T is high enough, these vibrations cause an atom to enter the lattice space of its nearest neighbours, disrupting the lattice and initiating melting.

Pusey used a hard sphere model based on the Lindemann melting criterion to impose a maximum polydispersity on the particle size distribution [86]. A lattice with nearest neighbour centre-to-centre separation, L, will be disrupted when a significant number of particles have radii $> L/2$. This leads to a condition for the maximum polydispersity (of a symmetrical distribution) of $\sigma_t = (0.74/\phi)^{1/3} - 1$. Assuming the most dilute crystal possible has $\phi = 0.545$, this equation gives a maximum polydispersity of the crystal of $\sigma_t = 0.11$. If we increase the value of the most dilute crystal to $\phi = 0.58$, which is the highest possible volume fraction of a polydisperse crystal according to Fasolo and Sollich [33], then Pusey's approach implies that the maximum polydispersity of the distribution for crystallisation is $\sigma_t = 8.5\%$.

Other techniques for estimating the terminal polydispersity have been attempted. Results ranged from a value of 30% for a triangular distribution by Dickinson and Parker in 1985 [25] to a density functional theory (DFT) approach of McRae in 1988 that predicted there would be no crystallisation above 5% [67]. Barrat and Hansen also used a DFT approach to calculate the crossing points of the coexisting crystal and fluid volume fractions [3]. Intuitively we expect the fluid to be stabilised with increasing polydispersity since the smaller particles can fit into the gaps between the larger. Conversely, the crystal volume fraction may decrease, since the lattice will have to accommodate a larger range of particles and thus will need to have larger spacing. Barrat and Hansen find a maximum polydispersity for a fully crystalline sample of 16% for a triangular distribution and 12% for a rectangular distribution, although a fluid coexisting with a crystal

was still predicted for polydispersities 5% above the terminal value for both of these. Simulations were later performed by Phan *et. al.* [78], who considered how polydispersity affects the crossing points of the volume fractions of random close packing and face-centred-cubic crystal packing. From this they found a terminal polydispersity of 12%.

Around the same time, both Bartlett [4] and Sear [104] used theoretical approaches, calculating the free energy of the crystal by a "geometric" approach and by cell theory respectively. Sear predicted a terminal polydispersity for a top-hat distribution of $\sigma_t = 8\%$, above this two solid phases with different fractions of particles were expected. Bartlett's calculations found a terminal polydispersity, above which the polydisperse fluid is the stable phase, also of 8%. More recent, and arguably more realistic, simulations by Wilding and Sollich [121] predicted that, above 6.9%, no coexisting fluid and crystal were possible. However, they emphasise that this does not necessarily indicate a terminal polydispersity, as they could not access higher polydispersites due to finite size effects in their Monte Carlo simulations. This last reference provides a good discussion on the comparison of different simulation techniques and deals with the possibility of fractionation in some detail.

In conclusion, it is evident that the kinetics of crystallisation in polydisperse samples are complex, and a consensus has not yet been formed, partially due to the difficulties associated with computing or calculating the phase behaviour.

3.1.3 Fractionation

In the discussions of shifting phase boundaries, slowing kinetics and termination of crystallisation in the previous sections, fractionation was often a factor in the calculations or theories. For example, in Bartlett's theoretical approach [4], coexisting fluid and solid phases were allowed to have different average size and polydispersity, although the distributions were constrained to have a Schulz shape. The fluid always contained smaller than average particles and smaller polydispersity than the coexisting solid phase but the differences in these values in both cases were very small.

In 2000, Bartlett [5] utilised the MFE method to examine the freezing behaviour of polydisperse hard sphere mixtures, by considering the difference between quenched *versus* annealed behaviour. In the quenched case, we assume that the

size distributions in the separate phases are equal. This has some justification, as in order for the different phases to have different populations of particles, the particles would need to self-diffuse on a large scale, which is a slower process than the crystallisation. Bartlett suggested that at long times, after initial crystallisation has taken place, the size distributions would relax into their annealed state where the particles can self-diffuse. In this instance we should observe fractionation of particles between the coexisting phases. At that time, the only experimental results showed that phase separated samples had similar size distributions [31]. In the experiments of chapter 5.2, the distributions of coexisting FS samples over the period of one month are measured to determine whether fractionation is present.

When size disperse systems phase separate, the coexisting phases can contain different distributions of particles. Fractionation is not limited to size polydisperse systems. It is possible for systems with distributions of, for example, charge or shape to fractionate, and in the low polydispersity limit it is expected that the degree of fractionation between the coexisting phases will obey a universal law [30]. A size-polydisperse particle suspension can separate into many coexisting phases [110], each of which may contain a different distribution of particles. In hard sphere experiments using polydisperse particles, the highest number of coexisting phases observed so far is two[1].

The quenched *vs.* annealed argument suggests that, given enough time, the coexisting phases will eventually contain distinct distributions of particles, but over what timescale would this fractionation occur? Multiple coexisting crystals having different crystal lattice parameters would involve large scale rearrangements of the particles into phases with different size distributions. While in theory coexisting multiple crystals are predicted to be the equilibrium state, on the timescale of experiments and the concentrations required it may not be possible in practice.

[1]Only coexisting fluid plus solid is observed on reasonable timescales (a few weeks) but bands of crystals do eventually form in particle suspensions left for very long times.

3.1.4 Measuring polydisperse volume fractions

Random close packing

Volume fraction is the most important parameter that needs to be considered when conducting research on hard-sphere particles. A simple and swift method of measuring the volume fraction of a colloidal suspension, as detailed in chapter 2.2.1, is to centrifuge the sample then use the random close packing volume fraction, ϕ_{rcp} and the height of the close-packed sediment to calculate the volume fraction of the sample. The effect of polydispersity here is to increase the density of random close packing. This makes intuitive sense; smaller particles will more easily fit into the gaps between larger particles. Desmond and Weeks recently recalculated values of ϕ_{rcp} for particles with various distributions and polydispersites [23]. They showed that for a polydispersity of $\sigma = 40\%$ the value of ϕ_{rcp} is increased to 0.66. The value of the random close packed volume fraction was shown not to depend sensitively on the type of distribution, however the skewness of the distribution can have just as large an effect as the magnitude of the polydispersity, as shown in figure 3.2.

Fluid-solid coexistence method

The fluid-solid coexistence method (section 2.2.1) is more complicated if we have polydisperse colloids. The method assumes that the melting and freezing volume fractions ($\phi_m = 0.545$ and $\phi_f = 0.494$) of the polydisperse colloid suspension are the same as those for the monodisperse case, and that the percentage of crystal increases linearly across the coexistence gap. Figure 3.1 suggests the width of the coexistence gap remains approximately constant for polydispersities up to $\approx 7\%$, while the tie-lines (not shown) are horizontal to $\approx 6\%$. So if a polydisperse sample behaves qualitatively the same as we would expect identical particles to, then it is probably safe to use the monodisperse techniques - any quantitative difference will be of the order of the error in the volume fraction. For systems with more extreme polydispersity, transparency of the determination of ϕ will allow recalculation in order to properly compare results with that of other research groups.

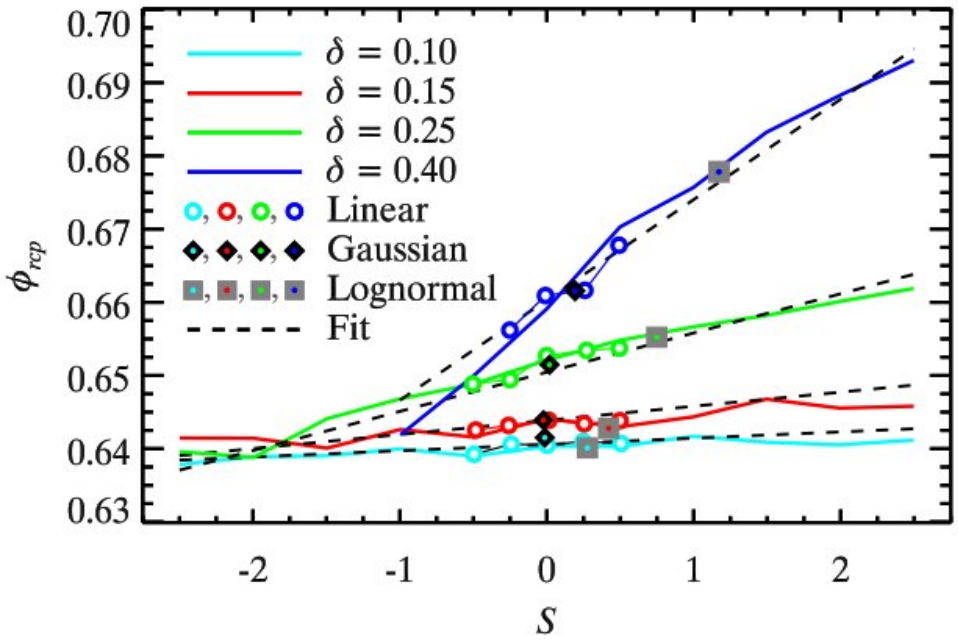

Figure 3.2 The dependence of ϕ_{rcp} on the size distribution, polydispersity, δ, and skewness, S. The symbols are calculated values for the various distributions indicated in the legend, while the solid lines represent ϕ_{rcp} for binary distributions with same overall polydispersity. The dashed lines are fits to a scaling model. Taken from [23].

3.2 Polydispersity and the Colloidal Glass transition

In order to use simulations or experiments to explore the colloidal glass transition in detail, it is desirable to avoid crystallisation of the particles. Since polydisperse systems are known to have slow crystal nucleation, they are an ideal candidate for a model system to probe dynamics of the glass transition, which occurs at volume fractions around $\phi_g = 0.58$. The problem is that polydisperse systems are yet to be completely understood, particularly in the regime of moderate polydispersity, where the particles are not observed to crystallise, despite the predicted equilibrium state of multiple coexisting solids [89]. The question of which observed features are a product of polydispersity alone, and which are pertinent to the glass transition, needs to be carefully addressed in any colloidal glass research utilising a polydisperse distribution of particles.

A recent example of the controversy, and the difficulties, surrounding this topic is the work by Brambilla *et. al.* [13]. They considered long-time dynamics of

a $\approx$ 10% polydisperse system using dynamic light scattering and compared it with Monte Carlo simulations of a binary hard-sphere mixture. Their results challenged the existence of a hard-sphere glass transition, with observations of fluid-like dynamics well above $\phi_g = 0.58$. It was thought that"activated processes" involving hopping of particles are instrumental in these systems avoiding the glass transition. Van Megen and Williams pointed out in a subsequent comment [68] that the extended regime of ergodic dynamics could be an effect caused by the polydispersity of the particles, not activated processes. The authors replied in a longer publication where they simulated particles with a top-hat polydisperse distribution [28]. They reported results compatible with their original experiments, discounting any effect of polydispersity on their results.

However, Zaccarelli *et al.* recently performed simulations using several different distributions at a range of polydispersities [123]. The resultant dynamics at high particle concentrations were reported to be very sensitive to the particular *shape* of the distribution - those with a tail of small particles exhibited on average the same behaviour observed by Brambilla, but when the large and small populations were considered separately it became apparent that the large particles exhibited the expected arrested behaviour at $\phi_g = 0.58$, while the small particles remained mobile. The mobility of these small particles brings about large deviations in the overall system, that were attributed by Brambilla to "activated processes".

This is just one recent example highlighting the ongoing debates in colloidal glass literature. The role of polydispersity on colloidal behaviour at high volume fractions needs to be studied before a complete understanding of the glass transition can be reached. Indeed, it seems even a simple choice of distribution shape can have unexpected, or overlooked, effects on hard-sphere behaviour. One might then expect an even richer range of phase behaviours when polydispersity is introduced to attractive hard-sphere systems.

3.3 Attractive polydisperse hard-sphere systems

A review of the effects of size polydispersity in colloidal systems would not be complete without considering the consequences of introducing attraction to a mixture of size-disperse colloidal particles. Very little research has intentionally been done on the addition of polymer to a polydisperse system, although the ever-present size dispersity of experimental particles means there are some clues

available to the effects. In chapter 6 the phase diagram of an experimental polydisperse system with short range attraction is presented, as well as a discussion of the various equilibrium and non-equilibrium features observed. The following section provides a review of the current literature on attractive, polydisperse hard-sphere systems.

3.3.1 Equilibrium phase behaviour

The three, range dependent, regimes of behaviour of attractive monodisperse hard spheres were summarised in figure 2.8. Theory suggests that the phase behaviour of polydisperse colloids plus polymer is richer than its monodisperse counterpart: Fasolo and Sollich have published schematics of predicted phase diagram topologies at the three attraction ranges, ξ, and three polydispersities, although they made detailed calculations only for size ratios in the long-range attractive limit [35]. Triangular distributions of particles were used and sketches of the predicted topologies for polydispersities of 5, 7 and 8% are shown in figure 3.3.

From figure 3.1, the polydispersity at which hard-spheres begin to exhibit qualitatively different behaviour from the monodisperse case is $\approx$ 6.5%; the polydispersities of the attractive systems studied by Fasolo and Sollich are just below and above this polydispersity of interest. The qualitative change in phase behaviour: the appearance of multiple solid phases, is reflected in the attractive phase topologies of figure 3.3. In all three regimes of attraction range, when the polydispersity is increased from 5 (bottom row) to 7% (middle row), the single solid phase (S) is replaced by multiple coexisting solids (SS). Furthermore, the widening of the fluid-solid (FS) coexistence region seen in the monodisperse regime disappears as the polydispersity increases. Instead, the 'next' phase is widened; either FSS for $\sigma = 7\%$, or $FSSS$ for $\sigma = 8\%$. The equilibrium, three-phase gas-liquid-solid behaviour is also affected; its region of stability increases with increasing polydispersity, even when the monodisperse phase diagram does not contain a two-phase gas-liquid. As the polydispersity increases, in order to accommodate multiple solid phases in the moderate and high attraction ranges, the number of solid phases in gas-liquid-solid phases also increases.

When the system undergoes gas-liquid or gas-liquid-solid phase separation, the coexisting phases are expected to have different distributions of particles. Fasolo and Sollich also made detailed calculations of coexisting gas-liquid phases

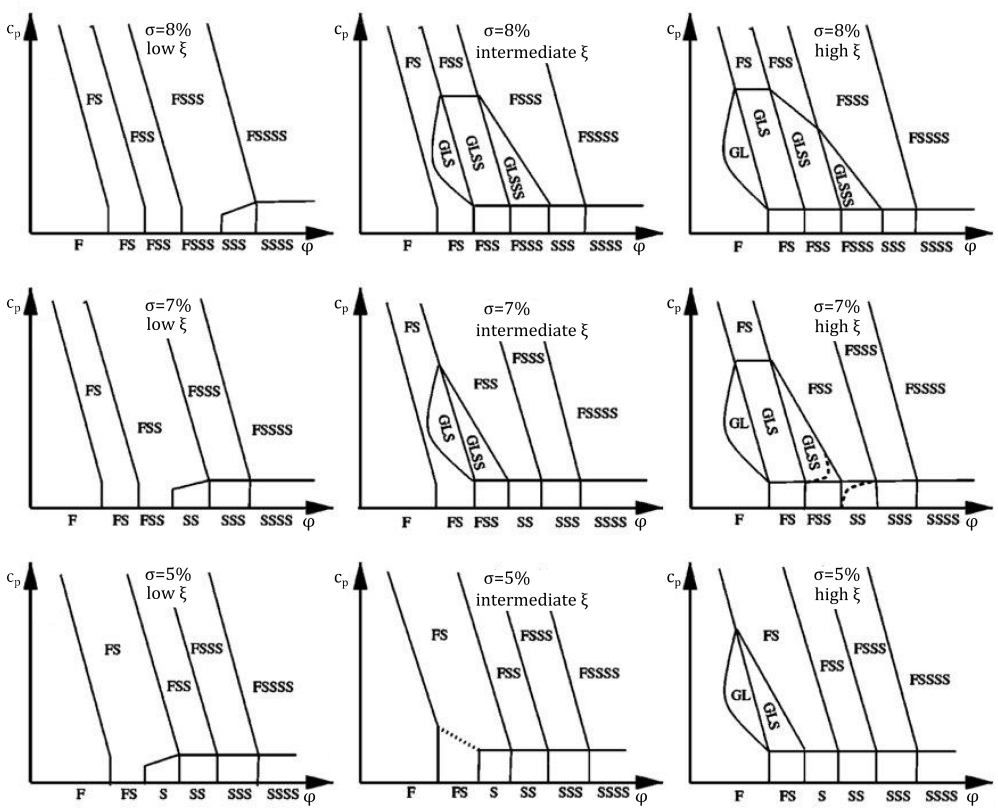

Figure 3.3 Sketches of theoretical phase diagram topologies for polydispersities $\delta = 5$, 7 and 8% and the three regimes of size ratio ξ, as labelled in the figure. F and S denote a single phase fluid and solid, respectively; the other phases are combinations of coexisting gas, G, liquid and multiple solid phases. Taken from [35].

at various polydispersities and attraction range $\xi = 0.45$ [35] to compare fractionation results with an experimental system [32]. The calculations followed the universal scaling law predicted in ref.[30] and were in reasonable quantitative agreement with their expected degree of fractionation.

3.3.2 Polydisperse polymer

The range of the attraction in a colloid-polymer mixture depends entirely on the radii of the depletant polymer and is usually quantified in terms of the relative range of the colloid and polymer radii: $\xi = r_g/R$, as discussed in section 2.3.1. Since the colloid polydispersity induces qualitative changes to the equilibrium phase diagram, it is pertinent to consider the effect of the polymer polydispersity.

Fasolo and Sollich performed calculations to determine the effect of polymer

polydispersity on the phase behaviour of colloid-polymer mixtures, concluding that polymer polydispersity only slightly affects the phase diagram topology [36]. This is in line with earlier calculations by Warren, who considered a colloid plus binary polymer system to study the effects of polymer polydispersity [118]. Both suggest that, similarly to polydisperse colloids, polydisperse polymers should fractionate between coexisting phases. However, unless the distribution of polymer sizes is wide enough, and fractionates in such a way that coexisting phases are in different regimes of phase behaviour, then we should not expect polymer polydispersity to have any qualitative effects on the phase behaviour.

3.3.3 Non-equilibrium features

The non-equilibrium features of gels and glasses for monodisperse colloids and low attraction range were discussed in section 2.3.3. Due to the increased complexity of the equilibrium phase diagram when the particles are polydisperse, the non-equilibrium features may also be affected. In figure 3.4, a schematic overlap of equilibrium phase boundaries for 7% polydispersity (according to figure 3.3) and binodal and glass lines for a short-range attractive colloidal system are shown. The intersection of the equilibrium and non-equilibrium phase boundaries could lead to novel behaviour within the binodal, region *a* of figure 3.4, as discussed below. The effect of polydispersity on the gel phase, region *b* of figure 3.4, is also discussed in the following section.

a. Metastable gas-liquid separation

As discussed in section 2.3.3, gas-liquid separation is a metastable state in short-range attractive colloidal systems. The free energy of the coexisting gas-liquid is higher than that of the equilibrium FS state, but a large, spontaneous fluctuation is needed to overcome the gas-liquid free energy minimum state, so the system remains as a gas-liquid over experimental timescales. This metastable binodal has has been observed in our experiments of a polydisperse colloid-polymer system [61]. In contrast to the monodisperse case, multiple types of phase behaviour are observed within the binodal, which we attribute to the intersection of the equilibrium FS/FSS boundary with the binodal. The experimental results will be presented in more detail in chapter 6.

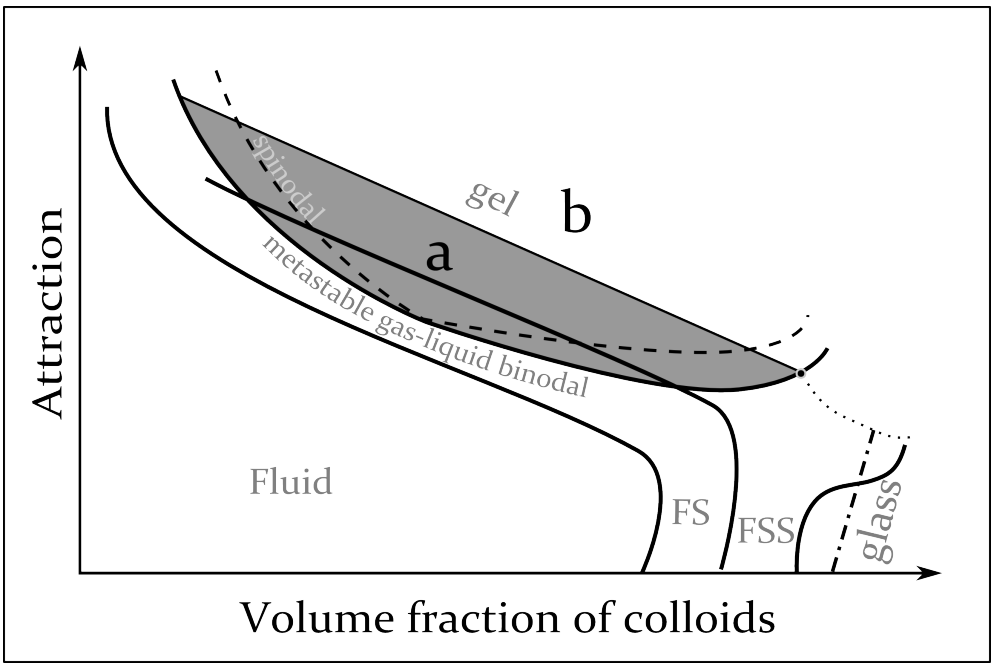

Figure 3.4 A sketch of a possible topology of a polydisperse system with short range attraction. The phase boundaries are an overlap of the theoretical equilibrium phase boundaries for particles with 7% polydispersity, according to fig. 3.3 and the non-equilibrium binodal and glass phases. FS denotes the equilibrium, coexisting fluid + solid phases, while FSS indicates the region where fluid is predicted to coexist with multiple solid phases. Consequences of polydispersity within the gas-liquid binodal (a) and gel (b) regions are discussed in the text.

b. Gels

Puretas and coworkers simulated a top hat distribution with polydispersity $\sigma = 17\%$, calculated using the expression for polydispersity in table 3.1 on page 41, to study the mean square displacements of particles near the gel transition [85]. They found heterogeneous dynamics not predicted by any theory: the 'small' population of particles had fewer neighbours and moved quickly, while the population of large particles had comparatively slower dynamics and more neighbours. Recent experiments by Zhang *et al.* to investigate the mechanism of gelation as the (long-range) attraction is changed, utilised 10% polydisperse particles, as measured by TEM. Their system exhibited the fast and slow heterogeneities predicted by Puretas' simulations, but Zhang *et al.* did not speculate whether the particle sizes were correlated with the dynamics [124].

This mixture of fast and slow behaviours seems similar at first glance to the dynamic heterogeneities seen in simulations at volume fractions near the poly-

disperse hard-sphere glass [123], although the Molecular Dynamics simulations of Coniglio [21] suggest the mechanisms giving rise to dynamic heterogeneities are different in gels and glasses. However, Conigilo *et al.* use only a small degree of polydispersity (randomly generated radii in a region of width $0.05R$ which implies a polydispersity of 1.5%), so size dependent heterogeneities are unlikely to be observed in their simulations.

The topic of colloidal gels is diverse and active. Understanding them is desirable for industrial research: shelf lives of many commercial products are dependent on how fast gels collapse and, for example, a layer of whey on top of a set yogurt is not inedible, but those yogurts that do not separate are aesthetically more appealing and more desirable to the consumer. Due to the ubiquity of size dispersity of the constituents of commercial products, it would be fruitful to explore the role of polydispersity with regards to the mechanisms of gel formation.

3.4 Binary Systems

Polydispersity of colloidal particles leads to some interesting features in both hard-sphere and attractive hard-sphere colloidal systems. However, part of the difficulty conducting a systematic experimental study of the effects of polydispersity is the difficulty of synthesising particles with a desired distribution. For this reason, some groups use instead a mixture of two (near) monodisperse suspensions in order to simplify the problem. This is not unreasonable; phase behaviour is controlled by the packing of the components, and Desmond and Weeks showed that binary distributions had random-close-packing volume fractions equivalent to those of continuous distributions with the same polydispersity [23]. Polydisperse distributions and binary distributions may be related, but it remains to be seen whether it is an oversimplification to approximate polydispersity with a binary model, or if the systems are fundamentally different.

The consistency of ϕ_{rcp} between binary and polydisperse distributions calculated by Desmond and Weeks does not necessarily mean that the dynamics of the systems will be equivalent. Taking the example of circulating fluidizing bed technology outlined at the beginning of this chapter [19], the experimental, binary distribution exhibited different behaviour to that of a continuous distribution of components. At what point do the details of the distribution become important in colloidal systems? To my knowledge, nobody has made a systematic study of

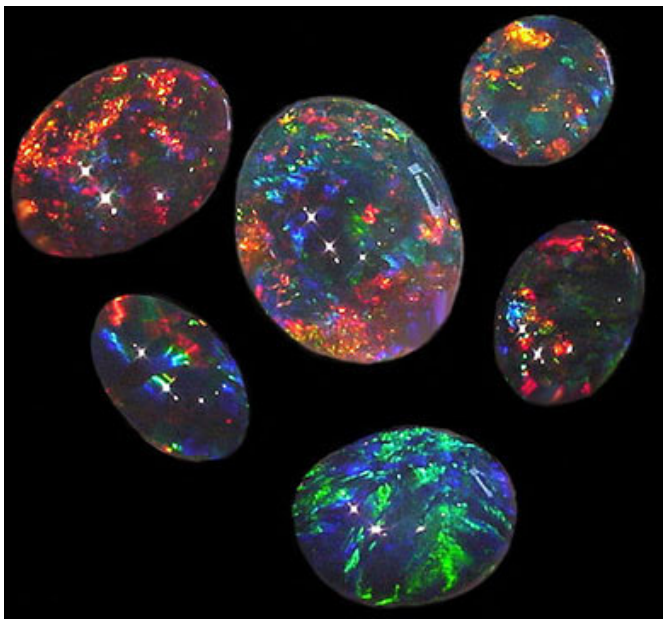

Figure 3.5 Photograph of black opals, a binary mixture of silica crystals, showing opals' characteristic 'play of colour' [119].

the applicability of using binary models to approximate polydisperse systems. In this section I will review some of the work in progress and point out areas where a systematic study might yield interesting results.

Binary systems are of course interesting in their own right; a specific example on the colloidal lengthscale is opals. Opals are made of a 3-dimensional binary 'superlattice' of silica particles. The gaps between the lattice planes are a similar length to the wavelength of light, and the different orientation of the crystal microstructures produce the striking 'play of colour' seen in opal gems (see figure 3.5). These binary superlattices were first observed in opals by Sanders in 1980 [95]. Binary colloidal distributions have also been proposed as a viable system for the self-assembly of photonic crystals: materials with an optical band gap, controlled by the length of the gaps between the lattice planes [20, 51].

3.4.1 Binary Colloidal Structures

Experimental studies of binary colloidal mixtures are abundant; the stability of superlattices in particular have received much interest. Superlattices are 3-dimensional crystal lattices with a mixture of large (L) and small (S) particles, for example LS_{13} and LS_2, with the same lattice structure of atomic $NaZn_{13}$

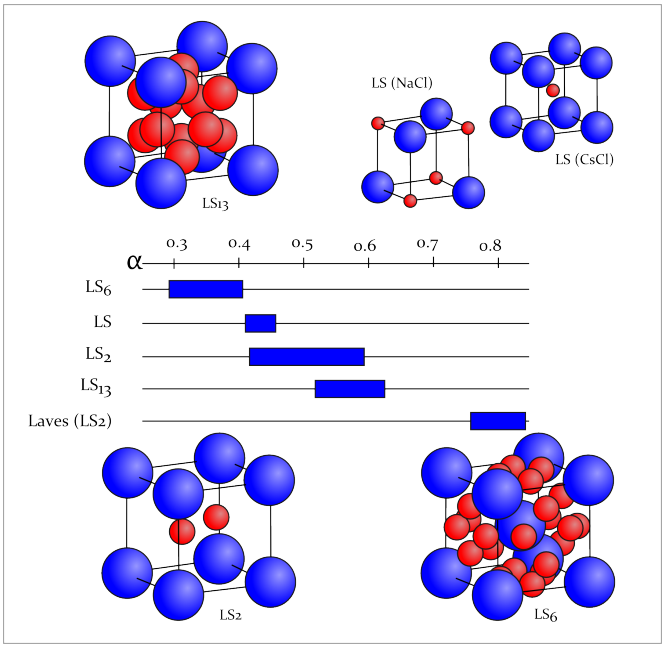

Figure 3.6 Range of stability of various different crystal structures, composed of large (L) and small (S) colloids, as determined by experiments [7, 49, 99] and predicted by theory and calculations [29, 38, 51].

and AlB_2 respectively. Some of the first experiments on colloidal binary crystal structures were performed by Bartlett *et al.* in 1992 [7]. They used a mixture of colloidal particles with size ratio $R_S/R_L = \alpha = 0.58$ and observed several crystal structures in different regions of the phase diagram, characterised by Bragg light scattering and scanning electron microscopy. More recent experimental studies have investigated the formation on stability of crystal structures over a wider range of size ratios, summarised in figure 3.6: *LS* crystals have been observed at $\alpha = 0.4$ [49], LS_2 structures are stable for $0.60 \gtrsim \alpha \gtrsim 0.425$ and LS_{13} for $0.62 \gtrsim \alpha \gtrsim 0.485$ [99] which broadly agree with the theoretical predictions and calculations [29, 38, 51]. Laves phases (eg $MgZn_2$) are predicted to be stable at high size ratios, $0.84 \gtrsim \alpha \gtrsim 0.76$ [38, 51], and these last, face centre cubic, superlattice structures have been observed in experiments using silver nanoparticles [55].

The most efficient packing structure for particular size ratios and compositions are yet to be completely understood. When making predictions based on packing fraction, different arrangements of each lattice type are found for different size ratios. For example, LS crystals of the type NaCl have been observed in experiments at size ratio $\alpha \sim 0.4$ [49], but at higher size ratios the LS crystal structure is expected to be of the type CsCl. Furthermore, in experiments

there are many regions where the particles do not crystallise as expected, but instead remain as an amorphous mixture [56]. This could be a feature relating to slow crystal nucleation kinetics due to the polydispersity of each component, or perhaps the system is attempting to make the large particle rearrangements necessary to form crystal superlattices. I made a detailed comparison of experimental and predicted binary phase diagrams. The results, in Appendix B, show that non-crystallisation often occurs near or in predicted eutectic (a fluid coexisting with two solids) regions, confirming for the first time a previous suggestion [7]. Understanding binary colloidal mixtures is an ongoing challenge, instrumental in the search for new materials and would help elucidate behaviour in materials such as metallic glasses.

3.4.2 An Application: Metallic Glasses

Metallic glasses are useful materials: they can be as strong as a crystalline metal but, due to their disordered structure, they are less prone to the mechanical stress problems that are governed by lattice defects (dislocations) in crystalline metals and alloys. Material properties of metallic glass vary depending on its constituents and a lot of the current research on metallic glasses is driven by the desire to understand this amorphous state [18]. One outstanding challenge is to find metallic glasses that can form without the need to quench the system very quickly. Early studies suggested that using a large range of elements is one way of forming a glass stable to crystallisation [75] and that the composition with the best glass forming ability is near, or at, the eutectic composition for the system [18, 75]. There is already some evidence that binary colloidal systems have low crystallisation ability near predicted eutectic compositions (Appendix B), and it is known that polydispersity also hinders crystallisation (section 3.1.2). Since packing of atoms is thought to be important in metallic glasses [70], it may be fruitful to use colloidal particles to study these systems.

The minimal number of components needed to create a metallic glass is two, and these materials are unsurprisingly known as binary metallic glasses (BMGs). A perhaps obvious hypothesis is that the glassy regions are analogous to those non-crystallising regions frequently seen in colloidal mixtures (see *e.g.* [7]). Miracle and coworkers recently completed a comprehensive review [71] on binary metallic glasses, quantifying the link between size ratio of the alloy constituents and glass forming ability. They collected data from 175 binary glass systems, with

628 alloys between them and found that there are only a few size ratios of the constituents which readily form glasses: of the 175 systems, all but 5 had size ratio $\alpha > 0.6$ with average size ratio $\alpha = 0.799$. Furthermore, it is believed that metallic glasses have some short to medium range order in the form of clusters [18, 70] which are packed densely in the system. Recent electron diffraction techniques, coupled with molecular dynamics simulation on binary $Zr_{66.7}Ni_{33.3}$ produced patterns consistent with clusters [46].

Some preliminary experiments investigating eutectic compositions of binary mixtures using colloidal polystyrene particles have been carried out by Hu *et al.* [48], who phase separated samples by preparing droplets of the suspension and letting the water evaporate, inducing the particles into crystalline or amorphous structures. They studied the structure using optical microscopy and light scattering techniques and found that the kinetics of the system were slowest at mixing ratios corresponding to the best glass forming composition of a CuZr alloy. Furthermore, Kozina and coworkers were able to enhance crystallisation in eutectic binary mixtures of polystyrene microgel spheres by adding an attraction into the system, although it is not clear whether the effects were due to each species' polydispersity (6 and 8%) or the mixing composition of the particles, or indeed the fact they were comparing their attractive hard-sphere suspension with a model hard-sphere system [56].

When investigating the effects of particle size on colloidal phase behaviour, the use of a bidisperse colloidal system, rather than a continuous distribution of particles, is advantageous; the distribution and overall polydispersity is easier to tune in a binary system (using different batches of particles) than attempting to synthesise one batch of particles with a particular polydispersity. However the ability for binary systems to crystallise into complex lattices is at odds with the polydisperse systems, which can have similar close packing features and the same numerical polydispersity value as a binary system. There are obviously some features in common, particularly the unexpected amorphous regions of binary phase diagrams, which resonate with the high-concentration, polydisperse hard-sphere systems that do not manage to reach their equilibrium multiple solid states. It is clear great care must be taken in characterising a system of particles and some thought must be made about the choice of a binary or a polydisperse system depending on the avenue of interest.

3.5 Types of distribution

Pusey, while not the first to use the concept, was one of the first to propose that the dimensionless polydispersity was used to characterise size-disperse systems [86], rather than stating the parameters of the particular distribution. This makes sense from a practical viewpoint; it is much easier to make comparisons between different systems with a dimensionless measure of polydispersity, and in a lot of cases the particular distribution chosen does not have a significant effect on the results [23]. But, as evidenced by the example of the Brambilla/Zaccarelli debate discussed in section 3.2, eventually the details do become important. Here I will briefly present some distributions commonly used to model size distributions of colloidal particles.

3.5.1 Symmetric distributions

Name	PDF, $F(R)$	Mean Radius, $\overline{R}$	Polydispersity
Uniform	$\frac{1}{b-a}, a \leq R \leq b$	$(a+b)/2$	$(b-a)/\sqrt{3}(a+b)$
Triangular	$\frac{2(R-a)}{(b-a)(c-a)}, a \leq R \leq c$ $\frac{2(b-R)}{(b-a)(b-c)}, c < R \leq b$	$(a+b)/2$	$(b-a)/\sqrt{6}(a+b)$
Gaussian	$\frac{1}{\sqrt{2\pi}\sigma} e^{-(R-\mu)^2/2\sigma^2}$	μ	σ/μ

Table 3.1 Typical forms of probability distribution functions (PDF) used in theory and simulations

The distributions in table 3.1 are often used in simulations and theory due to their simple analytic forms. Many of the examples referenced throughout this chapter made use of these, the most common being the top-hat or uniform distribution. The uniform distribution is the most simple and it has the advantage that the range $[a, b]$ can be exactly defined and as such ensure that no particles have zero (or negative) radius. However, the uniform distribution is the least realistic approximation to an experimental system - particle synthesis usually produces particles with a peaked distribution.

The triangular distribution is the most simple distribution which has a peak, at $R = c$. Again it has a well-defined interval, $[a, b]$ and asymmetry is possible if

$(c-a) \neq (b-c)$. It does not however have any tails, so if the small percentage of very large or very small particles in an experimental system are having an effect, using this distribution will not account for that possibility. The third distribution in table 3.1 is the well-known Gaussian, or Normal distribution. The central limit theorem tells us that distributions of random variables can be approximated as a Gaussian distribution, therefore it has wide-ranging applicability. A Gaussian distribution also has interesting mathematical properties (*e.g.* the sum of two normalised Gaussian distributions is also a Gaussian distribution), so it is not surprising that it is often used to approximate an experimental particle distribution. However, distributions of particle sizes are rarely symmetric and a Gaussian distribution also allows $R \leq 0$, which is not physically possible.

So, in order to attain a realistic model for experimental particles, we must consider more complex disributions.

3.5.2 Asymmetric distributions

As mentioned above, measured particle distributions are rarely symmetric [40, 92], so a realistic model should allow for the skewness of the particle size distribution. The Schulz distribution, sometimes referred to as the Gamma distribution, is often used as it has a relatively straightforward analytical form and is physically realistic, having no radii less than zero. It is used in scattering models of particles [6], where it is a standard distribution used to characterise particles. The Schulz distribution has also been used to model a bidipserse distribution of charged macroions [72], as well as a model for bacteria velocities [65].

Martin and coworkers fitted distributions to Bragg scattering data of particles and proposed a Weibull distribution was the best fit to their system [64], while others have utilised a log-normal distribution [42]. These are more realistic distributions, but are more complex, restricting their applicability in theoretical models. Recent research regarding random close packing of polydisperse spheres suggest that, at least for the determination of ϕ_{rcp}, the skewness is equally as important as the magnitude of the polydispersity [23], suggesting it is something we keep track of when investigating other aspects of polydisperse systems[2].

[2]Analytical expressions for skewness of each distribution (which is not an independent parameter) can be readily obtained but were too unweildly to be easily included in table 3.2.

Name	PDF, $F(R)$	Mean Radius, $\bar{R}$	Polydispersity
Schulz	$\frac{\theta^{-\alpha}R^{\alpha-1}e^{-R/\theta}}{\Gamma(\alpha)}, R>0$	$\alpha\theta$	$\sqrt{\frac{1}{\alpha}}$
Weibull	$\alpha\theta^{-\alpha}R^{\alpha-1}e^{-(\frac{R}{\theta})^{\alpha}}, R>0$	$\theta\Gamma(1+1/\alpha)$	$\sqrt{\frac{\Gamma(1+2/\alpha)}{\Gamma(1+1/\alpha)}-1}$
Log-normal	$\frac{1}{\sqrt{2\pi}\sigma R}e^{-(log(R)-\mu)^2/2\sigma^2}, R>0$	$e^{\mu+\sigma^2/2}$	$\sqrt{e^{\sigma^2}-1}$

Table 3.2 Probability distribution functions (PDFs) for more experimentally realistic, asymmetric size distributions of particles. The Schulz (Gamma) distribution and Weibull distributions are valid on the interval $[0,\infty)$, have shape parameter, α, scale parameter θ and $\Gamma(\alpha)$ is the Gamma function. The parameters σ and μ in the log-normal distribution are the standard devation and mean of $ln(R)$, respectively and is defined on the interval $(0,\infty)$.

3.6 Why study Polydispersity?

In many cases, a slight degree of polydispersity does not introduce quantitatively new effects - experiments using particles with polydispersities $\lesssim 5\%$ [88] agree with the predicted equilibrium phase behaviour from computer simulations of monodisperse hard spheres [47]. We also know that in this low polydispersity limit, no new phenomena are introduced in experimental attractive phase diagrams [83].

Anecdotal evidence suggests that many researchers observe strange behaviour when using polydisperse particles but either do not mention it or do not consider polydispersity as a cause for the strangeness [77]. There have been few comprehensive experimental studies undertaken to investigate the effects of polydispersity on phase behaviour of colloidal suspensions, the last by Fairhurst in 1999 [31]. Experiments tend to be focussed on low polydispersity effects [103], or the testing of a particular feature [32]. In the meantime, theoretical predictions have progressed [107], enabling a basis for comparison of any new experimental results.

In summary, while some of the effects of polydispersity on colloidal systems discussed in this chapter have received ongoing interest, a lack of systematic, experimental studies hinders further progress and understanding. In this thesis, I present the effects of size polydispersity on experimental hard spheres and a short-range attractive hard-sphere system. I have restricted my observations and

analysis to hard-sphere and short-range attractive systems. The hard-sphere effects, namely fractionation and dynamics, are presented in chapter 5 before considering the effects of polydispersity on attractive phase behaviour in chapter 6. Understanding the observed behaviour relied heavily on detailed characterisation of the size distributions of particles from analysis of transmission electron microscope images. This is discussed in the following methods chapter, along with some information on light scattering techniques, used for characterisation and dynamics studies.

Chapter 4

Methods

This chapter describes the methods used throughout this thesis. The experimental techniques - preparing the particles, measuring volume fractions and visual observations - were common to all experiments and will be described here. The methods used to characterise the size and polydispersity of the particles will also be presented in this chapter: small-angle x-ray scattering and transmission electron microscopy, as well as the image analysis protocol used to extract the size distribution of the particles. Finally, light scattering theory, applicable to both the x-ray scattering techniques and the dynamic light scattering measurements used in chapter 5, will be outlined.

4.1 Everyday experimental procedures

All of the particles used in this thesis consist of a cross-linked core of polymethylmethacrylate (PMMA) latex, synthesised in-house by Andrew Schofield and were received suspended in dodecane. Dodecane has a refractive index lower than that of PMMA ($n = 1.421$ and 1.49 respectively); mismatch of refractive index engenders multiple scattering in the suspension, making visual observations difficult. It is better to use a solvent with a more closely matched refractive index; traditionally cis-decahydronapthalene (cis-decalin) is used.

Solvents and particle washing

Pure cis-decalin is expensive, so instead we generally use a mixture of cis- and trans- isomers. Henceforth the mix-decalin shall just be referred to as decalin. The proportion of cis- to trans- varies batch to batch, but since it is purchased in large quantities, the decalin used will belong to the same batch and properties will be consistent across the experiments. The decalin used in this thesis had density of $\rho = 0.88123(1)\text{g/cm}^3$ (DMA 4500, Anton Paar) and refractive index $n = 1.4732(2)$ (Bellingham and Stanley LTD).

To replace the dodecane with decalin, the particles are spun down until they form a densely packed sediment, with an interface that remains stationary with respect to the vial as the vial is tipped, allowing the dodecane to be replaced by decalin. Some dodecane will still be trapped in the particle sediment, so the particles should be redispersed and the process repeated until the desired solvent purity is achieved.

The number of spin-replace steps (a wash) can be calculated using the fractional height, f, of the sediment and ϕ_{rcp}, the volume fraction of the random-close-packed sediment. Vials were spun at a speed of 2500rpm until all particles were part of the sediment, approximately 15 hours. The fraction of dodecane trapped within the sediment after one spin is $(1 - \phi_{rcp})f$. The particles themselves take up a proportion of $\phi_{rcp}f$ of the total volume, so the proportion, x, of dodecane remaining after one wash is

$$x = \frac{(1 - \phi_{rcp})f}{1 - \phi_{rcp}f} \tag{4.1}$$

After n washes the proportion of dodecane remaining in the solvent is x^n, allowing us to easily calculate the number of washes required to attain any desired purity. Sigma-Aldrich uses a benchmark purity of $\geq$ 98.5% for 'high purity' solvents (ReagentPlus® Grade), while Fisher Scientific's 'ultra pure' (OPTIMA® Grade) acids have "as low as $1-100$ ppt detection" for various impurities, corresponding to a purity of 99.9%. Using $\phi_{rcp} = 0.64$, the calculated purity of the new solvent after n washes, for various sediment height fractions, f, are shown in table 4.1. From table 4.1 we can see that the purity is sensitive to f: 4 washes gives 99.9% purity when $f = 0.4$, but 7 washes are required to attain the same purity when f is increased to 0.6. The unwashed particles typically had $f \approx 0.5$, and 7 washing steps were usually executed.

Table 4.1 Replacing a solvent in a particle suspension requires a number of washes, n, as described in the text. The purity of the new solvent is dependent on the fractional height of the close-packed particle sediment, f.

n		0	1	2	3	4	5	6	7
Purity(%)	f=0.4	0.0	80.6	96.3	99.3	99.9	100.0	100.0	100.0
	f=0.5	0.0	73.5	93.0	98.1	99.5	99.9	100.0	100.0
	f=0.6	0.0	64.9	87.7	95.7	98.5	99.5	99.8	99.9

Other solvents may be used to tailor the properties of the suspension. For example, an index-matching mixture, useful for scattering experiments, can be made from a mixture of decalin and tetrahydronaphthalene (tetralin) [99]. PMMA swells in tetralin, so the suspension must be prepared many weeks in advance of the experiments taking place, to prevent any change in size of the particles during the experiments. Density matching is also useful to prevent the particles from sedimenting. Sedimentation can disrupt equilibrium processes; colloidal systems prepared in density-matched solvents or experiments performed in microgravity display different crystallisation behaviour to those subject to gravity [126]. One example of a solvent combination used to density match particles is decalin and cyclohexyl bromide, with tetrabutyl-ammonium chloride salt added to screen the charges present in the solvent combination. The particle washing technique described above can also be used to suspend particles in density matched solvents: density matching is generally only exact at one temperature and the temperature inside the centrifuge will tend to increase with time, either by energy inefficiency or by some inbuilt temperature control.

Hard-sphere behaviour with minimal particle sedimentation was desired for the experiments in this thesis. To this end, small particles suspended in decalin were used. The sedimentation velocity, v_s of a particle of radius R and density ρ_P in a solvent with density ρ_S and viscosity η ($\eta_{decalin} = 0.00131$Pas) is given by the balance of weight, buoyancy and Stokes drag forces acting on the particle:

$$\frac{4\pi}{3}R^3(\rho_P - \rho_S)g = 6\pi\eta R v_s \tag{4.2}$$

$$v_s = \frac{2}{9}\frac{R^2\Delta\rho g}{\eta} \tag{4.3}$$

where $\Delta\rho = (\rho_P - \rho_S)$. Using typical values of densities of PMMA and decalin ($\rho_P = 1.18$ gcm^{-3} and $\rho_S = 0.894$ gcm^{-3}), the time taken for a single particle

of radius 100 nm to sediment 15 mm is 81 days. Larger particles sediment faster; increasing the particle radius to 200 nm decreases the sedimentation time by a factor of 4. Furthermore, sedimentation time for a higher volume fraction of particles will be slower due to particle-particle interactions. A quantitative record of sedimentation was not made during the experiments, but no visible sedimentation around the meniscus of ASM320 or ASM295 particles ($R \approx 150$ nm) was observed on the scale of at least one month, as expected by the calculations above. The use of small particles in these experiments ensures gravity and charge were not dominant parameters, but the particles were too small to measure using conventional microscopy and not index matched, complicating characterisation and ruling out the possibility for direct visualisation of the particles' *in situ* behaviour.

Measuring volume fractions

The problems associated with measuring volume fractions were discussed earlier in this thesis; in this section, details of the particular techniques employed during these experiments will be described. A rough estimate of the volume fraction was initially obtained by spinning down the particles in the centrifuge at a speed of 2500rpm. Centrifugation packs the particles in a random configuration (on a timescale shorter than that needed for crystallisation to take place) hence the volume fraction of the random close packed sediment can be calculated using $\phi = \phi_{rcp} f$, where f is the fractional height of the random-close-packed sediment and ϕ_{rcp} is its volume fraction. The variability of ϕ_{rcp} with polydispersity was discussed in detail in chapter 3.1.4: a polydisperse distribution of particles will have close-packed volume fraction greater than 0.64. However, since this method was only used as an initial estimation of the volume fraction and the value of ϕ_{rcp} only varies by a few percent for small changes in polydispersity, greater accuracy at this stage was not essential.

After the initial estimate was calculated, a more precise estimate was made by preparing samples around the fluid-solid coexistence region of the hard sphere phase diagram. The particles were allowed to equilibrate for approximately two weeks and the percentage height of crystals to fluid was determined in each case by measuring the height with an upright vernier rule. The vial with the highest proportion of crystal phase was assigned the volume fraction ϕ_m, and all others were rescaled relative to this value. ϕ_m was set to be equal to greatest volume

fraction for a single polydisperse solid (see figure 3.1), $\phi_m = 0.58$. This of course will lead to systematic errors in the absolute volume fraction, but the relative volume fractions for samples in each batch will be accurate. Volume fractions were adjusted by adding solvent dropwise, or centrifuging the vials and removing a number of drops of solvent. Using the change in mass of the vial and the measured density of decalin, it is straightforward to calculate the new volume fraction from the lever rule, $\phi_1 V_1 = \phi_2 V_2$ (chapter 2.3.2).

The particles can be treated with a fluorescent dye to enable various types of microscopy [12]; the batch ASM295 used in the experiments in chapter 5 were dyed with Nile Red (Supplied by SigmaAldrich, $\lambda_{ex} = 548$ nm, $\lambda_{em} = 567$ nm), although fluorescent properties were not required.

Adding attraction

In the projects forming this thesis, attraction between the particles was induced by adding a polystyrene depletant. The range of the attraction depends on the radius of gyration, r_g, of the polystyrene, which in turn depends on the temperature of the solvent. The ideal temperature for a polymer in a solvent, that is, the temperature at which the polymer acts like an ideal random walk, is known as the theta temperature, T_θ. Berry measured the theta temperature of polystyrene in different mixtures of cis- and trans- decalin [10]. The decalin used in these experiments had density $\rho = 0.88123$ g/cm^3, while the literature values for the density of cis- and trans-decalin are $\rho_{cis} = 0.897$ g/cm^3 and $\rho_{trans} = 0.87$ g/cm^3 respectively. By assuming a linear relationship between density of the mixture and percentage of cis-decalin, the solvent used in these experiments contains $\approx 42\%$ cis-decalin. A similar calculation was performed using the refractive index of each solvent, resulting in a cis-decalin percentage of 35%. Thus, using figure 4 of Berry's paper, T_θ of polystyrene in decalin is between $289 - 291$ K [10].

At the theta temperature, the radius of gyration of the polystyrene, its effective spherical radius, scales as the square root of the molecular weight: $r_g^\theta = 0.028\sqrt{M_W}$ nm, where the molecular weight is measured in daltons.

Berry also gave an expression for the coil swelling at a temperature away from

T_θ, which depends on the so-called Fixmann parameter z:

$$z = 0.00975\sqrt{M_W}\left[1 - \frac{T_\theta}{T}\right]. \tag{4.4}$$

For values of z below 0.1, the radius of gyration can be well approximated by

$$r_g = r_g^\theta\sqrt{1 + \frac{134}{105}z}. \tag{4.5}$$

Using equation 4.5 and a theta temperature of 290 K we find that the polystyrene used in these experiments, which had molecular weight of 114, 200 Daltons (and unknown polydispersity), has a radius of gyration (at 298 K) of $r_g = 10$ nm.

ASM320 particles used in the attractive hard-sphere experiments of chapter 6 had average radius $R = 152(2)$ nm, as determined by small-angle x-ray scattering and dimensionless attraction range $\xi = r_g/R = 10/152 = 0.07(1)$.

The *strength* of the attraction is controlled by the concentration of polymer present in the system. In practice this is simple to measure and implement: vials of particles were prepared at the required volume fraction, then solid polystyrene was added directly to the vials using a thin metal spatula. Vials were mixed on a rollerbank overnight to disperse the polystyrene and were checked by eye to ensure there were no large lumps of polystyrene remaining, before continuing with observations. Vials were left undisturbed in an incubator set at 298K for up to two weeks, then solvent was added dropwise to the vial to dilute the sample. This results in the data points becoming arranged on dilution lines in the (ϕ, c_p) plane that can be extrapolated to the origin at infinite dilution.

Characterising phases

The initial characterisation of the phases was determined by eye, using a small hand-held torch to distinguish interfaces and crystallites. The expected phases are easy to distinguish from one another; the fluid phases are spatially homogeneous and either optically opaque (liquid) or transluscent (gas), while the solid phase is seen as irridescent crystallites when the torch is directed towards them. A sample that has undergone complete gas-liquid separation appeared as two fluid phases with a sharp, horizontal interface between them. Some phase separating samples were recorded so that the height of the phase boundary could be recorded as a function of time. Particles in a gel phase underwent a characteristic gel collapse,

described in section 2.3.3, and had a particle-solvent interface that remained parallel to the vial bottom when the vial was tipped. Colloidal glasses were classified similarly by a stationary suspension-air interface when the vial was tipped and a 'shimmery' appearance.

New phases within the hard-sphere and attractive hard-sphere phase diagrams, that are not present in an equivalent monodisperse system, were discovered during the course of the experiments. These will be discussed in detail in the results chapters. For these new phases, additional characterisation was performed as an attempt to elucidate the observed behaviour, using 3-dimensional dynamic light scattering, small-angle x-ray scattering and transmission electron microscopy, described in the following sections.

4.2 Characterisation of size

The size of colloidal particles can be measured either directly, through microscopy techniques, or by using indirect methods, such as light scattering. Optical microscopy allows the radii of large particles to be measured readily, but the range of colloidal length scales extends below the limit of resolution of optical microscopes. Light, x-ray, or neutron scattering can probe length scales shorter than that of optical microscopy, but the inversion process required to extract radii from the measured data can be complicated. Either the average radius and polydispersity of the particles can be determined, or some information about the distribution shape is incorporated into a particle scattering model to fit more detailed characteristics.

The problem of carefully characterising small, polydisperse particles was solved by using a combination of transmission electron microscopy and small-angle x-ray scattering, to obtain a direct measurement of the distribution and the average *in situ* behaviour, respectively. The basics of light scattering theory is described below, followed by a description of the electron microscopy and analysis methods.

4.2.1 Scattering theory

In an ideal scattering experiment, radiation in the form of neutrons, x-rays or light are incident upon a sample. The incident radiation is either singly

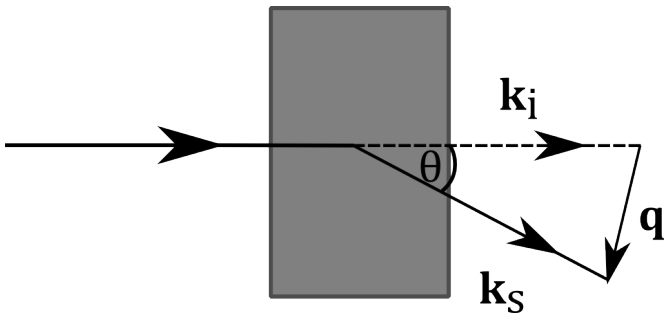

Figure 4.1 Single scattering of light incident on a scattering volume. Some radiation with wavevector $\mathbf{k}_i$ is transmitted through the sample; the scattered radiation, wavevector $\mathbf{k}_s$, is deflected by an angle θ by a scatterer within the volume. The scattering vector $\mathbf{q}$ is defined as the difference between the two wavevectors.

scattered to some point, $\mathbf{R}$, in the far field, or transmitted straight through the scattering medium, as illustrated in figure 4.1. This single scattering scenario is valid when the suspension is dilute - the scattered radiation is unlikely to be rescattered by other particles before exiting the sample. In concentrated suspensions, multiple scattering will be present. Experimental setups designed to minimise the detection of multiple-scattered radiation in dynamics studies are discussed in section 4.3.

The incident and scattered wavevectors, $\mathbf{k}_i$ and $\mathbf{k}_s$, have equal magnitude:

$$k = \frac{2\pi n_p}{\lambda_0}, \tag{4.6}$$

where λ_0 is the wavelength of the laser and n_p is the refractive index of the scattering material.

The scattering vector $\mathbf{q}$ is the independent variable in scattering experiments; it has dimensions of $[\mathrm{m}^{-1}]$ and is defined as the difference between incident and scattered wave vectors. From the geometry of the $\mathbf{q}$ vector in figure 4.1 above, the magnitude of the scattering vector can be derived as

$$q = \frac{4\pi n_p}{\lambda_0} \sin\frac{\theta}{2}. \tag{4.7}$$

The physics of scattering is equivalent for each type of radiation, with the difference that the refractive indices in light scattering are replaced by electron densities in x-ray scattering and scattering length densities in neutron scattering.

There are several important assumptions present in scattering theory. Firstly, we

assume that the degree of scattering by the suspending solvent is much smaller than that of the colloidal particles. The particles themselves also need to be weakly scattering, such that multiple scattering does not become an issue. Finally, in the case of spherical particles, we assume the refractive index only varies with radius within the particle rather than the particle orientation.

We are interested in the amplitude $b_i(q)$ of the field of light scattered by particle i. This is derived starting with the amplitude of the electrical field of radiation, scattered by a spherical point particle to a detector at position $\mathbf{R}$. The incident electric field is a plane wave of form

$$\mathbf{E}_i(R,t) = \mathbf{n}_i E_o \exp\left[i(\mathbf{k}.\mathbf{R} - \omega_i t)\right], \tag{4.8}$$

where $\mathbf{n}_i$ is the unit vector in the direction of the incident field, E_0 is the field amplitude and ω_i is the angular frequency. This plane wave is incident on a medium with local dielectric constant $\varepsilon(\mathbf{r},t)$ at position $\mathbf{r}$ within the scattering volume[1].

The component of the scattered electric field is then given by [9, 87]:

$$\mathbf{E}_S(\mathbf{R},t) = \frac{-k^2 E_0}{4\pi}\frac{\exp\left[i(kR-\omega t)\right]}{R}\int_V \left[\frac{\varepsilon(\mathbf{r},t)-\varepsilon_0}{\varepsilon_0}\right]\exp\left(-i\mathbf{q}.\mathbf{r}\right)\mathrm{d}^3 r, \tag{4.9}$$

where ε_0 is the average dielectric constant of the medium.

For discrete particles, there is scattering from both the particles and the liquid, which have dielectric constants $\varepsilon_P(\mathbf{r},t)$ and $\varepsilon_L(\mathbf{r},t)$ respectively. It is more useful to be able to write the bracketed term in equation 4.9 as a function of the measurable dielectric constants of the particle, $\varepsilon_P(\mathbf{r},t)$, and averaged solvent, ε_L:

$$\begin{aligned}
\varepsilon(\mathbf{r},t) - \varepsilon_0 &= [\varepsilon_P(\mathbf{r},t) - \varepsilon_0] + [\varepsilon_L(\mathbf{r},t) - \varepsilon_0] \\
\varepsilon(\mathbf{r},t) - \varepsilon_0 &= [\varepsilon_P(\mathbf{r},t) - \varepsilon_L + \varepsilon_L - \varepsilon_0] + [\varepsilon_L(\mathbf{r},t) - \varepsilon_L + \varepsilon_L - \varepsilon_0] \\
\varepsilon(\mathbf{r},t) - \varepsilon_0 &= [\varepsilon_P(\mathbf{r},t) - \varepsilon_L] + [\varepsilon_L(\mathbf{r},t) - \varepsilon_L] + 2(\varepsilon_L - \varepsilon_0)
\end{aligned} \tag{4.10}$$

[1]The scattering volume is within the scattering medium, and is the region of intersection of the incident and scattered radiation beams

This leads to three contributions in equation 4.9: the first term in equation 4.10 is the scattering from inside the particles due to the difference in refractive index between themselves and the surrounding fluid. The second term in equation 4.10 is scattering due to density fluctuations in the suspending solvent. This term can be neglected, since the background scattering from the solvent is measured separately and subtracted from the suspension scattering data, which is assumed to be negligible. The last term is independent of r, so results in a term in equation 4.9 proportional to $\int_V \exp\left[-i\mathbf{q}.\mathbf{r}\right] = \delta(\mathbf{q})$, where $\delta(\mathbf{q})$ describes the straight through unscattered beam at $q = 0$. In practice, this term has finite width due to finite sample volume: it decays exponentially away from $\mathbf{q} = 0$ and can therefore be neglected when $\mathbf{q} \neq 0$. Equation 4.9 can now be written as

$$\mathbf{E}_S(\mathbf{R},t) = \frac{-k^2 E_0}{4\pi}\frac{\exp\left[i(kR-\omega t)\right]}{R}\times \tag{4.11}$$

$$\sum_j \left(\int_{Vj} [\frac{\varepsilon_P(\mathbf{r}_j,t)-\varepsilon_L}{\varepsilon_0}] \exp -i\mathbf{q}.\mathbf{r_j}\, \mathrm{d}^3 r_j\right) \exp\left[-i\mathbf{q}.\mathbf{R}_j(t)\right], \tag{4.12}$$

where $\mathbf{R}_j(t)$ is the position of the centre of mass of particle j at time t; $\mathbf{r}_j$ is the position of the volume element, $\mathrm{d}^3 r_j$, relative to its centre of mass, and $\varepsilon(\mathbf{r}_j,t)$ is the local dielectric constant at position r_j in particle j.

From here, the prefactor describing the spherical wave of scattered radiation emitted from the origin is usually omitted, and we introduce $\Delta\rho(\mathbf{r}_j,t)$, the local density of the scattering material:

$$\Delta\rho(\mathbf{r}_j,t) = \frac{k^2}{4\pi}\left[\frac{\varepsilon_P(\mathbf{r}_j,t)-\varepsilon_L}{\varepsilon_0}\right]. \tag{4.13}$$

Equation 4.11 now becomes

$$E_S(\mathbf{R},t) = \sum_{j=1}^{N} b_j(\mathbf{q},t)\exp\left[-i\mathbf{q}.\mathbf{R}_j(t)\right], \tag{4.14}$$

where $b_j(\mathbf{q},t)$ is the scattering length (amplitude of the field of light) of particle j,

$$b_j(\mathbf{q},t) = \int_{V_j} \Delta\rho(\mathbf{r}_j,t)\exp\left(-i\mathbf{q}.\mathbf{r}_j\right)\mathrm{d}^3 r_j. \tag{4.15}$$

The quantity measured directly in experiments is the scattered intensity, $I(\mathbf{q},t)$,

which is related to the electric field by

$$I(\mathbf{q},t) = |E(\mathbf{q},t)|^2 \tag{4.16}$$

and has time averaged value of

$$\langle I(\mathbf{q})\rangle = \sum_i \sum_j \langle b_i(\mathbf{q}) b_j^*(\mathbf{q}) \exp\left[i\mathbf{q}.(\mathbf{r}_i - \mathbf{r}_j)\right]\rangle. \tag{4.17}$$

Equation 4.17 now gives an expression for the scattered intensity which can be expressed in terms of known (or measurable) quantities, such as the single particle form factor, $P(q)$ and the static structure factor, $S(q)$, as follows.

For dilute systems, particle j can take any position in the sample; they are randomly distributed about zero, so all contributions to equation 4.17 are zero except when $i = j$. Hence for dilute particles,

$$\langle I(\mathbf{q})\rangle = \sum_i \langle |b_i(\mathbf{q})|^2\rangle. \tag{4.18}$$

For identical particles, $b_i(\mathbf{q}) = b(\mathbf{q})$, so

$$\begin{aligned} \langle I(\mathbf{q})\rangle &= N\langle |b(\mathbf{q})|^2\rangle \\ &= NP(q)|b(0)|^2, \end{aligned} \tag{4.19}$$

where the single particle form factor, $P(q)$, is defined such that $P(q) \to 1$ as $q \to 0$:

$$P(q) = \frac{\langle |b(\mathbf{q})|^2\rangle}{\langle |b(0)|^2\rangle}. \tag{4.20}$$

For concentrated samples of identical particles, the $b(\mathbf{q})$ terms in 4.17 are still identical and can be brought in front of the summation:

$$\langle I(\mathbf{q})\rangle = \langle |b(q)|^2\rangle \sum_i \sum_j \langle \exp\left(i\mathbf{q}.(\mathbf{r}_i - \mathbf{r}_j)\right)\rangle \tag{4.21}$$

and the static structure factor, $S(q)$ is defined such that equation 4.21 can be

expressed as

$$\langle I(\mathbf{q})\rangle = \langle |b(0)|^2\rangle P(q) NS(q). \tag{4.22}$$

This last equation tells us that the scattered intensity measured in an experiment is directly related to the single particle form factor. Therefore, if a theoretical form of $P(q)$ is known, it can be calculated and fitted to the experimental data to then, for example, characterise the scatterers.

Single particle form factor

There are various forms for $P(q)$ depending on the characteristics of the particles in question. Many useful theoretical form factors are given by Pederson in [74]. The simplest is the form factor for a single homogeneous sphere, first calculated by Lord Raleigh in the early 20^{th} Century [90]. Returning to the definition of the scattering length of particle j in equation 4.15, assuming the distribution of scattering material is homogeneous inside the sphere, then the $\Delta\rho$ term can be taken outside the volume integral:

$$\begin{aligned} b(q) &= \Delta\rho \int_{sphere} \exp\left(-i\mathbf{q}.\mathbf{r}\right) \mathrm{d}^3 r \\ &= \Delta\rho \int_0^{2\pi} \mathrm{d}\phi \int_0^{\pi} \sin\theta \,\mathrm{d}\theta \int_0^{R} r^2 \exp\left(-iqr\cos\theta\right) \mathrm{d}r \\ &= \Delta\rho 2\pi \int_0^{R} r^2 \,\mathrm{d}r \int_0^{\pi} \sin\theta \exp\left(-iqr\cos\theta\right) \mathrm{d}\theta \end{aligned} \tag{4.23}$$

change of variables; $f = \cos\theta$

$$\begin{aligned} b(q) &= \Delta\rho 2\pi \int_0^{R} r^2 \,\mathrm{d}r \int_{-1}^{1} -\exp\left(-iqrf\right) \mathrm{d}f \\ &= \Delta\rho 2\pi \int_0^{R} r^2 \,\mathrm{d}r \frac{2\sin qr}{qr} \\ &= \Delta\rho \frac{4\pi}{q} \int_0^{R} r \sin qr \,\mathrm{d}r \\ b(q) &= \Delta\rho \frac{4\pi R^3}{3(qR)^3} 3(\sin qR - qR\cos qR). \end{aligned} \tag{4.24}$$

Then, using equation 4.20 and the fact that $9(qR)^{-6}(\sin qR - qR\cos qR)^2 \to 1$ as $q \to 0$, the single particle form factor is

$$P(q) = \frac{9}{(qR)^6}(\sin qR - qR\cos qR)^2. \tag{4.25}$$

Similarly, the form factor for a core-shell particle with core radius R_c and (shell+core) radius of R_s is

$$P_{cs}(q) = \frac{9}{q^6}\left[\frac{\sin qR_c - qR_c\cos qR_c + A(\sin qR_s - qR_s\cos qR_s)}{R_c^3 + AR_s^3}\right]^2, \tag{4.26}$$

where $A = (n_s - n_c)/n_c$. n_s and n_c are the refractive indices of the shell and core (relative to the solvent), respectively.

These expressions were all determined with the assumption that the scatterers are identical. The particles used in this thesis are polydisperse in size, so it is pertinent to also consider the form of $P(q)$ when the scatterers are not identical.

Polydisperse form factor

When the particles are not identical in size, equation 4.20 becomes

$$P_{poly}(q) = \frac{\sum_i^N \langle|b_i(\mathbf{q})|^2\rangle}{\sum_i^N \langle|b_i(0)|^2\rangle}, \tag{4.27}$$

$$P_{poly}(q) \to \frac{\sum_i^N \langle|b_i(0)|^2\rangle P(q,R_i)}{\sum_i^N \langle|b_i(0)|^2\rangle} \tag{4.28}$$

$$= \frac{1}{\sum_i^N \langle R_i^6\rangle}\sum_i^N \langle|b_i(0)|^2\rangle P(q,R_i). \tag{4.29}$$

For a continuous size distribution, $f_{psd}(R)$, with $f_{psd}(R)dR$ particles between R and $R + dR$, equation 4.29 can be expressed as

$$P_{poly}(q) = \frac{1}{\overline{R^6}}\int f_{psd}(R)R^6 P(q,R)\,\mathrm{d}R. \tag{4.30}$$

Equation 4.30 allows the theoretical form factor for any continuous distribution to be readily calculated. It can be simplified to a discrete form if the continuous

size distribution is too complex to calculate easily, or for calculating form factors from an experimental size distribution. A comparison of monodisperse (points) and polydisperse (line) calculated form factors is shown in figure 4.2. The monodisperse radius is 150 nm, and the polydisperse particles were generated from a normal distribution, centred around $R = 150$ nm. The effect of polydispersity is clear: the minima, which occur when $qR = 4.493$, appear smeared out when the particles have a range of sizes. In fact, it is possible to derive an analytical expression for the polydispersity as a function of the ratio of the relative intensities of the first minimum and second maximum of the form factor [31].

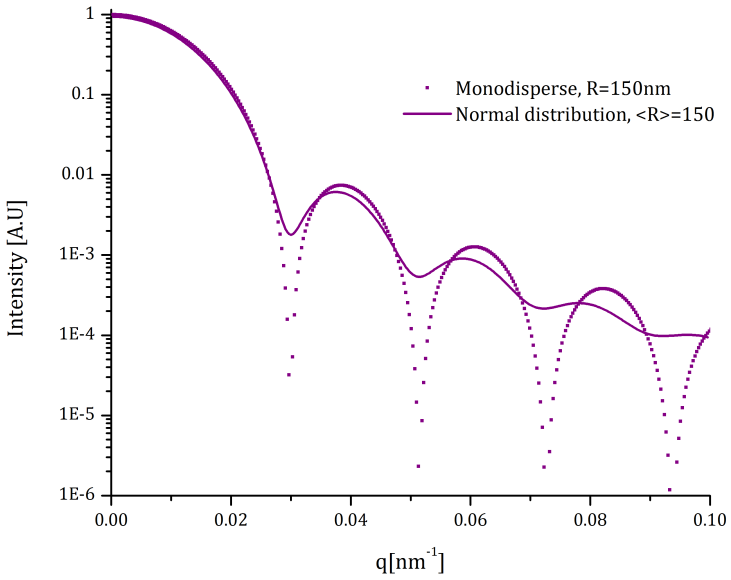

Figure 4.2 Normalised form factor for monodisperse particles with radius 150 nm (points), calculated using equation 4.25, and a normal distribution of particles with average radius 150 nm (line), calculated using equation 4.29.

Light or x-ray scattering?

The number of minima measured in an experiment, and hence the length scale probed by scattering, depends on the range of q values on which the technique operates. The range of the scattering vector can be calculated using equation 4.7. For example, in a static light scattering experiment using a HeNe laser ($\lambda_0 = 632.8$ nm) and PMMA particles as the scattering material ($n_s = 1.49$),

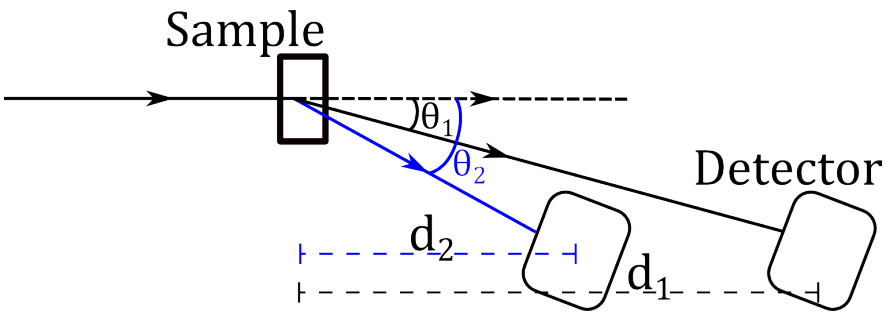

Figure 4.3 Example of using sample-to-detector distance to extend the range of possible q-values in constrained experimental setups: by decreasing the distance of the detector from d_1 to d_2, the scattering angle can be increased from θ_1 to θ_2.

$q = 0.030 \sin(\theta/2)$ nm^{-1}, so the maximum possible value of the scattering vector is 0.030 nm^{-1}, corresponding to a minimum spatial scale $\frac{2\pi}{q} = 209$ nm. For x-rays, which have a much smaller wavelength ($\lambda_0 \approx 0.1$ nm), the minimum spatial scale probed by scattering is 0.03 nm.

The lateral space and equipment geometry constraints present in experimental set ups mean that the entire range of q-values is not always accessible. One method to obtain a larger range of angles is to vary the sample-to-detector distance, illustrated in figure 4.3. By decreasing the horizontal distance of the detector to the sample, a larger scattering angle can be obtained.

In the calculated form factors shown in figure 4.2, the first minimum for particles with radius of 150 nm occurs at ~ 0.03 nm^{-1}, so light scattering would not be an effective method to characterise particles of this size; x-ray scattering or an alternative method would need to be used. The particles used in the experiments of this thesis were of the order of 150 nm in size. Light scattering was attempted but a suitable form factor could not be obtained; ultimately x-ray scattering was used to characterise the particles.

SAXS experiments

A variation of x-ray scattering is small-angle x-ray scattering (SAXS).

To measure the size and polydispersity of the ASM320 particles using the form factor method outlined above, an initial sample of the particles were sent to T. Narayanan at the ID02 beamline at the European Synchrotron Radiation Facility in Grenoble, France. The experimental setup described below was later used

to obtain form factors from scattering experiments of phase-separated samples, which will be presented in chapter 6.

Dilute suspensions of ASM320 PMMA particles were characterised using small-angle X-ray scattering (SAXS). Two sample-to-detector distances of 10 m and 1 m were used to cover a scattering vector range of 0.008 $\text{nm}^{-1} \leq q \leq 3\ \text{nm}^{-1}$. The colloidal suspensions were contained in a flow-through capillary cell of diameter 1.8 mm. Measured two-dimensional scattering patterns were normalized to an absolute intensity scale and then azimuthally averaged to obtain the intensity as a function of q, $I(q)$ [24]. Fig. 4.4 shows the background-subtracted SAXS intensity from a dilute suspension. The data can be adequately described by a polydisperse core-shell model with a Schulz size distribution [24]. The best fit parameter values are: mean core radius and polydispersity 152 ± 2 nm and $6.1 \pm 2\%$ respectively, and the volume fraction of the sample was 0.006.

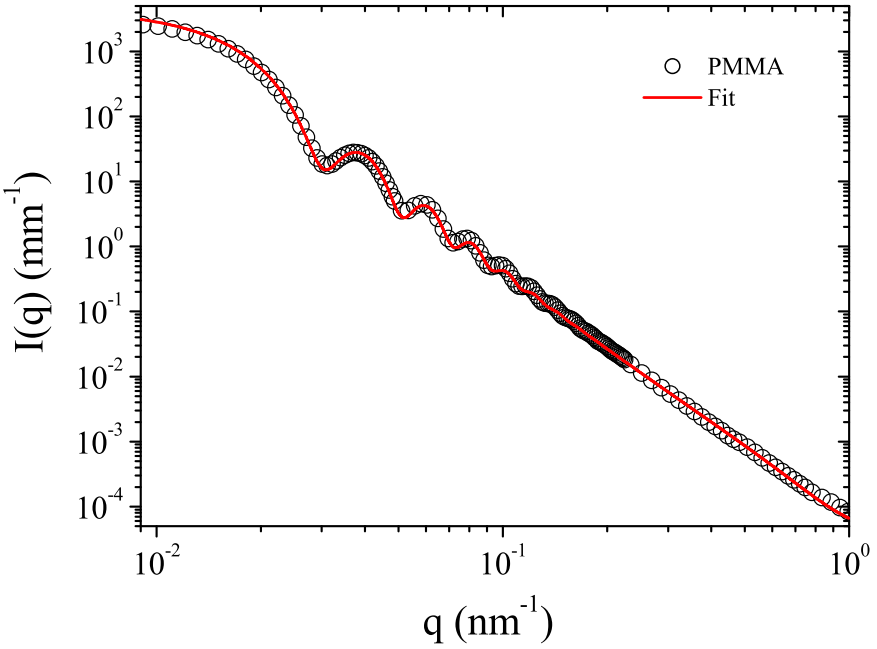

Figure 4.4 Form factor of ASM320 colloidal particles (points) from SAXS measurements by T. Narayanan. The data was fitted with a polydisperse (Schulz distributed) core-shell model, convoluted with an instrument resolution function of width 0.0026 nm^{-1}

.

4.2.2 Transmission electron microscopy

Transmission electron microscopy (TEM) was used to measure size distributions of the polydisperse particles, ASM295 and ASM320, used in this thesis. In TEM,

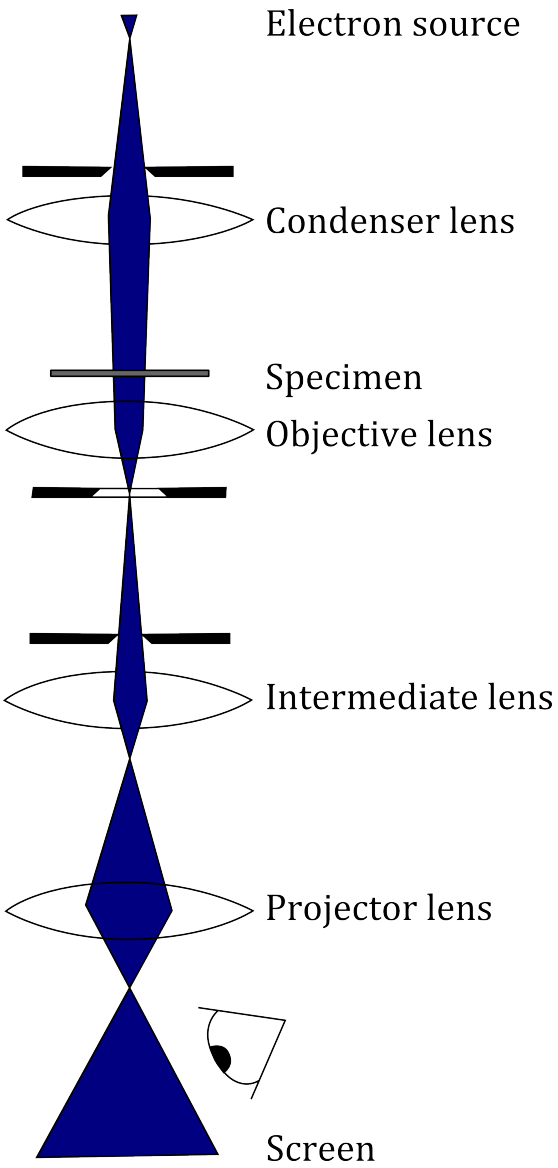

Figure 4.5 Schematic of a TEM imaging system.

a high energy beam of electrons is directed through electromagnetic lenses and a thin sample onto a fluorescent screen or camera, as depicted in figure 4.5. The sample material, which must be dried since the TEM chamber is under vacuum, scatter electrons, where the amount of scattering is dependent on the composition of the material. A typical TEM image of PMMA particles is shown in figure 4.6. Assuming the sample is suitably prepared, TEM can produce high resolution, high magnification images of particles, although there are some problems associated with imaging polymer particles using this technique[2].

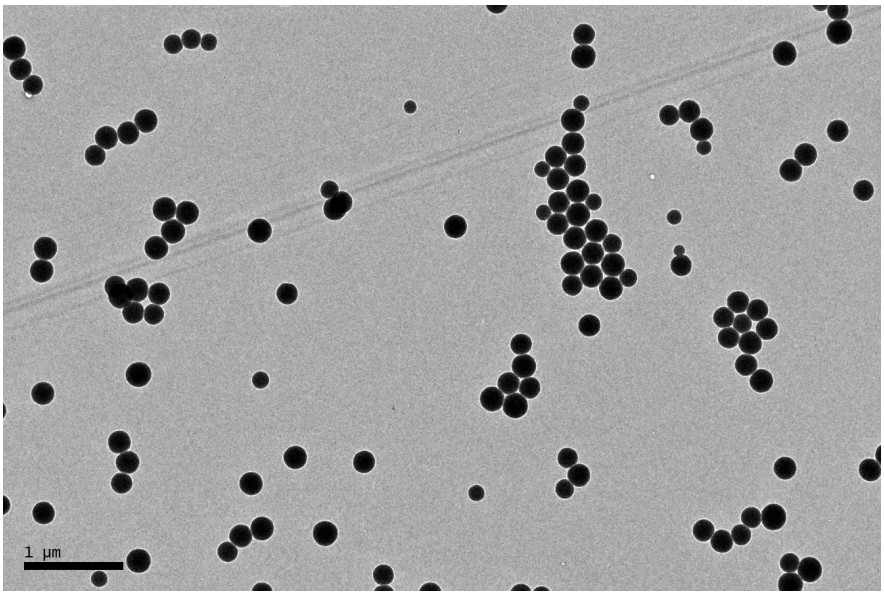

Figure 4.6 Typical TEM snapshot of polydisperse PMMA particles; at least 1000 particles were counted to determine a size distribution. Particles tend to arrange in clusters during the drying process due to the collapse of the stabilising hairs. Clustering can be minimised by decreasing the concentration of particles, but this means many more images need to be acquired to achieve good statistics.

Difficulties imaging PMMA particles with TEM

The difficulties that arise when imaging polymer particles using transmission electron microscopy are summarised below.

- Particle shrinkage
  The TEM operates under vacuum, so the particles must be dried. Unfortunately they will shrink as the solvent evaporates, leading to a decrease in the

[2]It appears these problems are not easily solved, TEM images of melted polymer particles can be found in published work [111].

TEM radius compared to the *in situ* value. There are coating methods to treat the samples before imaging but they were not used: the coating layer will have finite thickness (with associated uncertainty) and, since decalin is volatile, some de-swelling of the particles before the coating is applied will still be present.

- Irradiation damage
  All organic matter interacts with electrons, but the sensitivity of polymers to irradiation damage is lower when the carbon content is increased [69]. For this reason, colloidal polystyrene is less susceptible to the melting behaviour seen in colloidal PMMA samples. Figure 4.7a) is a snapshot of ASM522 particles at 2850× magnification; figure 4.7b) is the same image after a few seconds of exposure to the electron beam. Reference [69] suggests techniques for minimising damage to the polymers, two of which were utilised to achieve better quality images: increase the accelerating voltage of the electrons (100 kV was used, rather than the standard 80 kV of the instrument) and use the "low dose" technique of quickly scanning and acquiring snapshots. Furthermore, the intensity of the electron beam can be adjusted; this was set as low as possible such that the particles were still visible.

- Clustering
  Invariably, the particles were present in clusters when imaging. Since many of the images were of hard-sphere systems, this is due to the drying process, rather than any residual attraction as suggested previously [31]. As these sterically stabilised particles dry, the stabilising hairs will collapse onto the particle. This exposes the van der Walls attractive minimum and the particles will cluster if they come within the range of the van der Walls minimum. These unavoidable particle clusters make analysis difficult, so a protocol was developed to properly segment and analyse the particles. An outline of the analysis steps will be presented in the following section, with further details in Appendix A. When the polydispersity of the sample is large, the clustering can cause smaller particles to become hidden beneath large particles, for example in figure 4.7a).

  Related to this point, the concentration of particles in the sample is important: too low results in images such as figure 4.7d), where many images must be taken to achieve a suitable number of particles for statistically significant results. If the concentration of particles is too high the particles arrange in multiple layers of clusters . A representative

example this problem is shown in figure 4.7 c), where the darker region indicates that there are multiple layers of particles. While it is still possible to extract data from these images, large portions of the image must be excluded from the analysis and the contrast and image quality is not usually as good as images with well-spaced particle clusters.

Finally, the clustering of particles also implies the TEM grid is not covered uniformly with particles. This means that many snapshots across the entire grid must always be taken to ensure good data sampling.

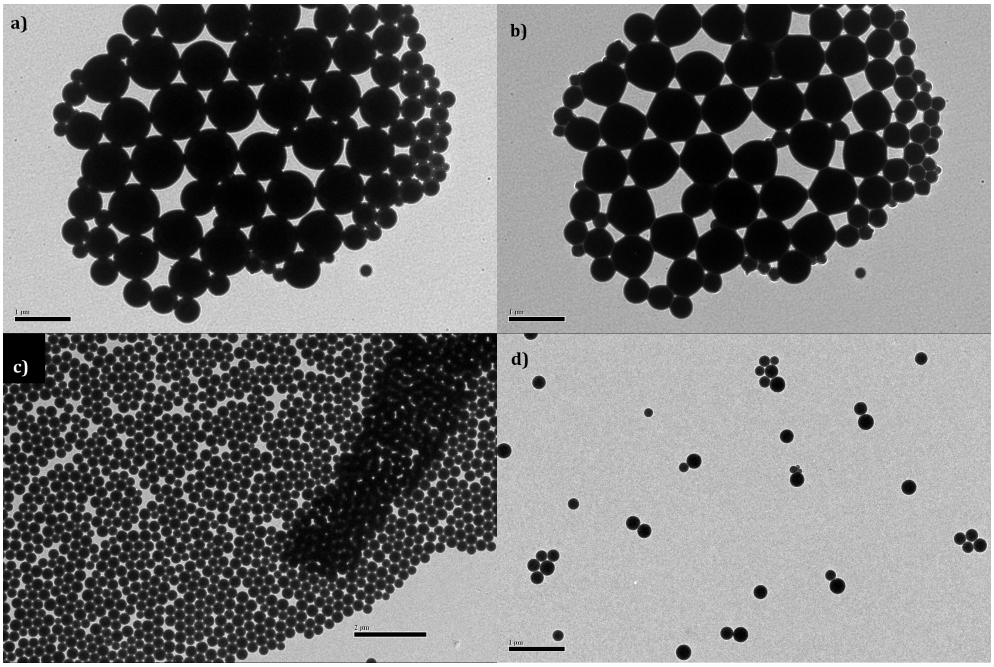

Figure 4.7 Example of different problems encountered when imaging PMMA particles for use in size distribution measurements: a) clustering of particles in highly polydisperse samples leads to the small particles becoming obscured, b) irradiation damage (melting) of the particles after a few seconds of exposure, c) too high sample concentration, leading to lower contrast and regions of stacked particles, d) low sample concentration, meaning many images must be taken to acquire a size distribution with good statistics. Methods of dealing with these problems are discussed in the text.

Experimental details

The technique detailed below was used to prepare all TEM samples. 3.05 mm copper grids were dipped into a dilute solution of particles and the solvent was allowed to evaporate. TEM was performed using the Phillips CM120 Biotwin in

the Wellcome Trust Centre Optical Instrumentation Laboratory at the University of Edinburgh. Micrographs were taken at 2850× magnification, such that each particle had a diameter of approximately 40 pixels; each image was taken at a well separated region of the grid in order to obtain a good approximation of the distribution.

The resultant images were processed in Fiji, a version of the open-source ImageJ software with added built-in macros [97, 98], to extract particle radii. Due to the clustering of particles, segmentation was not initially straightforward; many iterations of steps in Fiji were tried to obtain images with mostly correct particle segmentation. The results for each image were checked manually before the results were recorded. Once the analysis steps were determined, a macro was written in Fiji so that, other than the checking step, analysis could be performed at a reasonable speed. An example of the segmenting process is described below; further details can be found in Appendix A.

The following steps were taken to process the raw TEM images to extract the radius of each particle. The steps correspond to each numbered image in figure 4.8.

1. Load the image into Fiji.

2. Threshold the image. The contrast varied between images; to ensure the automatic thresholding did not erode the particles, each image was thresholded manually.

3. Despeckle. This step replaces each pixel with the median value in a 3×3 neighbourhood. This results in a smoothing of the edges of the particles and removes any 'salt and pepper' noise from the background.

4. Watershed. This algorithm calculates distance maps of each point to find maxima, erodes each maxima to a point, then dilates each point until the objects meet an edge or another growing object. This step is sufficient for images with few particles, but it misses small particles easily and can over-segment the particles. These over-segmented particles then need to be manually identified and removed from the analysis. There are many competing watershedding algorithms, some of which are reviewed in [93]. However, instead of trialling different algorithms, the following steps were found to minimise the number of over-segmented particles.

5. Find Edges. This step detects sharp changes in intensity and draws an outline.

6. Find Maxima. This works in a similar way to watershedding, with the advantage that a noise tolerance can be specified, so a single particle does not become split into two or more parts. This step has the option of outputting segmented particles, shown in image 6 of figure 4.8.

7. Analyse particles. This function outputs specified parameters of objects in the image, including x, y coordinates, area and roundness. For the particle radius measurements desired to obtain a size distribution, the Feret diameter parameter was used (discussed in Appendix A). The 'Analyse particles' function can then output numbered outlines of the measured particles.

8. Send overlay to ROI (region of interest) manager and overlay onto original image. The use of the ROI manager allows erroneous objects to be selected by clicking on the image. These objects can then be deleted from the image and the results. The results were contained in a text file, which was imported into Origin 8.5 for the size distribution analysis.

Errors in TEM radius measurement

The error in the radius measurement due to the processing technique is $\pm 1/20$ pixels per particle, or 5 %. With this in mind, the number of particles measured for each distribution was chosen such that the standard error in the mean was less than 5 %. For a particle of radius $R = 150$ nm, $S_E = R/\sqrt{N} < 5$ % when $N = 500$, dropping to 3 % for $N = 900$. Since the average radius was not known in advance, and the error increases as R increases, typically a goal of 1000 particles was chosen for the TEM distribution analysis.

In conclusion, a robust processing and analysis technique was developed using Fiji to extract size distribution measurements from TEM images [97]. All of the size distributions in this thesis were obtained using this method. Additionally, the parent ASM320 particles and the phase-separated samples in chapter 6 were also characterised using small-angle x-ray scattering, as discussed earlier in this chapter. TEM distributions have the advantage of measuring directly the distribution, while SAXS scattering analysis obtains the *in situ* characteristics

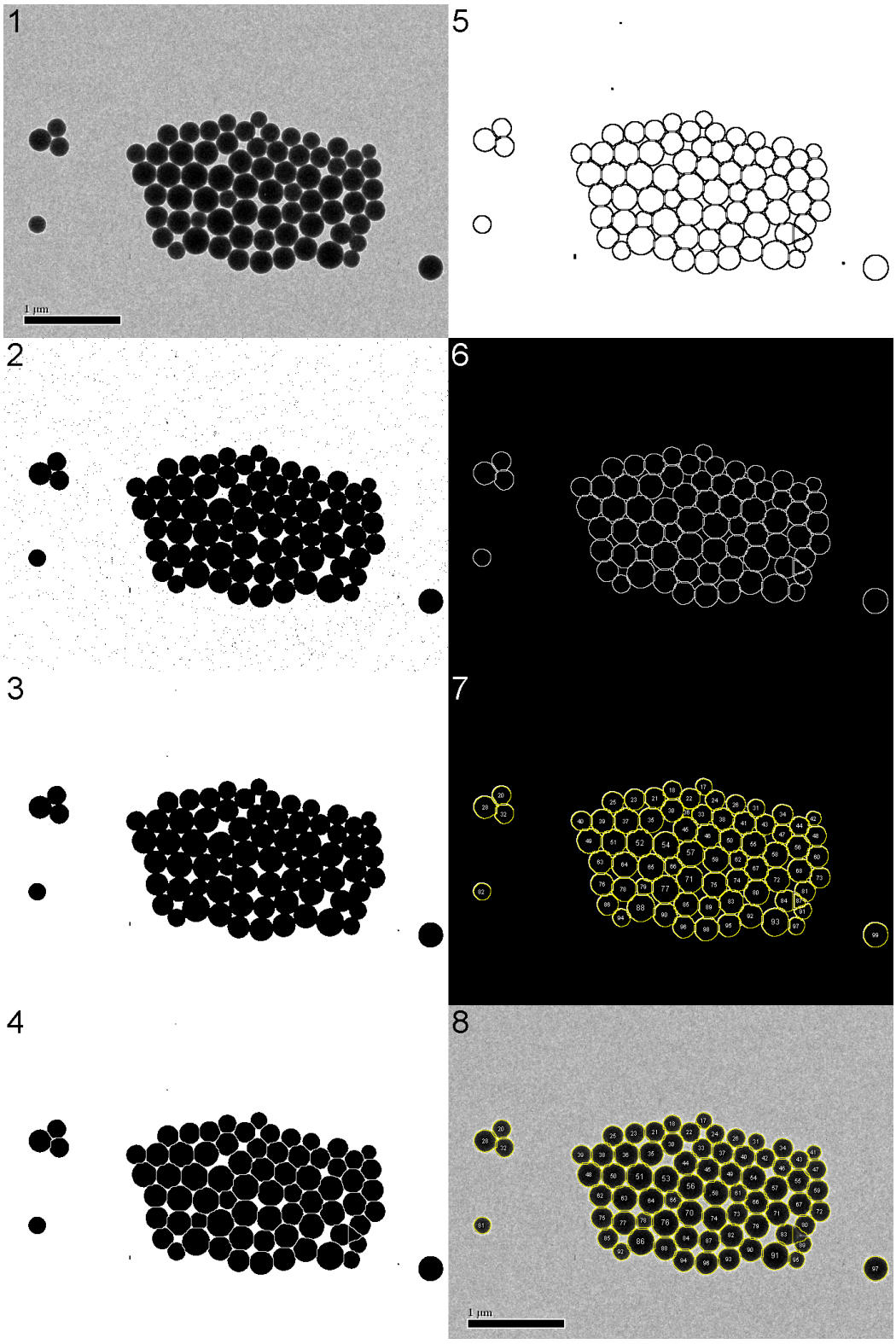

Figure 4.8 TEM analysis steps as described in the text.

of the particles. A method of combining the advantages of these two methods, calculating form factors using the directly obtained TEM size distributions, will be presented in chapter 6.

4.3 Dynamic Light Scattering

Dynamic light scattering was used to investigate the novel phases observed in hard-sphere experiments. These phases were not crystalline and appeared not to act like glasses - they flowed - but were at a volume fraction where we would expect samples to either be crystalline or glass. The dynamics of these phases were probed using 3d dynamic light scattering, and the results will be presented in chapter 5.3. This section contains a short introduction to dynamic light scattering and techniques used to reduce multiple scattering when the samples are turbid or concentrated.

4.3.1 Introduction

When coherent light is passed through a scattering medium, a scattering pattern is produced and can be used to identify particular phases. For example, a transient gel has a characteristic scattering ring of high intensity, which becomes brighter and eventually collapses [80]. A random configuration of particles will produce a 'speckle' pattern of regions of constructive interference, which fluctuate as the particles move. By studying the time correlation function of speckles of scattered intensity, information about the dynamics can be extracted.

The fluctuating intensity-time correlation between starting time, t, and delay time, τ, is given by

$$\langle I(\mathbf{q},0)I(\mathbf{q},\tau)\rangle = \lim_{T\to\infty}\frac{1}{T}\int_0^T \mathrm{d}^3 r I(\mathbf{q},t)I(\mathbf{q},t+\tau). \tag{4.31}$$

For $\tau = 0$, this equation reduces to

$$\lim_{\tau\to 0}\langle I(\mathbf{q},0)I(\mathbf{q},\tau)\rangle = \langle I^2(\mathbf{q})\rangle \tag{4.32}$$

and for delay times much longer than the fluctuation time of the intensity, the

speckles are uncorrelated, so

$$\lim_{\tau\to\infty}\langle I(\mathbf{q},0)I(\mathbf{q},\tau)\rangle = \langle I(\mathbf{q})\rangle^2. \tag{4.33}$$

The quantity measured in experiments is the normalised time correlation function of the scattered intensity, $g^{(2)}(q,\tau)$:

$$g^{(2)}(q,\tau) = \frac{\langle I(\mathbf{q},0)I(\mathbf{q},\tau)\rangle}{\langle I(\mathbf{q})\rangle^2}, \tag{4.34}$$

which is related to the normalised time correlation function of the scattered *field*, $g^{(1)}(q,\tau)$ by the Siegert relation:

$$g^{(2)}(q,\tau) = 1 + [g^{(1)}(q,\tau)]^2. \tag{4.35}$$

$g^{(1)}(q,\tau)$ is also known as the measured intermediate scattering function, $f^M(q,t)$ and is defined as

$$f^M(q,\tau) \equiv g^{(1)}(q,\tau) \equiv \frac{\langle E(\mathbf{q},0)E^*(\mathbf{q},\tau)\rangle}{\langle I(\mathbf{q})\rangle}. \tag{4.36}$$

Equation 4.35 is applicable to any fluid system where the spatial correlation range is small. In practice, not all of the signal reaches the detector, so an intercept, β, is introduced. This consists of many factors and it can be used as a judge of the data quality. Thus equation 4.35 becomes

$$g^{(2)}(q,\tau) = 1 + \beta[g^{(1)}(q,\tau)]^2. \tag{4.37}$$

The plots presented later in this thesis are in terms of $(g^{(2)}(q,\tau)-1)$ against delay time. The curves are normalised such that they have a maximum of 1 when $\tau = 0$ and will decay to zero for ergodic (uncorrelated) systems. In glassy systems, the particles are caged over long times and are thus effectively correlated. In these non-ergodic systems $g^{(2)}(q,t)$ exhibits a plateau at a non-zero value.

Furthermore, for non-ergodic systems, the time average does not equal the ensemble average of the system, so to obtain an ensemble-averaged $g^{(2)}(q,\tau)$, further steps must be taken. One common technique, employed by Martinez *et. al.*, is to determine $g^{(2)}(q,\tau)$ (or $f^M(q,\tau)$) of the fast, initial decay process and the slow, non-ergodic plateau separately [66]. This method is valid for hard-sphere colloidal glasses, where there is a well-defined plateau of the correlation

function as $\tau \to \infty$. However, many of the samples probed by DLS in this thesis had dynamics which had both non-ergodic and ergodic features; the correlation functions exhibited plateau-like behaviour but eventually decayed to zero at long times. These correlation functions will be presented in chapter 5.3.

In order to obtain ensemble-averaged correlation functions in the partially ergodic samples, a 'brute force' method was applied [77]. This method consists of measuring $g^{(2)}(q,\tau)$ for many speckles, i, in the sample, then calculating the intensity-weighted average of each dataset:

$$g^{(2)}_{av}(q,\tau) = \frac{g^{(2)}_i(q,\tau) I^2_i(q)}{N\langle I\rangle^2}, \tag{4.38}$$

where the average ensemble intensity, $\langle I\rangle$ is related to the average intensity at each detector, I_1 and I_2, and the ratio of the measured to ideal (detector) intercepts:

$$\langle I\rangle = \sqrt{I_1 I_2 \frac{\beta^{measured}}{\beta^{ideal}}}. \tag{4.39}$$

The mathematical treatment in this section is valid under the assumption that the incident light is scattered only once in the scattering medium, that is when the system is dilute or when the refractive index of the scatterers closely match that of the solvent. It is possible to perform DLS on turbid or concentrated samples, but a different experimental set up is required to counteract the effects of multiple scattering. Two cross-correlation methods are described in the following section: two-colour (TC) and three-dimensional (3d) dynamic light scattering.

4.3.2 Two colour dynamic light scattering

In TC DLS, two lasers, i and ii with different wavelengths are set up in plane, with two detectors, 1 and 2. The different wavelengths of light will scatter with different angles, and the detectors are set up such that singly scattered light with the same q vector are detected with each detector. This is illustrated in figure 4.9. Light of the wrong wavelength is blocked from entering the other detector.

The cross correlation function of detectors 1 and 2, G^{TC}_{12}, (equation 4.31) can now

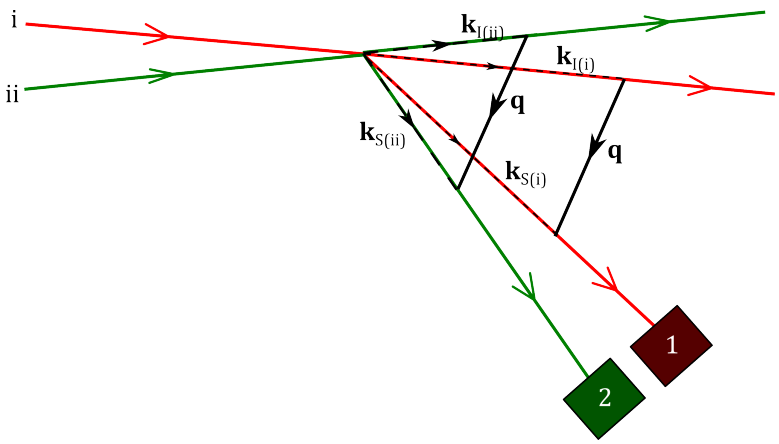

Figure 4.9 Scattering of light in a two-colour dynamic light scattering setup. The detectors are arranged such that scattered light from laser i (red) entering detector 1 has the same q vector as light from laser ii(green) entering detector 2.

be split into four components:

$$\begin{aligned} G_{12}^{TC} =& \langle I_1^i(0) I_2^i(\tau)\rangle + \langle I_1^i(0) I_2^{ii}(\tau)\rangle + \\ &+ \langle I_1^{ii}(0) I_2^i(\tau)\rangle + \langle I_1^{ii}(0) I_2^{ii}(\tau)\rangle. \end{aligned} \tag{4.40}$$

Since only light of the correct wavelength is allowed to enter each detector, the only non-zero contribution to the correlation function is when light from i enters detector 1 at the same time as light from ii enters 2. Thus for singly-scattered light, equation 4.40 becomes

$$G_{12}^{TC} = \langle I_1^i(0) I_2^{ii}(\tau)\rangle \tag{4.41}$$

and the normalised correlation function is given by

$$g_{12}^{(2)TC}(\tau) = \frac{\langle I_1^i(0) I_2^{ii}(\tau)\rangle}{\langle I_1\rangle\langle I_2\rangle} \tag{4.42}$$

$$= 1 + \beta_{TC}[g_{12}^{(1)}(\tau)]^2. \tag{4.43}$$

Where $\beta_{TC} = \beta$ has the same theoretical maximum of 1. Because equation 4.42 is now of the form of equation 4.37, which was applicable in the single-scattering limit, it implies the data can be interpreted in the same way as in the single-scattering limit. Unfortunately, while two colour methods work well [82], the experimental work is technically demanding, and requires very careful alignment of the two lasers [105].

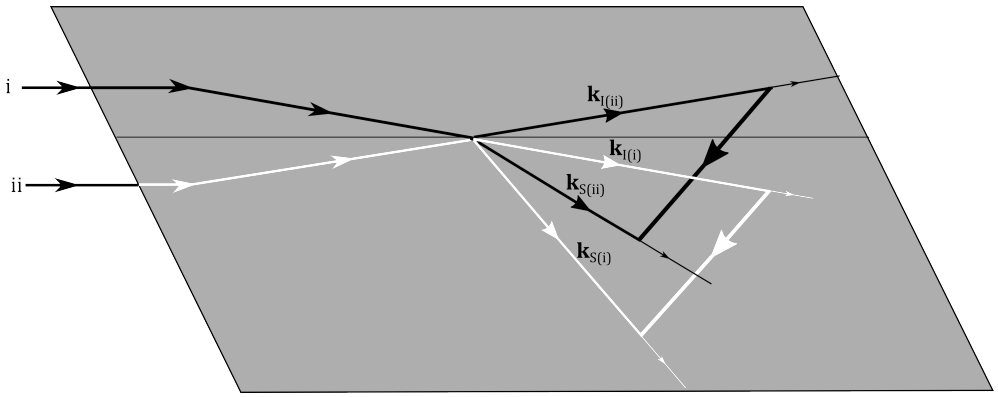

Figure 4.10 Scattering of light in a 3d dynamic light scattering setup. One laser beam is split into two and focussed on the same point in the scattering volume. The detectors are arranged such that scattered light from beam i entering detector 1 has the same $\mathbf{q}$ vector as light from laser ii entering detector 2. The white lines represent scattering below the (grey) plane, while black lines are scattering above the plane.

4.3.3 3 dimensional dynamic light scattering

3d DLS is a similar cross-correlation technique to TC DLS described above but only one laser is used. The laser beam is split such that the two beams are incident outside of the usual scattering plane. The incident beams are focussed on the same point in the sample, as illustrated in figure 4.10. The detectors are set up such that scattered light with the same q vector are correlated.

The normalised time correlation function of the scattered intensity (ICF) can be found as follows: the cross correlation function can again be split into four parts but, in contrast to the TC DLS set up, all scattered light reaches the detector. The uncorrelated terms each contribute a term to the background:

$$\begin{aligned} G_{12}^{3d} =& \langle I_1\rangle\langle I_2\rangle + \langle I_1^i(0) I_2^{ii}(\tau)\rangle + \\ &+ \langle I_1\rangle\langle I_2\rangle + \langle I_1\rangle\langle I_2\rangle \qquad (4.44) \\ =& \langle I_1^i(0) I_2^{ii}(\tau)\rangle + 3\langle I_1\rangle\langle I_2\rangle. \qquad (4.45) \end{aligned}$$

Therefore the normalised ICF is

$$g_1^{(2)3d}2(\tau) = \frac{\langle I_1^i(0)I_2^{ii}(\tau)\rangle + 3\langle I_1\rangle\langle I_2\rangle}{\langle I_1^i + I_1^{ii}\rangle\langle I_2^i + I_2^{ii}\rangle} \tag{4.46}$$

$$= \frac{\langle I_1^i(0)I_2^{ii}(\tau)\rangle + 3\langle I_1\rangle\langle I_2\rangle}{\langle I_1^i I_2^{ii}\rangle + \langle I_1^i I_2^i\rangle + \langle I_1^{ii} I_2^i\rangle + \langle I_1^{ii} I_2^i\rangle}$$

$$= \frac{\langle I_1^i(0)I_2^{ii}(\tau)\rangle + 3\langle I_1\rangle\langle I_2\rangle}{4\langle I_1\rangle\langle I_2\rangle}$$

$$= \frac{1}{4}(1 + \beta[g_{12}^{(1)}(\tau)]^2) + \frac{3}{4}$$

$$= 1 + \frac{\beta}{4}[g_{12}^{(1)}(\tau)]^2. \tag{4.47}$$

Equation 4.47 implies that the maximum theoretical intercept of a 3d DLS experiment is $\beta_{3D} = 0.25\beta = 0.25$ [96, 116]. In practice it is a lot lower; it can be difficult with highly concentrated samples to obtain data with an intercept large enough to be significant. 3d DLS was used in experiments on concentrated hard sphere colloidal systems, presented in the following chapter.

Chapter 5

Polydispersity effects in hard-sphere colloids

The phase behaviour of monodisperse hard spheres has long been known. While there has been a substantial amount of theory and simulations regarding polydisperse hard spheres, as discussed in chapter 3, there is still a lack of experimental data to verify these simulations and theories. Presented here is a detailed observational study of polydisperse hard sphere phase behaviour, followed by an investigation into possible fractionation of particles between coexisting fluid and solid phases over time. A new phase at high volume fractions, between coexisting fluid-solid and glassy behaviours, is identified and the dynamics of this frustrated fluid phase are studied in the second part of the chapter.

Two batches of particles (PMMA suspended in decalin, as detailed in chapter 4) were used in these experiments: ASM295 had mean radius $R_{295} = 108(5)$nm and polydispersity $\sigma = 11(1)\%$, while the ASM320 had mean radius $R_{320} = 124(4)$nm and $\sigma = 12(1)\%$, both determined by TEM. The technique for extracting particle size distributions from TEM images was described in chapter 4.2.2. The distributions for both batches of particles are shown in figure 5.1.

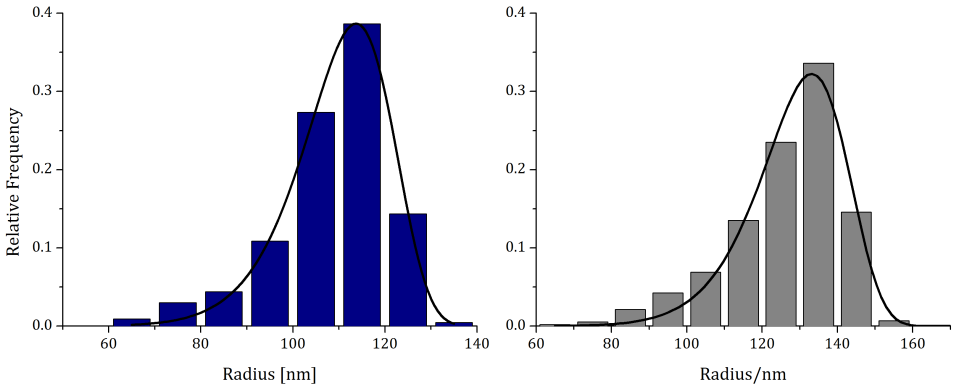

Figure 5.1 Distributions of ASM295 (left) and ASM320 (right) particles as determined by transmission electron microscopy. $\overline{R}_{320} = 124(4)$ nm and $\sigma_{320} = 12(1)\%$, $\overline{R}_{295} = 108(5)$ nm $\sigma_{295} = 11(1)\%$. The line are the best-fit Weibull distributions to the data: $\overline{R}^{\text{fit}}_{320} = 129$ nm and $\sigma^{fit}_{320} = 10\%$; $\overline{R}^{\text{fit}}_{295} = 110(5)$ nm $\sigma^{\text{fit}}_{295} = 9.8(4)\%$.

5.1 Phase behaviour

5.1.1 Experimental details

ASM320 particles were used to determine the hard-sphere phase behaviour. A single vial of particles were prepared from "Batch E", a 30 ml vial of ASM320 particles in decalin, which had volume fraction of $\phi = 0.505$, as determined by centrifuging the particle suspension and measuring the height of the randomly close packed sediment. To achieve an initial volume fraction above that of $\phi_m^{\text{mono}} = 0.545$, 1.19 ml of the parent suspension was pipetted into a 1.8 ml cylindrical glass vial. This vial was placed into the centrifuge at 2500 rpm until the particles formed a close-packed sediment. 0.19 ml (0.1647 g) of decalin was then removed, such that the volume fraction of particles was $\phi_0 = \frac{0.505 \times 1.19}{1} = 0.601$. The particles were redispersed using a whirlmixer for 5 minutes, then placing the vial on the rollerbank overnight.

When the particles were suitably re-dispersed, the vial was placed in an incubator set at 298 K and left undisturbed for 5 days. At this point, observations were made and recorded, then the particle suspension was diluted by the addition of two drops of decalin. The particles were again re-dispersed using the whirlmixer and rollerbank before replacing the vial in the incubator for observations. This process was repeated until the entire phase space had been explored. The observation

time for each "dilution" (where dilution 0 refers to the initial vial prepared at $\phi = 0.601$) was typically 5 days, with longer observation times for those dilutions which crystallised. Intermediate observations were also made and recorded, as described below. The final observation for each dilution with the designated phase behaviour is illustrated in figure 5.2. The height of each phase was measured using an upright vernier calliper and converted to percentage height of the particle suspension.

5.1.2 Observed phase behaviour

Dilutions 0 and 1 exhibited glassy behaviour - the particles had an uneven particle-air interface which showed no noticable movement (due to gravity) after 5 days. Furthermore, the interface remained stationary relative to the vial bottom when the vial was inverted and air bubbles were observed in the bulk of the suspension. These two dilutions required repeated whirlmixing to satisfactorily redisperse the particles.

Dilutions 2 to 4 exhibited similar behaviour to one another: they appeared initially glass-like, with no signs of bulk crystallisation after 5 days. Dilution 4 was left for 6 days, after which time a few small crystallites were observed around the meniscus. These crystallites were small and difficult to see, so it is not clear if they were present at earlier times. Despite the lack of crystallisation and high volume fractions, these dilutions were not designated as glasses because the particle-air interface moved (albeit sluggishly) when the vial was angled. Dilution 5 also appeared to have similar behaviour to $2, 3$ and 4, with no crystallites observed after 5 days. After 13 days, however, a few crystallites were observed at the very top of the particle suspension. Similarly, crystallites were visible at the top of the particle suspension of dilution 6 after 4 days. By 6 days a few more crystallites were visible, but only at the top of the suspension. The lack of bulk crystallisation and retarded movement of the particles when the vial was angled was common between dilutions 2 to 6; the phase was described as a *frustrated fluid* and will be investigated further in section 5.3.

Dilutions 7 to 10 showed coexisting fluid and solid (crystal) phases. Dilution 7 was the first in the dilution series to have any visible crystallites in the bulk of the suspension; crystallites were visible after 2 days, and had started to sediment out after 3 days. By 5 days, crystallites were visible at all heights in the suspension. After 14 days there was not a sharp crystal-fluid interface but

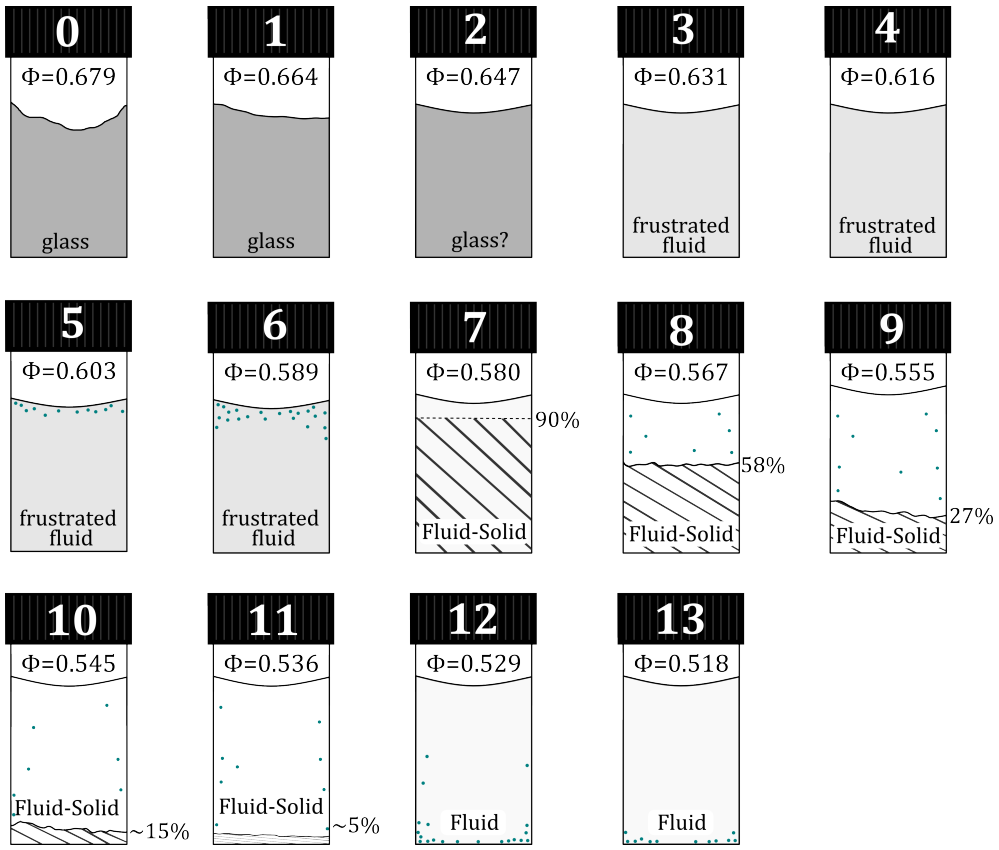

Figure 5.2 Illustration of a series of dilutions of ASM320 sample $24A$; polydisperse, hard-sphere PMMA particles. The numbers at the top of each vial indicate the dilution number, and the volume fractions are corrected such that dilution 7 has $\phi = 0.580$. A description of the phase behaviour for each dilution can be found in the text.

most of the crystallites were in the crystal phase. There was also a small region at the bottom of the vial which appeared devoid of crystallites, possibly due to compression from the crystal layer above.

Crystallites in the fluid-solid samples became visible faster with decreasing volume fraction: in dilution 8, they were visible towards the top of the vial after 1 day and at all heights after 2 days. By 8 days, the crystallites appeared to be sedimenting (more were visible towards the bottom). By 10 days the layer was almost measurable , but again a sharp interface between the fluid and solid phases was not present. The height of the solid phase was recorded after 13 days, although there were still a small number of crystallites visible in the bulk of the suspension. Dilution 9 exhibited similar behaviour to 8, in that crystallites were observed after 1 day in the top half of the suspension and at all heights after 2 days. After 5 days the crystallites had visibly sedimented but there were still many in the bulk. At the point when the heights were recorded for this

dilution (12 days), the fluid-solid interface was uneven and there were still a few crystallites visible in the fluid phase.

Visible crystallites were observed in the top half of the particle suspension in dilution 10 after 1 day and at all heights after 2 days, although there were markedly less crystallites than in previous dilutions. The heights were recorded after 8 days for this dilution, since the majority of visible crystallites had sedimented out by this point. Dilution 11 was the last to convincingly exhibit fluid-solid phase behaviour. The first crystallites were visible after 2 days at the top of the suspension and at all heights after 3 days, although again the number of crystallites observed was small. After 12 days, when the heights were recorded, there was a very small crystal phase with an uneven fluid-solid interface. There were also a few smaller crystallites visible on the walls of the vial.

Dilutions 12 and 13 contained a few crystallites but these were mainly on the walls and bottom edges of the vial. Figure 5.2 shows the appearance after 7 days for these two dilutions; they were designated single-phase fluids.

5.1.3 Discussion

The difficulties of measuring volume fractions were discussed in sections 2.2.1 and 3.1.4. The method used for these experiments was to make an initial estimate of the volume fraction by centrifuging the particle suspension and assuming the random-close-packed sediment had volume fraction $\phi_{rcp} = 0.64$. Subsequent dilutions are then precice and accurate relative to the reference volume fraction. In order to obtain a more accurate reference point, the dilution with the highest percentage of crystal phase was chosen to have volume fraction ϕ_m. Referencing Fasolo and Sollich's hard-sphere polydisperse phase behaviour calculations (3.1, page 23), the highest possible volume fraction of a single-phase polydisperse crystal is $\phi_m = 0.58$. This will of course introduce a further systematic error to the final volume fractions. The resultant volume fractions for dilutions 0 to 13 are shown in table 5.1, along with the volume fraction initially calculated relative to $\phi_0 = 0.601$.

The random errors in the volume fraction calculations originate from the measured mass and density of the decalin added (hence the calculation of the total volume of each dilution) and the measured height of the close-packed sediment. These lead to an error of 0.896%, which translates to $\phi = \phi \pm 0.005$.

Table 5.1 Experimental volume fraction, determined using $\phi_1 V_1 = \phi_2 V_2$. The initial volume fraction was calculated using this equation relative to the parent volume fraction, determined by the centrifugation/random-close-packed method. The corrected volume fractions were calculated by setting $\phi_7 = 0.580$, as discussed in the text. The random error on each volume fraction is ± 0.005.

Dilution number	0	1	2	3	4	5	6
ϕ_{exp}	0.601	0.588	0.573	0.558	0.545	0.533	0.521
ϕ_{corr}	0.679	0.664	0.647	0.631	0.616	0.603	0.589
Dilution number	7	8	9	10	11	12	13
ϕ_{exp}	0.512	0.502	0.491	0.482	0.474	0.468	0.458
ϕ_{corr}	0.580	0.567	0.555	0.545	0.536	0.529	0.518

The height of the solid phase is plotted as a function of (corrected) volume fraction in figure 5.3. Assuming the percentage of solid phase increases linearly across the fluid-solid coexistence gap, a straight line was fitted to the percentage heights corresponding to dilutions 7 to 12 in Excel. Using the inbuilt LINEST function, the equation for the straight line is $y = 2511\phi - 1366$. The width of the coexistence gap was then calculated as $\Delta\phi = \phi_{y=100} - \phi_{y=0} = 0.584 - 0.544 = 0.040(5)$.

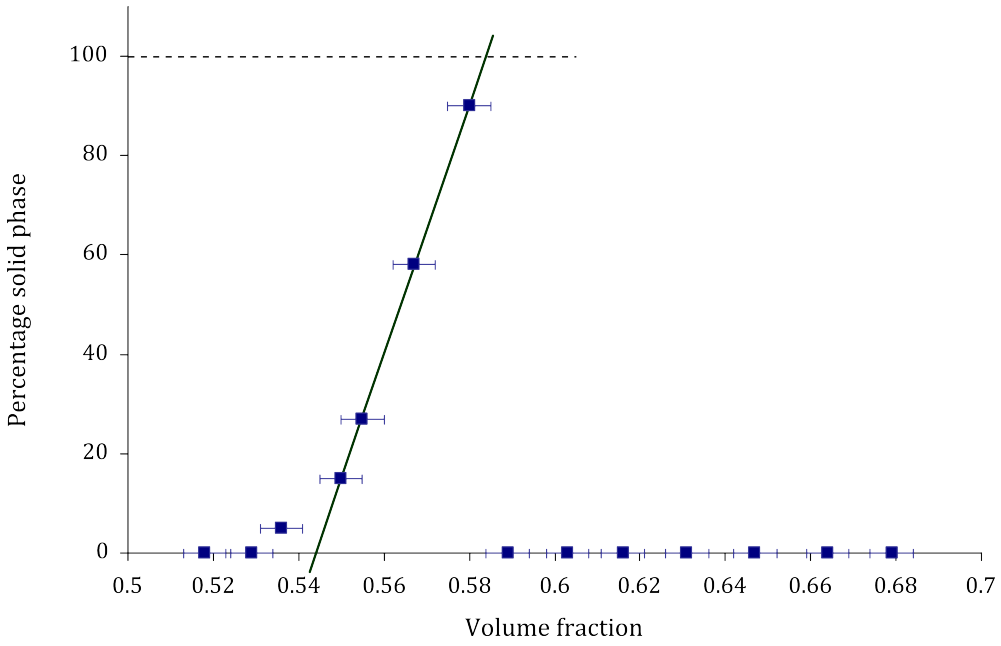

Figure 5.3 Plot of percentage crystal height *vs.* (corrected) volume fraction for dilutions 0 to 13, corresponding to figure 5.2. The line is a linear fit to the heights of dilutions 7 to 10.

This result is smaller than the width of the coexistence gap in the monodisperse case, $\Delta\phi_{mono} = 0.545 - 0.494 = 0.051$. There have been few studies of fluid-solid coexistence gaps in polydisperse systems; the system closest to ours is that studied

by Fairhurst, who measured the coexistence gap in a system of PMMA particles with 9.5% polydispersity [31]. When using solvents to match the refractive index of the particles, the value of the coexistence gap was $\Delta\phi = 0.041$, consistent with our results. However, the same particles in a cis-decalin (so more directly comparable with our system) had a smaller coexistence gap of $\Delta\phi = 0.03(1)$.

Taking another qualitative look at figure 3.1 on page 23, the width of the coexistence region should not narrow considerably. At values up to $\sigma \approx 6\%$, the gradients of the fluid and solid boundaries have similar steepness; the coexistence region shifts to higher ϕ but remains approximately the same width. Above 6%, the polydispersity of the fluid boundary increases at a constant rate with increasing volume fraction, then rapidly increases for $\sigma \gtrsim 10\%$. At these high polydispersities, the single phase solid is no longer an equilibrium phase; the boundary for coexisting fluid-solid-solid approaches from the right. Part of the FSS phase should be accessible in experiments, since it exists at volume fractions lower than that of the colloidal, hard-sphere glass transition, $\phi_g = 0.58$. The outcome of this combination of features is that the FS coexistence region should narrow for polydispersities $\gtrsim 10\%$ but any experimental coexistence region could also include FSS behaviour.

Fairhurst's PMMA, 9.5% polydisperse particles in cis-decalin underwent a FS transition over a narrower range of volume fractions than the monodisperse case, as expected [31]. The particles investigated in this section ($\sigma = 12\%$) had a larger coexistence gap than Fairhurst's particles, even though Fasolo and Sollich's work suggests the fluid-solid region should in fact have narrowed significantly at polydispersities $> 10\%$. Therefore, the apparently increased coexistence gap is consistent with the observation of both FS and FSS phases within the "coexistence region".

Fasolo and Sollich made detailed calculations for the volume fractions of coexisting phases for particles with parent polydispersities of 4 and 8%, as shown in figure 5.4. For the "effectively monodisperse", 4% polydispersity particles, the volume fractions of coexisting fluid and solid phases remain constant across the coexistence gap. When $\sigma = 8\%$, the volume fraction of the fluid increases more rapidly with increasing parent volume fraction than the coexisting solid: when $\phi_{Parent} = 0.56$, $\phi_F = 0.544$ (blue dashed line in figure 5.4) and $\phi_S = 0.579$ (red dashed line). However, when $\phi_{Parent} = 0.57$, the volume fraction of the fluid, $\phi_F = 0.552$ and $\phi_S = 0.584$[1]. The important point to note here is, while the width

[1]This should not be confused with the width of the coexistence region, which remains

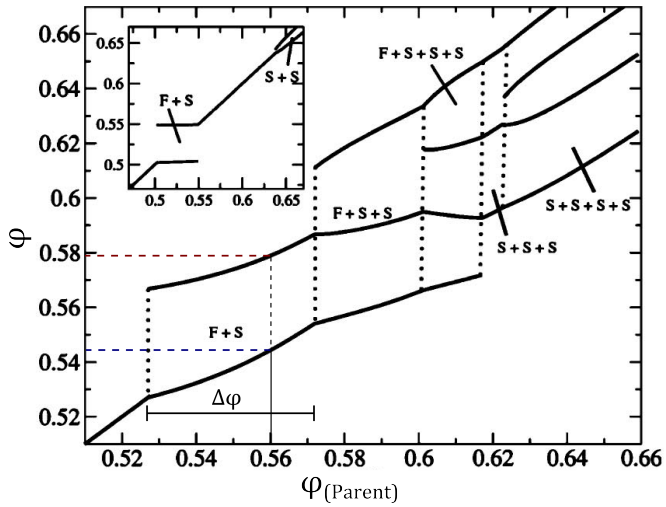

Figure 5.4 Volume fractions of coexisting phases plotted against parent volume fraction for particles with 8% polydispersity (main figure) and 4% polydispersity (inset). Dashed lines have been drawn on to denote the equilibrium volume fraction of one particular coexisting solid (red) and fluid (blue) with parent volume fraction of 0.56; also marked is the width of the coexistence gap, $\Delta\phi$. Taken from [33].

of the FS coexistence gap narrows slightly, the volume fraction of the coexisting solid could have ϕ greater than $\phi_g = 0.58$, so if the colloidal glass transition intervenes , crystallisation may not be possible at all volume fractions across the coexistence region. This would account for the experimental observation that no vial with 100% solid phase was observed.

In the same publication, Fasolo and Sollich also plotted average particle radius $\overline{R}$, normalised to the average radius of the parent size distribution, again for $\sigma = 8\%$. This has been reproduced in figure 5.5. This figure tells us that any coexisting solid in the FS region should contain particles with larger than average radius than those in both the parent and the coexisting fluid. This difference is less than 4% for this example, but is expected to be at least 6% between fractionated solids in the FSS region. Therefore, if significant size fractionation is observed in the experimental system, it can be taken as evidence for the observation of FSS behaviour.

Sollich and Wilding's 2011 follow-up to reference [33] considered multiple solid transitions in more detail [109]. Their work echoed the findings of [33] - the width of the coexistence region does not narrow severely with increasing polydispersity and size fractionation between coexisting fluid and solid should be observed at

constant: $\Delta\phi = 0.572 - 0.526 = 0.046$.

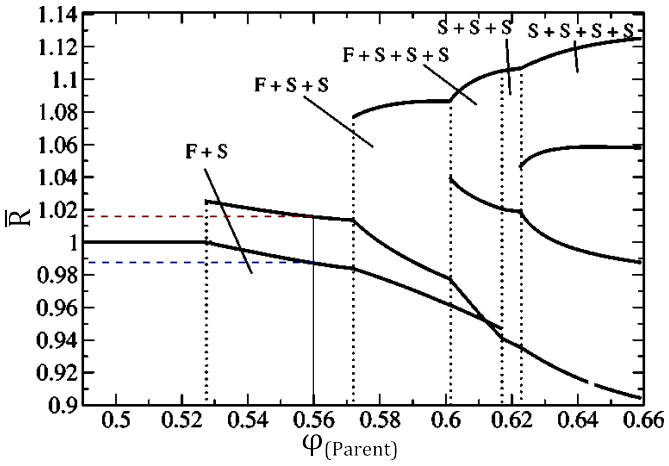

Figure 5.5 Average radius $\overline{R}$ of coexisting phases, normalised to the average radius of the parent particles, plotted against parent volume fraction. The parent particles have 8% polydispersity. Dashed lines have been drawn on to denote the average radius of coexisting fluid (blue) and solid (red) phases for a parent volume fraction of 0.56. Taken from [33].

equilibrium.

Furthermore, Sollich and Wilding claim that their work shows conclusive evidence that dense polydisperse spheres demix into coexisting, face-centre-cubic, solid phases. However, they suggest that since multiple solids are unlikely to be observed alone in experimental systems (due to the large scale rearrangements required), it may be necessary to focus on coexisting fluid plus solid phases, where the fluid phase can serve to transport particles to their preferred solid phase.

Thus, to develop a more convincing interpretation of my experimental results as observation of experimental fluid-solid-solid behaviour, we should consider the possibility of fractionation between coexisting fluid and solid phases.

5.2 Fractionation

In general, polydisperse suspensions fractionate upon phase separation. That is, different phases contain particles with different distributions of properties. Size-disperse hard-sphere particles are expected to fractionate such that the solid phase has larger, more monodisperse particles than the coexisting fluid [34]. Previous investigations using light scattering techniques did not reveal any significant fractionation [31] after a period of 21 days, but it is possible that small changes in distribution shape would not have been detected using light scattering, or that

fractionation occurs over a timescale longer than that of the previous experiments. One way to investigate these possibilities is to set up a time series of samples and use transmission electron microscopy to measure the size distributions of particles in the coexisting phases at each time point.

5.2.1 Experimental details and results

ASM295 particles were used in these experiments. These particles were chosen due to their similar distribution to ASM320 particles (figure 5.1). The phase behaviour of these particles was determined using the method described in the previous section and two vials were prepared for each volume fraction such that if the particles from one vial were extracted for electron microscopy, there would be another with identical properties available for long-time observations.

To study the size fractionation of particles between coexisting fluid and solid phases, a sample with a significant layer of particles after a few days was chosen. Six more vials with the same volume fraction as this sample ($\phi_{corr} = 0.559$, similar to Dilution 9 of figure 5.2) were then prepared to create a time series.

The particles started to crystallise within a few days and had a solid layer with a clear, measurable (but not sharp) interface after ≈ 5 days. A series of six samples, from 5 to 28 days were prepared. Also included in the analysis was the sample from the volume fraction series used to determine the phase behaviour of these ASM295 particles, which had by this point been left undisturbed for 120 days. The 120 day sample is obviously not at the exact same volume fraction as the rest in this time series, but the volume fraction of particles in each vial in the time series was prepared such that it was equivalent to this 'original' sample. The vials were set up and each was homogenised at the appropriate time, such that all could be observed and extracted on the same final day[2]. Observations of crystal height and appearance are illustrated in figure 5.6.

Crystallites were visible in the bulk of the suspension after 1 day. The number of crystallites had visibly increased after 2 days, and had started to sediment out after 3 days. After 5 days, there was a measurable layer of sedimented crystallites at the bottom of the vial, but there were still crystallites visible at all heights in the fluid phase. Those at the top of the sample appeared smaller than those

[2]This method was used rather than taking observations every 5 days so that sample-to-sample differences (for example the size of crystallites) could be directly compared.

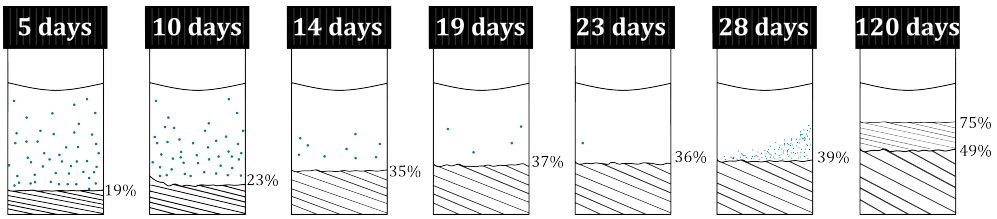

Figure 5.6 Illustration of a time series of ASM295 - polydisperse, hard-sphere PMMA particles. The volume fraction of this sample is $0.559(5)$. The percentage vial height of the solid phase is included in the figure; the small points signify crystallites in the bulk or on the wall of the vial, as described in the text. After 120 days, a second crystal phase is observed, with visibly more heterogeneous crystallites than those in the bottom solid phase.

which had sedimented. The next time-point was 10 days: in this sample the crystal layer was much more defined although the interface was very uneven and there was a region on one side of the vial which was visibly higher than the rest of the crystal layer. There were still crystallites in the fluid phase, but far fewer than in the 5 day sample; it was difficult to ascertain if there were any crystallites near the meniscus.

By 14 days, almost all of the visible crystallites had sedimented out of the fluid and were contained in a single solid phase. The fluid-solid interface was visibly uneven and there were still a few crystallites visible in the fluid phase. The appearance of the 19 day sample was very similar to that of day 14, but the interface was less uneven and there were very few crystallites visible in the fluid phase.

At day 23, the solid layer was very clear but still uneven and there was no visible sedimentation of the fluid around the meniscus. Between 23 and 28 days, smaller (more difficult to observe) crystallites started to appear. It was not clear whether these were on the wall or in the bulk of the sample and the crystallites were distributed irregularly, as illustrated in figure 5.6. After 120 days, two visibly different solid layers are present within the sample. The bottom layer was similar in appearance to the solid layers at earlier times; large crystallites of visibly similar sizes, separated from the phase above by a rough interface. The second solid phase had much more heterogeneous crystals and appeared 'shiny'. This again had a clear but rough interface separating it from the fluid phase above. All three of the regions in this sample were extracted for size distribution analysis.

Dilute suspensions of each phase were prepared for TEM in the following way: A

clamp stand was set up such that the vial could be illuminated from the bottom, using a swan-necked lamp. A small amount of the fluid phase was extracted using a Pasteur pipette and 3 drops of this particle suspension was then transferred to a vial containing 30 ml decalin; the remaining particles were discarded. The same pipette was used to extract the remainder of the fluid phase and those particles around the FS interface. A new pipette was then inserted into the bulk of the solid phase and a dilute suspension of the solid phase was prepared. While this technique destroys the sample, it ensures that only the desired phase is extracted and reduces any effects which may arise from disturbing the fluid-solid interface. All three regions of the 120 day sample were extracted in this way.

TEM grids were prepared from the diluted phases and were imaged on the same day. The resultant histograms of particle sizes is shown in figure 5.7; the average size and polydispersity of each phase is summarised in table 5.2

Table 5.2 Average core radius ($\overline{R}$) and polydispersity (σ), as determined from TEM measurements, for samples with volume fraction $\phi = 0.559(5)$ at different times. The parent particles had $R_{TEM} = 108(5)$ nm and $\sigma_{TEM} = 11(1)\%$.

Time [days]	Phase	$\overline{R}$ [nm]	σ [%]
5	F	106(4)	13
	S	106(3)	12
10	F	107(4)	13
	S	106(3)	13
14	F	108(4)	14
	S	106(4)	14
19	F	107(5)	13
	S	106(4)	12
23	F	106(4)	14
	S	109(4)	12
28	F	108(4)	13
	S	107(4)	13
120	F	103(4)	15
	S	106(3)	14
	S	107(4)	13

5.2.2 Discussion and conclusions

The first thing to note is all of the results in table 5.2 have polydispersities greater than the parent polydispersity of 11%. This distribution was obtained from 442 particles, giving a standard error in the mean of 4.7%. While this is reasonable, it is possible that the sample size was too small to properly sample the population

Figure 5.7 TEM distributions for coexisting fluid (top) and solid (bottom) of a time series of ASM295 particles with $\phi = 0.559$. The time of each sample is indicated in the top left of each par of distributions.

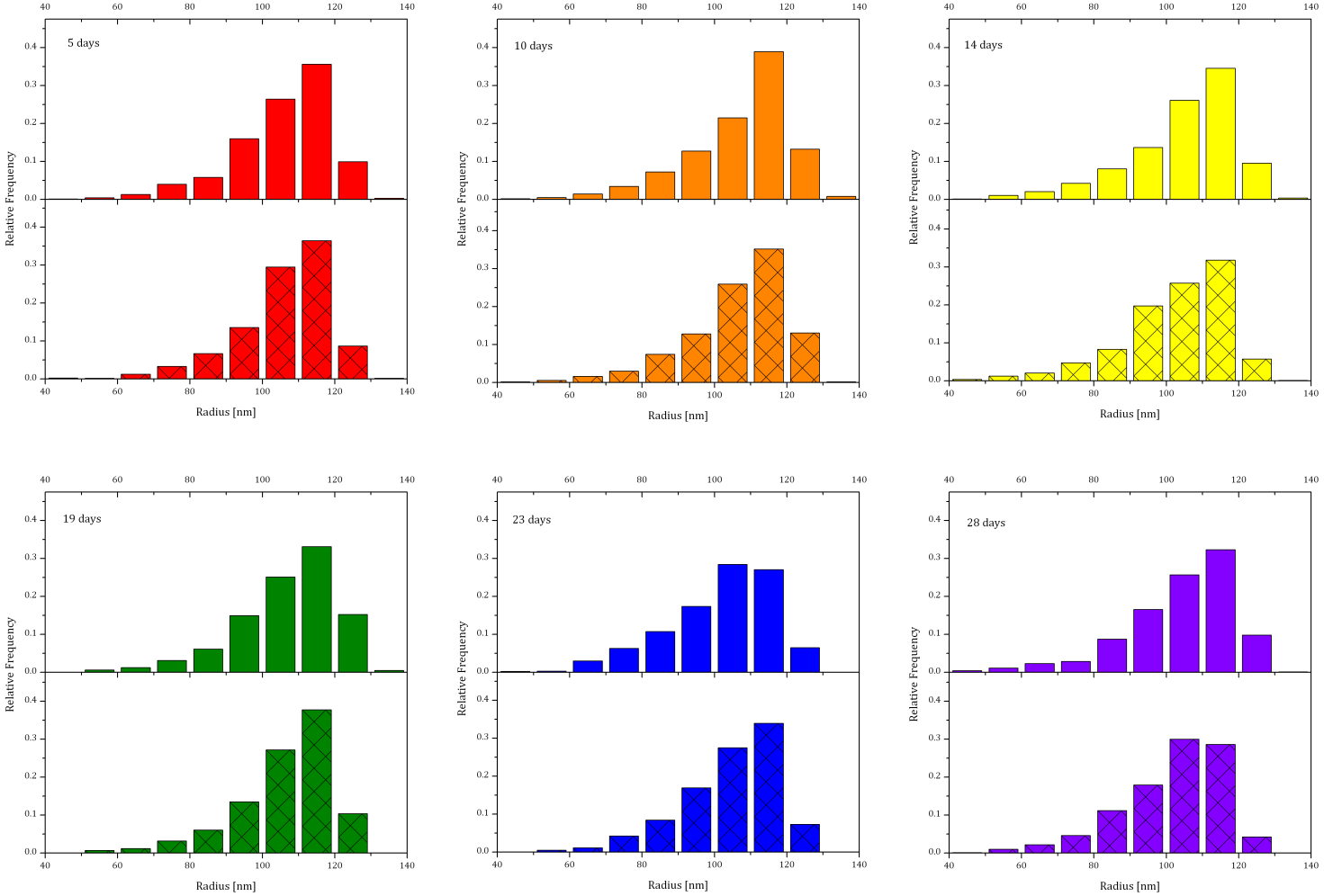

distribution in this case[3]. To make any quantitative comparisons between the different time points, day 5 will be used as a reference, since the average radius and polydispersity of each phase were the same within error.

Within the first 28 days, no statistically significant evidence for size fractionation between coexisting fluid and solid phases was observed. However, there is a systematic decrease of particle size with increasing height in the sample for the 120 day sample: the difference in average radii was 4nm. This is only just outwith the errors of the measurement, but visual observations of different types of crystal nucleation suggest that something is happening.

One possibility is that equilibrium has not yet been reached - crystallisation is certainly not complete within the first 28 days: a graph of the percentage crystal height against time is shown in figure 5.8, with an inset showing the first 28 days only, where the lines are guides to the eye of the slope. The data from the first 28 days suggests fast and slow crystallisation processes are taking place: crystal height increases at a faster rate during the first 12 days than between $12-28$ days. The dashed line in the main graph is an extrapolation of the $12-28$ day slope, coinciding with the percentage height of the upper crystal phase at 120 days.

Using a coarse-grained approach to the results, this suggests the crystals in the upper phase have a nucleation rate similar to those nucleated in the bulk after the first 12 days. Unfortunately we do not have data points for the time between 28 and 120 days, which would be necessary to come to a stronger conclusion. We can however be sure that the system is not yet at equilibrium; the uneven interface between the coexisting fluid and solid phases could be serving as an intermediate phase, exchanging particles between the fluid and solid, as suggested by Sollich and Wilding [109]. One would then expect the observed result of a systematic decrease in particle size with increasing height in the sample.

Another possibility is that the fluid-solid interface is serving as a nucleation point for new crystals. This is supported by the large, heterogeneous crystallites observed in the 120 day sample and other samples (not shown) which initially exhibited fluid-solid coexistence. The question remains whether this is the fluid-solid phase reaching equilibrium, or if the crystallisation seen at times greater than 28 days is the formation of a second, coexisting solid phase.

While the degree of fractionation is not large, the 120 day sample showed

[3]Two more attempts were made to obtain the parent size distribution, but unfortunately neither attempt yielded any useful images.

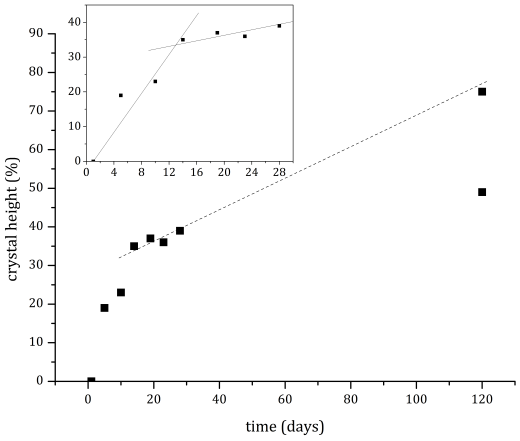

Figure 5.8 Plot of the crystal height versus time for the samples in figure 5.6. The inset shows the first 28 days only, with lines added as guides to the eye of the slope. The dashed line in the main figure is an extrapolation of the $12 - 28$ day slope in the inset.

the systematic change in particle radii between coexisting phases as predicted by Wilding and Sollich. It is likely the 120 day sample has not yet reached equilibrium (and is unlikely to), so the particle transport between phases is incomplete. This, coupled with the coexistence gap discussions of the previous section suggest that the observed phase behaviour with increasing volume fraction of phase behaviour observed for polydispersities $\approx 12\%$ is F$\rightarrow$ F+S $\rightarrow$ F+S+S $\rightarrow$ frustrated fluid $\rightarrow$ glass.

The possibility of fractionation and multiple coexisting solids could be more convincingly concluded in future experiments by utilising scattering techniques to measure changes in the lattice parameters of the crystal over time. A wider distribution of larger particles would enable statistically significant resolution of any size fractionation between coexisting phases, although the use of larger particles will require careful consideration of the effects of gravitational settling on the results.

5.3 Dynamics and arrest

5.3.1 Introduction

In the discussion of phase behaviour in section 5.1, a plot of volume fraction of coexisting phases against parent volume fraction was presented (figure 5.4).

For the example of 8% polydispersity, there would exist samples within the FS coexistence region with experimentally accessible parent volume fractions that would separate into a fluid coexisting with a solid, where the solid volume fraction $\phi_S > 0.58$. In other words, the solid will have volume fractions in the region where we would expect the colloidal glass to be evident.

The conclusion of the previous two sections of this chapter were that the observed coexistence region probably contains both FS and FSS behaviour. While Fasolo and Sollich did not make detailed calculations for the polydispersity of these particles ($\approx 12\%$), if the trend continues with increasing polydispersity we should expect to see an interruption of the coexistence region when a coexisting solid phase has volume fraction above $\phi = 0.58$.

Indeed, we observed a new, non-crystalline phase between the coexistence region and the glass phase, samples $3 - 6$ of figure 5.2, where one would expect to find a single, fully crystalline phase in a monodisperse system. This phase, which we labelled as a *frustrated fluid* (fF), did not exhibit signs of bulk crystallisation but also did not appear to be an arrested, glass phase. The glasses and frustrated fluids were initially categorised by a crude rheology experiment: if the suspension flowed when the vial was tipped, it was labelled a fF, while if the particle-air interface remained stationary with respect to the vial, it was labelled a glass.

This hint at the different dynamics in the frustrated fluid phase was investigated further using dynamic light scattering (DLS). Due to the turbid, concentrated nature of these suspensions, multiple scattering will be dominant in scattering experiments, rendering traditional light scattering ineffective. Instead, the cross-correlation technique of 3d DLS, introduced in chapter 4.3, was used. The remainder of this chapter discusses the techniques and results of the 3d DLS experiments and compares them with simulations on an equivalent system.

5.3.2 Experimental details

Experiments were performed in collaboration with Prof. S. Egelhaaf and Dr. M. Laurati at Heinrich-Heine Universität, Düsseldorf; a photograph of the setup is shown in figure 5.9.

Suspensions of ASM320 particles in decalin spanning the range of phase behaviour were initially prepared. They were were shipped to Düsseldorf in sealed 1.8 ml

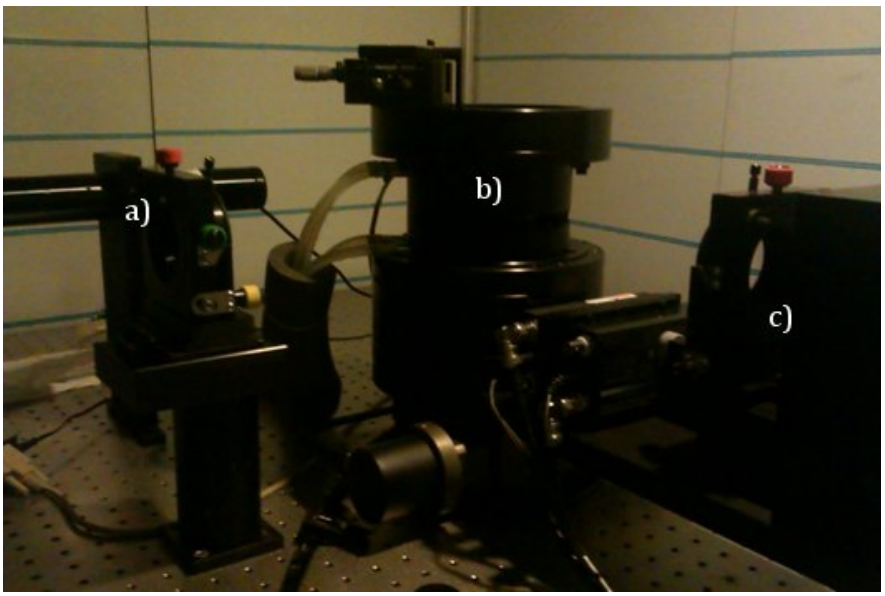

Figure 5.9 Photograph of the 3d DLS setup used. The features marked on the photograph are: a) 628nm laser, directed off to the left of the image, back through a beam splitter and into the sample chamber, b); b) is free to rotate, to allow measurement of different 'speckles' and c) is a CCD camera on a goniometer, which can be rotated to adjust the scattering angle.

vials, then transferred to clean, narrow glass vials suitable for 3d DLS. The vials were then centrifuged briefly (no longer than 3 minutes at 1000 rpm) so any dust or air bubbles present in the particle suspension were displaced from the scattering region. The supply of parent particles was at this point severely depleted, so further samples were prepared in and around the frustrated fluid region by mixing or diluting existing samples and observing the phase behaviour over a few days[4]. As a result, the exact volume fractions of each sample were not easily calculated; the results will be presented using the approximate position of each sample on the ϕ axis relative to the others and the boundaries of the coexistence region.

The vial was placed in the sample chamber, figure 5.9(b), and the incident laser intensity was adjusted such that the maximum average intensity was < 1500kHz to avoid damaging the detector.

The static properties were measured first: the average intensity over 60 seconds was measured for scattering angles between 15 and 135°. The point at which the intensity was maximal was used as the scattering angle for the dynamic light

[4]Although crystallisation is slow, those which do crystallise have observable crystallites in the bulk after 1 or 2 days, so a few days is long enough to decide whether a sample belongs in the coexistence region or the frustrated fluid.

scattering. For the dynamics, the software was programmed to rotate the sample by 10° between each measurement. The number of measurements required to enable proper averaging, and the duration of each measurement is discussed in the next section.

Experimental issues

The time required for each measurement in 3d DLS experiments, to obtain statistically significant results, is 100× the timescale of the decay (to zero) of the normalised, scattered intensity correlation function (ICF), $g^{(2)}(q,\tau) - 1$. Each ICF is itself an average of a series of independent scattering events reaching the detector. The statistics of random, independent events can be described by Poisson statistics and have an error of $1/\sqrt{N}$, where N is the number of events. Here, N is the number of decays, so in an experiment of time t, $N = t/\tau$, where τ is the characteristic decay time of the ICF. So, in order to obtain acceptable statistics (errors no more than 10%) the experiment should run for at least 100τ. For good statistics, errors of at most 1%, we should aim for $t = 10000\tau$.

Additionally, the number of speckles (individual ICFs) required to obtain an accurate picture of the entire system depends on the ergodicity of the system. For fluid-like samples, the system is ergodic and each particle will have, on average, the same dynamics so the normalised ICFs will be identical. In a non-ergodic sample, the dynamics of one particular region will have different behaviour to one elsewhere, or to itself at a later time. This means the dynamics of each speckle will be different, and many speckles need to be measured and averaged to obtain a reliable picture of the whole system.

Furthermore, due to the high volume fractions of the particle suspensions under investigation, there were often aberrations in the dynamics. In particular, some ICF plots had an intercept greater than the theoretical maximum ($\beta_{3dDLS} = 0.25$, discussed in section 4.3.3 on page 72), or so low as to be essentially zero. These measurements, examples of which are shown in figure 5.14a, were discarded. Another peculiarity is that some measurements appeared to have an intensity that increased from the intercept value as time increased, for example in figure 5.14b (page 100). These measurements also had to be discarded. Finally, a quirk of the software meant some measurements appeared reflected in the x-axis (figure 5.14c). These measurements were simply reflected back using a script in Origin. Figure 5.14c also shows oscillations that were present in a few sets of measurements;

they were later discovered to be due to the air conditioning unit in the room.

These issues taken together, meant that the time needed to to perform a sufficient number of measurements for each sample was of the order of days[5]. Since we were interested in the ensemble average of the system, we needed to measure many speckles, which limited the time allowed for each measurement to 1.5 hours. This means that those samples with average decays longer than $\tau = 100s$ will have statistical errors greater than 13%.

5.3.3 Analysis and results

After all datasets, i, were measured and checked, they were processed using scripts in Origin: the bad datasets were removed and the ensemble average was performed using the 'brute force' method (equation 4.38, page 70). The results for a series of samples, with volume fractions spanning fluid to glass behaviours, is shown in figure 5.10.

The dynamics of aged samples were also investigated. All vials were well sealed using teflon tape, parafilm and glue, before placing them in a refrigerator for 3 months to minimise evaporation. After this time, the vials were allowed to come to room temperature before the dynamics measurements were repeated. These aged samples are presented as dashed lines in figure 5.11.

The fluid and those which eventually show coexisting fluid-solid behaviour (on a timescale longer than the measurements) are, in order of volume fraction: the red, blue, grey and purple datasets in figure 5.10. Their dynamic behaviour appears uncontroversially fluid-like: the ICF exhibits a single decay to zero at delay times < 100s, with the decay time increasing with increasing volume fraction.

The samples represented by the blue and purple datasets were also remeasured after 3 months; the data is represented by the dashed lines in figure 5.11. The ageing behaviour is also as expected - the dynamics are slower at longer times.

The frustrated fluid samples, however, are strange in several ways:

- Bumps in the decay
  The "bumps", that is plateaus followed by decays in the ICF, suggest there

[5]All of the analysis and sample preparation was performed by myself. However, my time in Düsseldorf was limited, and the experiments long, so some samples were prepared and left with M. Laurati, who performed those measurements.

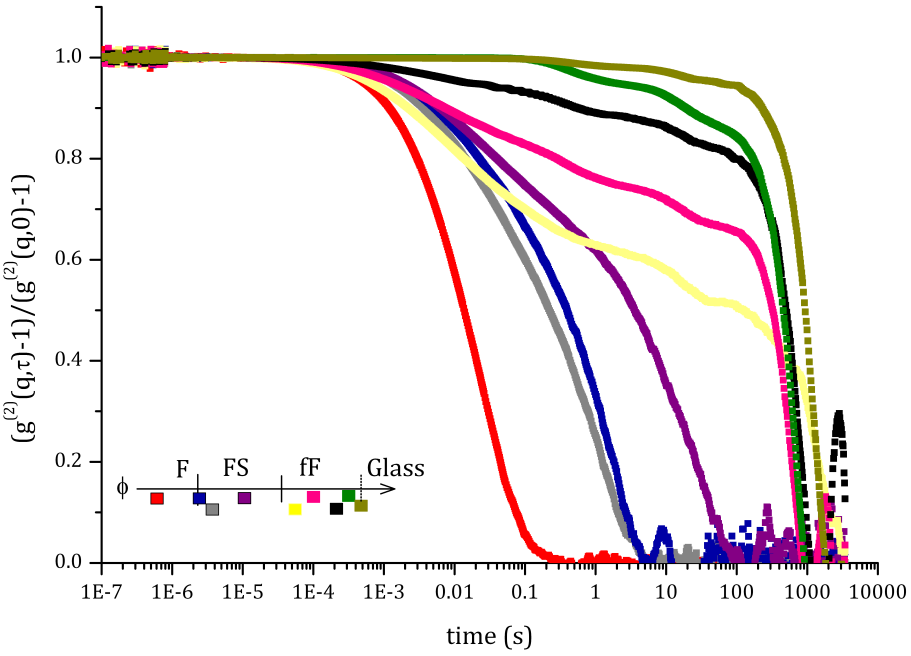

Figure 5.10 3d DLS data for a series of samples of ASM320 particles which shows expected ergodic decays in the fluid and FS samples (red, blue, grey, purple). The 'bumpy' plateaus followed by possible decays to zero signify dynamic heterogeneities in the frustrated fluid samples (yellow, pink, black, green and yellow-green).

are competing arrested (plateaus) and mobile (decays) behaviours within the particle suspension. These were evident in all samples with volume fractions above that of the high-ϕ end of the coexistence region.

The experimental data for one of these bumpy decays was separated into 'fast' or 'slow' behaviours. The category in which each of the 26 datasets (or equivalently, each speckle) belonged was decided arbitrarily by the steepness of the first decay (fast, slow or undecided). The results are plotted in figure 5.12.

Even with such a coarse-grained approach, the results are striking: each speckle appears to be either arrested (blue) or mobile (red) with some speckles with intermediate (purple) dynamics. The average of all behaviours is dominated by the slow dynamics.

- Are the frustrated fluids ergodic?
  There is some ambiguity whether the final decay of the ICF for the

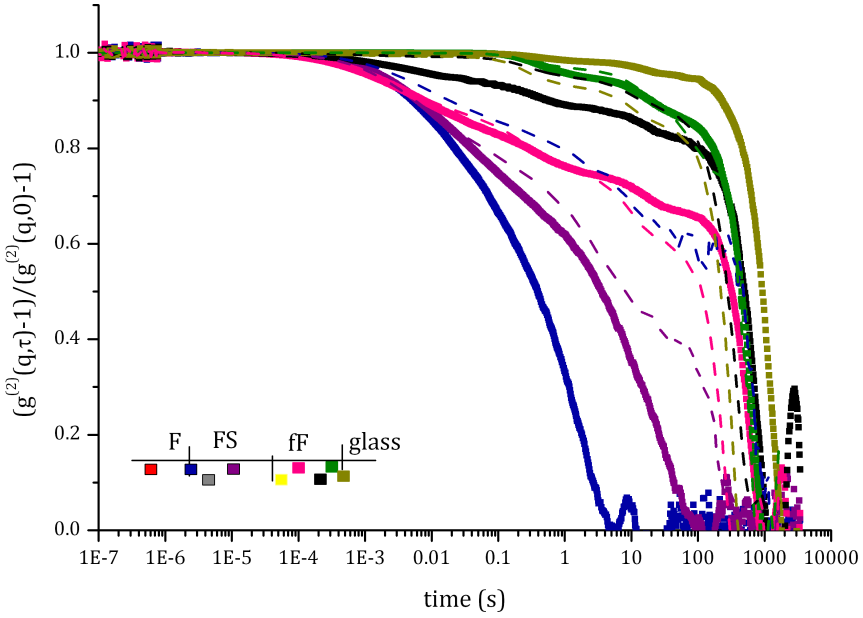

Figure 5.11 The original data from figure 5.10 (points), with the same samples remeasured after 3 months (dashed lines). The pink and yellow-green fF samples show anomalous ageing, while the other datasets all display expected slowing down of dynamics.

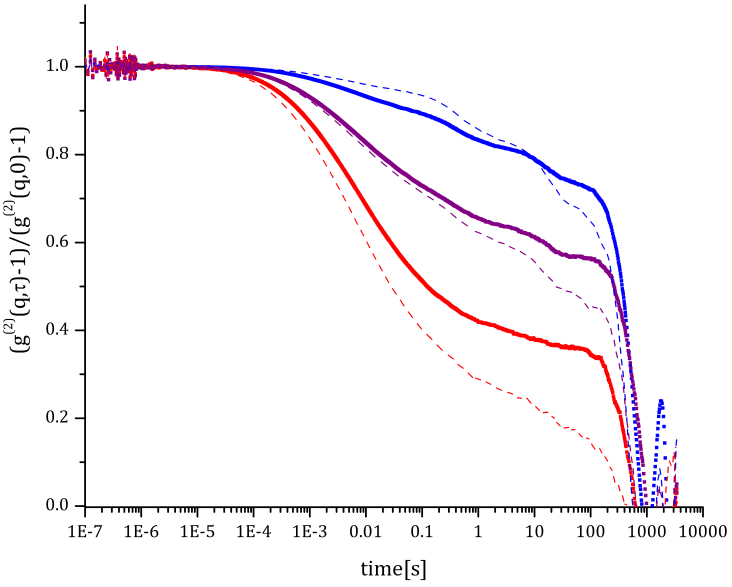

Figure 5.12 Separation of datasets (speckles) into averaged fast (red), slow (blue) and intermediate (purple) behaviours for one of the samples of figure 5.10 within the frustrated fluid region. Each individual ICF was separated by the slope of the initial decay and the average ICF for each category was calculated using equation 4.38.

frustrated fluid (fF) samples is real, hence ambiguity in the ergodicty of these samples. The sharp decays around 1000 s can probably be attributed to the limit of good statistics due to the timescale of the run: as discussed earlier, the statistical error on each ICF is $1/\sqrt{N} = \sqrt{\tau/t}$, so for a 1.5 hour experiment the error is approximately 43% (if $\tau = 1000s$). The yellow sample was measured for a longer time, and appears to slowly decay towards zero, suggesting the frustrated fluids will eventually decay to zero and are thus ergodic.

- Anomalous ageing

  We expect the dynamics of a system of particles to slow as the system ages. The ageing data is presented in figure 5.11: the pink and yellow-green fF samples show anomalous speeding up of the dynamics, while the other datasets all display expected slowing down of dynamics.

  The ageing data is repeatedly inconsistent: of the six averaged ICFs with the highest volume fractions, three exhibited expected slowing down of dynamics (purple, black and blue), one did not show any significant ageing (green) and the remaining two appeared to have faster aged dynamics than their original, corresponding ICF (yellow-green, and pink). Earlier

measurements using same particles (but not all the same samples) were made at a scattering angle of 90°, the peak of the structure factor for the most dilute sample. The results contained five averaged ICFs in the fF region: two of these aged in the expected way, the other three exhibited the anomalous slowing dynamics. This is strong evidence for dynamic heterogeneities within the particle suspension.

5.3.4 Discussion

To better understand the dynamics and ageing in the frustrated fluid samples, Molecular Dynamics simulations of hard spheres with different size distributions, including the exact particle size distribution of ASM320 particles (figure 5.1), were performed by Dr. E. Zaccerelli during her time visiting Edinburgh University. For details of the simulation see ref. [123]. The simulation was set up in close collaboration to ensure the output was directly comparable with the experimental ICFs.

Although data equivalent to the experimental ICFs were produced, it is more illustrative to consider the mean square displacement of each system and from this extract the average self-diffusion coefficient, D, as a measure of the particle dynamics. Furthermore, the distribution was split such that the tails of the distribution, the largest and smallest 10% of particles, were considered separately. The results for the self diffusion constants as a function of volume fraction are displayed in figure 5.13.

Figure 5.13 shows that, as the volume fraction of the system increases, the large particles (triangles) become arrested (glassy) at the expected value of $\phi = 0.58$. On the other hand, the small particles (crosses) remain mobile to much higher volume fractions. The result is the dynamics of the whole system (diamonds) are a whole order of magnitude faster than the large, arrested particles: the movement of the small particles fluidizes the system. This is also in agreement with discussions of the previous section: one of the coexisting phases will have a volume fraction higher than that of the parent and if the volume fraction of that phase is above that of the hard sphere glass transition, slow or arrested behaviour would be observed.

Other distributions were considered; a Gaussian with the same polydispersity as the experimental psd exhibited largely the same behaviour, while a top-hat

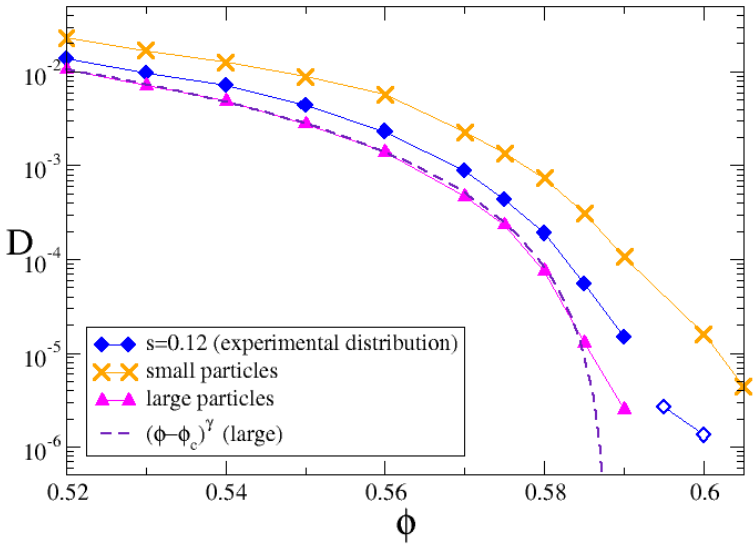

Figure 5.13 Simulations of the diffusion coefficient, D versus volume fraction for particles with the same distribution as the experimental ASM320 particle distribution, showing the large and small particles have dynamics which differ by almost two orders of magnitude. Taken from [123].

distribution did not. Distributions with lower polydispersities also do not show the differing fast and slow dynamics, since the largest and smallest particles do not have such extreme size differences as those in the tails of the 12% distributions. These simulation results suggests that the tails, and hence the shape of the distribution in general, are particularly important in determining the dynamics of polydisperse systems.

The simulations confirm that the strange behaviour observed in the experimental system is in fact due to the polydispersity of the system, rather than some experimental error. The anomalous ageing behaviour still remains unexplained but is an interesting concept; it would be useful to be able to pinpoint the conditions required to consistently achieve speeding up of dynamics in these dense particle systems over time. Tentative analysis of experimental data by splitting the correlation functions of the aged systems (dashed lines in figure 5.12) suggest that the fastest particles speed up over time.

5.4 Summary

In this chapter we have investigated phase behaviour, fractionation and dynamics of polydisperse, hard spheres. Two batches of particles were used, which had polydispersities of 11 and 12%, as determined by transmission electron microscopy. The phase behaviour of these particles was the same in both cases: with increasing volume fraction, fluid $\rightarrow$ fluid-solid coexistence $\rightarrow$ frustrated fluid $\rightarrow$ glass. Comparing the width of the coexistence region to calculations [33], and previous experiments [31], led to the argument that the coexisting fluid-solid region could also contain a fluid-solid-solid phase.

Fractionation of particle sizes between phases is necessary for equilibrium multiple solid behaviour [109], but coexisting fluid and solid phases should also show a difference in average size, with the solid phase containing on average larger particles than the parent and fluid phase [33]. Analysis of transmission electron microscopy images of particles taken from each phase showed no significant fractionation between coexisting fluid and solid phases up to 28 days after peparation.

A fluid-solid sample left for 120 days showed a visual difference in the types of crystallisation of the bottom and top of the solid phase: the crystallites in the lower part of the vial were homogeneously nucleated and appeared similar to those seen at the start of the crystallisation process. The top of the crystal phase appeared to have crystallised by heterogeneous nucleation. There was a clear visual difference in the two types of solid, but there was no sharp interface between the solid phases or the solid and fluid. Electron microscopy analysis of the particles in the three regions of this sample showed a systematic decrease of particle size with vial height. It is unclear whether the top solid phase is a second coexisting solid, or simply the solid phase finally reaching equilibrium, but these observations and measurements coupled with the coexistence gap discussions suggest that fluid+solid+solid behaviour is being observed.

The non-crystallising part of the phase diagram at high volume fractions was more difficult to explain. Dynamic light scattering was used to consider the dynamics of the phase, but cross correlation setup of 3d DLS was necessary due to the turbidity and high concentrations (hence large degree of multiple scattering) of these samples. Analysis of the 3d DLS data showed the samples designated as fF are strange. They exhibit dynamics with both ergodic and non-

ergodic characteristics, due to a combination of fast and slow dynamics within the particle suspensions.

By comparison with simulations using the same experimental distribution, it appears that the small particles remain mobile at high volume fractions, while the large particles are effectively arrested [123]. Interestingly, simulations performed using a top-hat distribution with the same polydispersity did not exhibit the same behaviour. Since top-hat distributions are used in polydisperse simulations in high-profile research [13], full consequences and expected manifestation of behaviour in experimental systems need to be investigated.

The origin of the anomalous ageing behaviour was not fully determined, although initial analysis of the experimental data (separating individual correlation functions into fast and slow types) suggests that the fastest particles become more mobile. Further experimental work and simulations using the protocols developed in this chapter could be extended to elucidate this feature. It is possible that the movements of the small particle facilitate cage-breaking of the larger, arrested particles.

Although, and possibly because, the frustrated fluid is only a small region of the phase space, it has been, until now, not been identified. Due to the popularity of using polydisperse particles to study dynamics of colloidal systems close to the glass transition, it is important to understand more fully the behaviour discovered in this thesis.

Polydispersity clearly has non-trivial effects on the phase behaviour, dynamics and arrest of hard-sphere colloidal systems; in the next chapter, the phase space is extended perpendicularly by adding a short-ranged attraction.

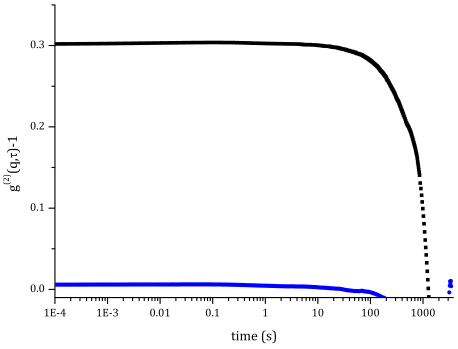

(a) Intercept too high or low.

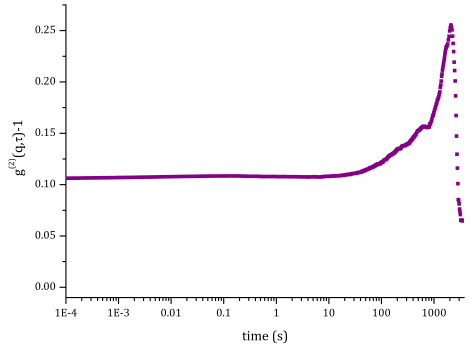

(b) $(g^{(2)} - 1)$ increases from intercept value.

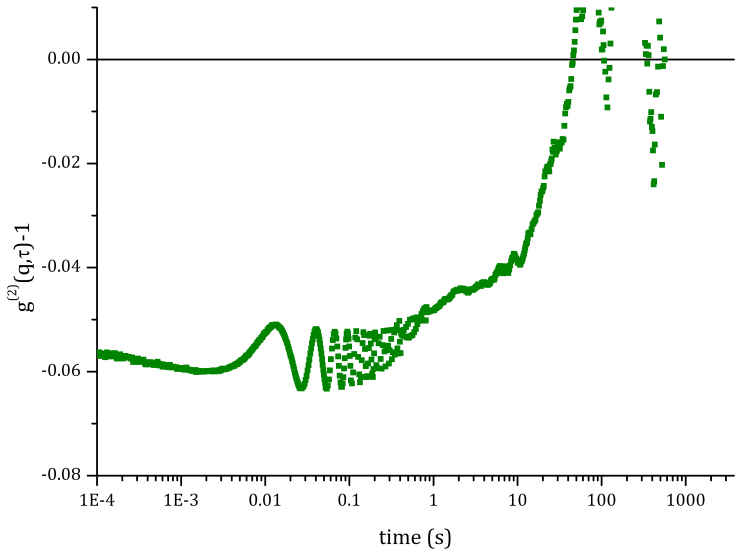

(c) Data is inverted and oscillations are present at short times

Figure 5.14 Issues encountered when performing 3d DLS: (a), the intercept is above the theoretical maximum value, $\beta_{3DDLS} = 0.25$, or too close to zero to be significant; (b), some quirk of the software means occasionally the ICF appears to increase from the intercept; (c) shows inverted data (starts from a negative value) which can simply be reflected in the x-axis, and shows the oscillations at short times that were later revealed to be due to the air conditioning in the room.

Chapter 6

Polydispersity effects in colloid-polymer mixtures

The phase behaviour of colloidal systems become increasingly complex when attraction is added to the system. In the monodisperse limit, when the attraction is short-ranged, increasing attraction broadens the range of equilibrium fluid-solid coexistence. In addition, non-equilibrium features such as a metastable gas-liquid binodal, a gel and an attractive glass are observed. A previous experimental study on a polydisperse system with small polymer revealed the region of fluid-solid coexistence did not spread out [31]. In this section a complete picture of the equilibrium and non-equilibrium features of polydisperse colloidal particles with short-range attraction is presented and discussed.

6.1 Phase boundaries

The hard sphere phase behaviour of an experimental system of Polymethylmethacrylate (PMMA) particles in decalin was presented in chapter 5. The sequence of phases encountered with increasing volume fraction is fluid, fluid-solid coexistence, frustrated fluid and finally a hard sphere colloidal glass at the highest volume fractions. As discussed in the previous chapter, the coexistence region may contain both fluid-solid and fluid-solid-solid behaviours, and the novel behaviour observed in the frustrated fluid region is due to the largest particles in the distribution becoming arrested while the smallest particles are still mobile.

This leads to an overall fluid-like phase with dynamical heterogeneities and anomalous ageing behaviour.

Because the hard-sphere phase behaviour is affected by polydispersity, we could expect that the phase behaviour of an experimental hard-sphere system to be more complex. While theoretical phase behaviour has been predicted [35], experimental determination of the phase behaviour of a short-range attractive, hard-sphere colloidal system has, until now, not been fully explored.

6.1.1 Experimental Setup

The particles used here are the same as those used in chapter 5.3 for the dynamics experiments: PMMA particles with mean core (TEM) radius of 124 ± 4 nm and polydispersity of 12%, suspended in a mixture of cis- and trans- decahydronaphthalene (decalin). A short-range attraction was added to the system by the addition of a polymer depletant. The size ratio of the polymer radius of gyration to average colloidal radius, $\xi = r_g/\overline{R}$ dictates the regime of phase behaviour (see chapter 2.3.1 for further discussion). The depletant chosen for this system had a size ratio well within the regime of short-range attraction, $\xi < 0.2$.

The polymer used was polystyrene, which had molecular weight of $114,200$ Daltons and an unknown polydispersity. Using the Flory calculations (page 50), the radius of gyration at 298 K is 10 nm and $\xi = \frac{10}{124} = 0.08(1)$[1].

Samples were prepared with a range of volume fractions, ϕ and polymer concentrations, c_p. A parent batch of particles was prepared, where the volume fraction was calculated by centrifuging the parent vial and measuring the fractional height of the random-close-packed sediment, $\phi \approx 0.64f$. The majority of the samples were prepared from the same parent batch as those used in the hard-sphere phase behaviour experiments of chapter 5; the volume fractions were scaled using the same factor as those in table 5.1, such that the hard-sphere vial with the highest proportion of crystal phase had volume fraction of 0.58.

1ml samples of the parent colloid suspension were pipetted into 1.8ml cylindrical

[1]This was calculated using the TEM value of the average radius, although *in situ*, the particles will swell. However, swelling of the colloids means ξ will decrease and since the attraction should already be short-ranged, a small decrease in size ratio should not have any qualitative effect on the observed phase behaviour.

cuvettes then decalin was either added dropwise, or removed by centrifugation then extracting a measured mass of solvent. The volume fraction of each sample, relative to the parent volume fraction, is calculated using the lever rule, $\phi_1 V_1 = \phi_2 V_2$.

A known mass of solid polymer was then added to the prepared colloidal suspensions. The concentration was calculated simply by $c_p = m_{polymer}/V$ where V is the total volume of colloids plus solvent in the vial. The vials were left to mix on a rollerbank mixer overnight. The most concentrated samples, or those that had been in the centrifuge were also mixed vigorously on a whirlmixer to effectively re-disperse the particles before placing on the rollerbank. The vials were checked visually after mixing to ensure no large masses of polymer were still present.

When all samples in the series were well-mixed, the vials were placed in an incubator set to 25°C for up to two weeks. This was sufficient time for any suspensions to start crystallising and hence categorise. Subsequent samples for each data point were prepared by adding two drops of decalin and re-dispersing the suspension. This increases the volume and hence decreases the colloid volume fraction and the polymer concentration, producing the "dilution lines" shown in figure 6.1. To prepare a series of suspensions with increasing particle and polymer concentrations, the suspension is centrifuged, then a pasteur pipette is used to extract a small amount of decalin. Two drops are then discarded and the remaining decalin in the pipette is added back to the sample. The latter technique is best used for hard-sphere mixtures only, due to the uncertainty of the concentration of polymer in the solvent and spun-down particles of centrifuged, colloid-polymer mixtures.

The dropwise dilution method is the most efficient way to sample a large area of the phase diagram quickly[2]. The mass of the vials were measured, so although two drops did not always have the same mass, the relative volume fractions could be easily calculated. Preparing a dilution series is more efficient than a concentration series, due to the long centrifugation times needed to obtain a sediment of these small, polydisperse particles. Diluting the samples does of course destroy the original, so long-time observations cannot be made, but it means the relative positions of phase boundaries should be accurate: the points in phase space of

[2]Note that preparing large numbers of small vials can lead to incidents of frustration if one (or more, domino style) is accidentally knocked over. I strongly recommend using a vial holder to keep the vials upright.

each sample on a dilution line, relative to each other, can be calculated with both accuracy and precision.

6.1.2 Observations and Results

A large number of samples were prepared and recorded, but only the minimal set required to delineate all of the observed states in the phase diagram have been plotted in figure 6.1. The lines are all guides to the eye of the phase boundaries, with the exception of the red dotted line, which is a schematic of the attractive glass line.

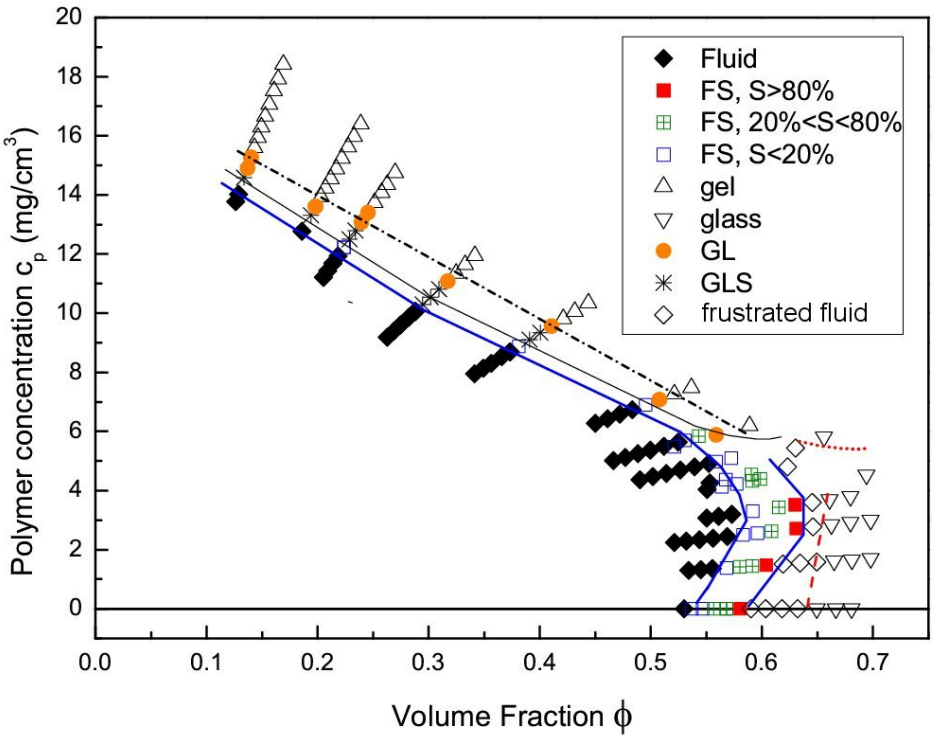

Figure 6.1 Observed phase diagram, with legend given in the inset, where G, L and S stand for gas, liquid and solid (crystal) phases. Three kinds of fluid-solid coexistence samples are distinguished, in terms of their fraction of solid phase: S $< 20\%$, S $> 80\%$ and $20\% <$ S $< 80\%$. Lines are guides to the eye of where various phase boundaries lie as deduced from the data points; the exception is the dotted line, which is a schematic of the attractive glass line.

Firstly, on the no-polymer, horizontal axis, we observed the hard-sphere phase behaviour documented in chapter 5: as the volume fraction of the particles was increased, the suspensions transition from a single phase fluid ($\diamond$) at volume fractions below $\phi \approx 0.55$ to a fluid coexisting with a solid (FS) denoted by

squares in figure 6.1. Small solid crystallites nucleated in the bulk of the sample and settled to the bottom of the vial. The percentage of crystals in the vial was measured after two weeks, using a vernier rule. Each percentage is indicated by the different square symbols: □, ⊞ and ■, where the different fillings denote increasing percentage of crystals: below 20%, between 20 and 80% and above 80% respectively. The conclusions of chapter 5 indicate that crystal phase is unlikely to have reached equilibrium after only two weeks, and that this coexistence region may also contain samples which would eventually contain a fluid coexisting with two solid (crystal) phases.

Increasing ϕ further, the frustrated fluid phase (fF) is encountered. This phase is likely to be formed due to different volume fractions between coexisting phases. In moderately polydisperse systems, there is no single phase at volume fractions above the fluid-solid coexistence region. Any phase separation will lead to different phases having different volume fractions; this volume fraction could be high enough ($\phi > 0.58$) that one or more of the phases are arrested. Indeed, this is what we observe from the dynamic light scattering experiments and comparison with simulations (chapter 5.3): the largest particles are arrested while the smallest particles remain mobile.

At volume fractions high enough, $\phi > 0.64$, the suspension was unambiguously fully arrested: the particle-air interface did not move when the vial was tilted[3].

Next, we consider the phase behaviour when attraction is added. For low polymer concentrations, $c_p < 6\text{mg/cm}^3$ the region of fluid-solid coexistence remains approximately the same width. This region also has a re-entrant shape: following a vertical line at $\phi \approx 0.55$, without polymer there is crystallisation; increasing to $c_p = 4\text{mg/cm}^3$ the crystal melts back into a single-phase fluid; increasing the polymer concentration futher, above $\approx 6\text{mg/cm}^3$, we again observe crystallisation. There is also similar re-entrant behaviour at the high-ϕ boundary of the coexistence region.

Increasing the concentration of polymer past 6mg/cm^3, for volume fractions below 0.55, results in the samples entering the metastable binodal region of the phase diagram. Within the binodal the suspension undergoes phase separation into two fluid phases with different turbidities and a sharp interface. These samples were labelled gas-liquid. In the samples closest to the binodal, crystallites appeared in the bottom, fluid phase and sedimented out, eventually forming a significant

[3]Or accidentally dropped.

crystal layer; sometimes as much as 1/3 of the total height of the suspension. This large proportion of crystalline particles suggests that there was actually bulk crystallisation, rather than the possibility of crystals forming on the wall of the vial. The gas phase persisted in these cases and the liquid did not become consumed completely by the crystal phase. These samples were thus classified as having three-phase, gas-liquid-solid (GLS) behaviour, denoted in figure 6.1 by $*$.

As the concentration of polymer is increased within the binodal region, the coexisting gas-liquid samples no longer crystallise. The onset of GL formation started within a few hours, but no crystallites were seen in the liquid phase after two weeks. These two-phase, gas-liquid (GL) samples are denoted by • in figure 6.1.

At the highest polymer concentrations (relative to the binodal), a colloidal gel was observed. Usually, the difference between gel and GL behaviours was obvious: in gel samples, a particle-fluid interface was formed at the top of the suspension and this interface quickly collapsed such that all of the particles were contained in a single, percolated phase with a solvent layer above. This type of transient gelation was not the focus of these experiments, but recordings were made of the gel collapse such that the height of the interface over time could be measured. The interfaces had a timescale of collapse typical of gels in short-range attractive, colloid-polymer systems [112].

Some of the samples had gel phases which, for some reason, did not contain all of the particles. These looked visually similar to some GL samples which, due to the steep binodal, had a gas phase with very low volume fraction. In these situations, it was difficult to categorise GL and gel samples by turbidity alone; gels were distinguished from GL behaviour by the "tip-test": the gel interface remained parallel to the vial bottom, but the liquid interface became horizontal. A photograph of a tip-test comparison can be seen in figure 6.2.

6.1.3 Discussion

Fluid-solid coexistence region

The experimental results are interpreted in light of theoretical phase diagram topologies published by Fasolo and Sollich [35], who used mean free energy calculations to consider the phase behaviour of systems with various polydispersites, σ

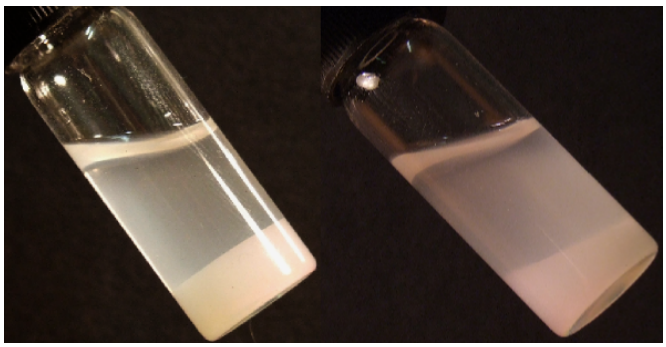

Figure 6.2 The "tip-test": photograph comparing a typical gel (left), which has an interface parallel to the vial bottom, and a gas-liquid sample (right), with interface is parallel to the meniscus.

and attraction ranges, ξ. Reproduced in figure 6.3 are their predicted equilibrium phase topologies for low ξ and three values of polydispersity: $\sigma = 5$, 7 and 8%. A dotted line indicating the metastable binodal has been drawn on in each case.

The $\sigma < 5\%$ schematic shows that, in systems with low polydispersity, the expected topology coincides with that observed in experiments using "effectively monodisperse" colloids [52]: the region of fluid-solid coexistence broadens with increasing c_p, and various non-equilibrium behaviours are observed at high c_p that are interpreted as the presence of a metastable gas-liquid binodal buried within the FS coexistence region. The effectively monodisperse, experimental topology is sketched in the inset of figure 6.3; the phase boundaries that exist in both the experimental topology and the calculated equilibrium case are that of the FS coexistence region (blue lines), the single-phase solid and the metastable binodal. Any predicted multiple solid (SS) or FSS regions are in experimentally inaccessible regions of the phase diagram - the volume fraction of these phases will be > 0.58 so the colloidal glass transition will intervene before phase separation can progress.

When the polydispersity of the colloids is higher than 5%, the multiple solid regions discussed in chapter 5, that are on the horizontal axis of the (ϕ, c_p) phase diagram, extend in the vertical direction. The region of phase behaviour which broadens with increasing polymer concentration shifts sequentially to higher volume fractions as polydispersity is increased. When $\sigma < 5\%$, the largest region of phase behaviour is FS; increasing polydispersity to 7%, the largest region is now the FSS phase; finally, when $\sigma = 8\%$, the FS and FSS regions remain constant width and the FSSS region broadens. Experimentally realisable volume fractions lie within the FS or FSS regions, so it is somewhat irrelevant whether our

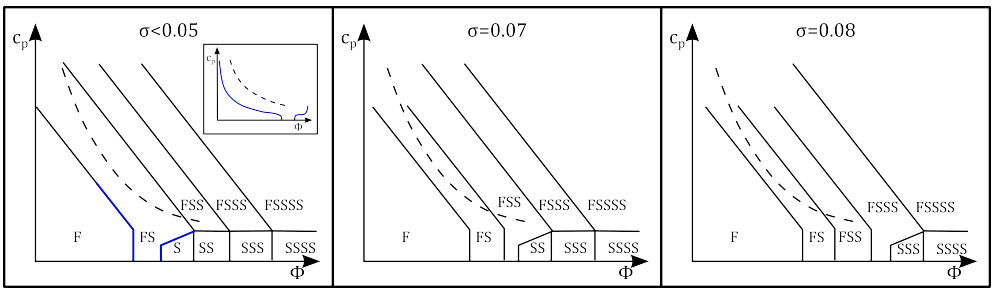

Figure 6.3 Topology of the phase diagram of a polydisperse colloid-polymer mixture with polydispersities (left to right) $\sigma < 5\%$, $\sigma = 7\%$ and $\sigma = 8\%$ according to [35]. Inset: a schematic representation of the phase diagram for a monodisperse colloid plus polymer mixture, with blue lines indicating observed experimental phase boundaries. In each case the metastable binodal has also been drawn in.

experimental topology is in line with the predictions for "7%", "8%", or indeed a higher polydispersity, because any broadening will occur at volume fractions too high to be observed.

The experimental FS coexistence region delineated in figure 6.1 for these $\sigma = 12\%$ particles follows the same quantitative shape predicted in figure 6.3 for $\sigma > 5\%$: the boundaries of the FS coexistence region remain parallel with increasing polymer concentration, although the calculations of reference [35] do not predict the experimentally observed re-entrant shape.

Metastable binodal region

For polydisperse colloid-polymer mixtures, the binodal should be buried within multiple regions of the phase diagram according to figure 6.3, intersecting with the FS/FSS boundary, so we may expect more than one type of behaviour within the binodal region.

One complication is that, as discussed in chapter 5.1, it is possible the experimental coexistence region contains both FS and FSS behaviour and, at volume fractions above the coexistence region the non-equilibrium frustrated fluid is present. Thus we attribute the multiple types of behaviour within the binodal region in figure 6.1 to be caused by the intersection of the coexistence/fF boundary with the binodal: the samples with parent volume fractions closest to the binodal exhibit three-phase, GLS behaviour, consistent with this region being below the coexistence/fF boundary within the binodal.

Polydispersity of the particles is likely to decrease the gap in free energy between the gas-liquid curve and the solid curve, since polydispersity will increase the free energy minimum of the solid curve proportionally more than it will change the gas-liquid curve. This means the fluctuations in free energy required for the system to escape from metastable GL coexistence to equilibrium gas-solid coexistence will be smaller than in a monodisperse, metastable system. It remains to be seen whether this is an equilibrium phase (where all three minima lie on one common tangent in the free energy diagram) or if the equilibrium is gas-solid and the slow crystallisation of the higher volume fraction phase results in the existence of a non-equilibrium gas-liquid-solid.

At higher polymer concentrations relative to the binodal, a two phase region is observed. This region lies between the FS/fF boundary and the fF/gel boundary within the binodal and was originally labelled as a coexisting gas-liquid. The "liquid" phase of samples within this region is likely to have a volume fraction within the frustrated fluid region, so should instead be labelled gas-frustrated fluid. This could be confirmed by performing dynamic light scattering on the dense phase of the coexisting sample - a frustrated fluid can be easily be identified from the dynamical heterogeneities which manifest as a series of plateaus and decays in the intensity correlation function of a DLS experiment (section 5.3).

Finally at high polymer concentrations relative to the binodal, the observed phase is a gel phase, analogous to that seen in monodisperse systems with short-ranged attraction [112]. This phase is situated above a tie-line that intersects the binodal approximately where the attractive glass line would also intersect from the other side. A revised schematic of the experimental phase diagram with potential bounary intersections are shown in figure 6.4.

Conclusions

No widening of the fluid-solid coexistence region in this system of moderately polydisperse colloids and small polymer was observed, in agreement with previous experimental work [31]. The phase diagram was extended to a wider range of colloid volume fractions and polymer concentrations than has been investigated previously, revealing the full phase behaviour.

The experimental observations were considered in light of calculated equilibrium phase behaviour of Fasolo and Sollich [35]; as a result, the phase topology for

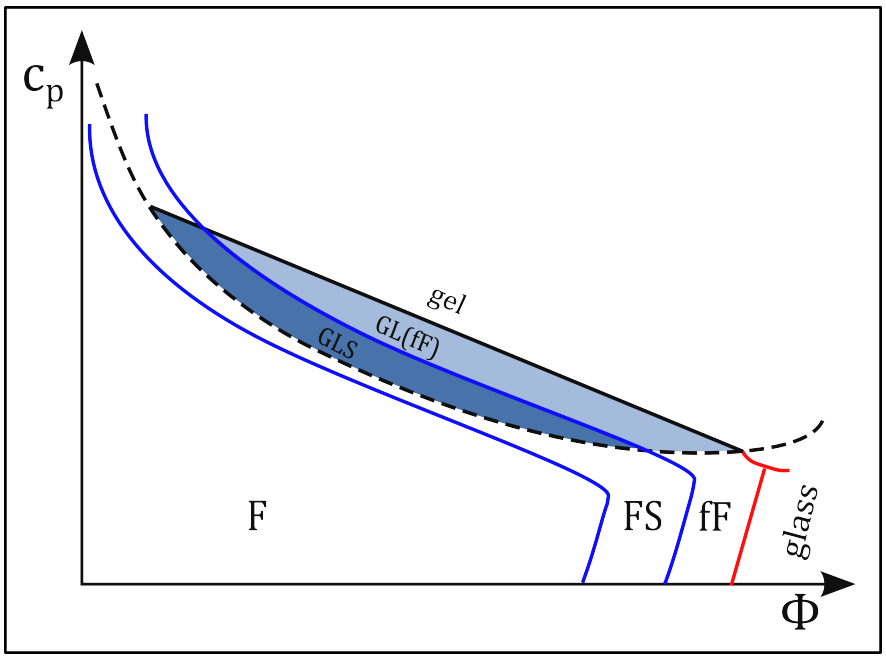

Figure 6.4 Schematic of the experimental phase behaviour of a colloid-polymer mixture with low attraction range, ξ, and moderate polydispersity, $\sigma \geq 7\%$, showing intersection of equilibrium and non-equilibrium phase behaviour. The coexistence region is labelled FS although it is possible it contains both fluid-solid and fluid-solid-solid behaviour within the region, the dashed line denotes the metastable binodal and the region labelled *fF* is the non-crystallising frustrated fluid investigated in chapter 5.3.

a general colloid-polymer mixture, with moderate colloid polydispersity and a short range attraction was determined and is presented in figure 6.4.

The intersection of phase boundaries with the metastable binodal leads to novel phase topology not present in colloid-polymer mixtures when the colloid is monodisperse. These non-equilibrium features within the binodal, coexisting GLS and GL(fF), will be discussed further in the next section.

6.2 Phase transition kinetics

Determination of the binodal

When the relative volumes of two coexisting phases are known, the lever rule provides a method of estimating the volume fractions of each phase and thus an estimate of the position of the binodal [11]. The heights of each of the gas-

liquid and gas-liquid-solid samples in figure 6.1 were carefully measured using an upright vernier rule. The proportion of heights of the samples is related to the proportion of volume fractions of each coexisting phase, relative to the parent volume fraction; this information was used with the lever rule (page 2.3.2) to check the 'guide to the eye' binodal line drawn in the figure was reasonable.

Currently there are no calculations of binodals in an equivalent system to compare with these experimental observations. However, Warren studied the (GL) phase transition kinetics of Schulz-distributed particles in 1999 [117]. Much like Bartlett's discussion of the hard-sphere freezing case [5], he proposed two competing types of kinetics, depending on whether the system was quenched (fast) or annealed (slow). The kinetics of the system were then split into two stages: a fast spinodal stage and a slow ripening stage. Competition of the quenched and annealed behaviours was predicted to introduce more complex phase behaviour.

With this in mind, it is possible that the samples with parent ϕ and c_p close to the edge of the binodal have reached the annealed, ripening stage of kinetics. This would account for the two-staged crystallisation kinetics observed, since we know from chapter 5 that crystallisation in this system is slow: crystallites start to appear in FS coexistence after 1 day but the sample does not reach equilibrium within the first 28 days.

Those samples deeper into the binodal, which do not crystallise, must therefore have not reached the ripening stage. This is in agreement with our theory that the high-ϕ phase in the coexisting "gas-liquid" samples is actually a partially arrested frustrated fluid. The fast, quenching process allows the sample to phase separate, but since the phase with the higher volume fraction is partially arrested, the slow, ripening process cannot take place.

In chapter 5.2 we discussed possible fractionation between coexisting fluid and solid phases in a hard-sphere system with similar polydispersity ($\phi = 11\%$); we concluded the crystallisation process is very slow, and any possible fractionation between multiple solid phases would require a coexisting fluid phase to help transport the particles. It is possible that the different phase separation kinetics of samples within the metastable binodal region could facilitate fractionation of particle size between phases. Fractionation of particle sizes between coexisting phases within the binodal region of figure 6.1 is investigated in the following section.

6.3 Fractionation within the metastable binodal

The presence of two types of non-arrested phase behaviour within the binodal is one of the novel features of this polydisperse colloid-polymer system, so it is important to investigate them further. While no significant fractionation was observed in coexisting fluid-solid phases of the hard-sphere system, it is possible that the kinetics of the samples within the binodal region could facilitate size fractionation in coexisting GL or GLS phases. The possibility of particle size fractionation was investigated using both scattering techniques and electron microscopy.

6.3.1 Experimental setup

Batch C of ASM320 particles ($\sigma = 12\%$) was used for these experiments. The volume fraction of the parent suspension was determined using the centrifugation method. Approximately half of the suspension was transferred to another vial and solvent was added such that the new volume fraction was approximately 0.2. 3 ml of the $\phi \approx 0.2$ suspension was then transferred into two smaller vials. At this point, solid polymer was added with reference to figure 6.1 to achieve (ϕ, c_p) points expected to be in either the GL(fF) or GLS region.

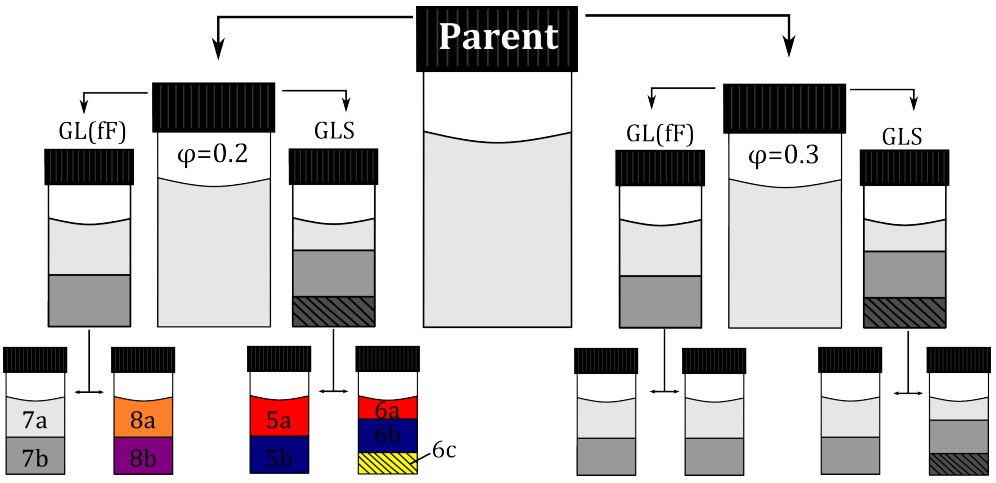

Figure 6.5 Illustration of the samples prepared to investigate possible fractionation between coexisting gas-frustrated fluid, GL(fF), and gas-liquid-solid, GLS, phases, as described in the text. Two vials were prepared for each type of behaviour so the short and long time characteristics could be measured.

The colloid-polymer suspensions were well-mixed on a rollerbank overnight then

left undisturbed in an incubator set at 298 K so the phase behaviour could be observed. When both GL(fF) and GLS behaviours had been observed, each vial was mixed again on the rollerbank and two identical 1.8 ml vials, each containing 1 ml of particles was prepared. This procedure was repeated to obtain an equivalent set of samples at $\phi \approx 0.3$; the resultant samples are summarised in figure 6.5.

Initial gas-liquid separation is fast for samples with both types of behaviour - an interface is observed within an hour. A small amount of the gas phase was extracted and diluted in decalin, then the remainder of the gas phase, plus some interface region was removed and discarded. A small amount of the liquid phase was then extracted and diluted in decalin. The second vial for each point was left undisturbed for several days to allow for any crystallisation, then each of the phases were extracted in the same top-down manner as those at earlier times. The size and polydispersity of the particles in each phase were then determined through a combination of small-angle x-ray scattering and transmission electron microscopy.

6.3.2 Characterising coexisting phases

For the $\phi \approx 0.3$ samples, only small-angle x-ray scattering (SAXS) was used to characterise the particles. The size and polydispersity were determined by assuming a Schulz distribution and fitting calculated form factors to the experimental ones, as discussed below.

Transmission electron microscopy (TEM) was also used to measure directly the distribution of the particles of the phases with parent volume fraction $\phi \approx 0.2$. Additionally, the TEM distribution was used to calculate a form factor. By comparing this with the SAXS form factors, the average radius and polydispersity, as well as an estimate of the particle swelling and hair thickness was determined. The difficulties in reconciling TEM and SAXS data were introduced in chapter 4 and are discussed further later in this section (page 119).

SAXS

Characterisation of particle suspensions using scattering methods was discussed in chapter 4.2.1. A quick method of determining the average radius of the particles

is by considering the **q**-value of the first minimum, where **q** is the scattering vector, defined in equation 4.7 (page 52). For monodisperse particles, the first minimum ($I \to 0$) occurs at a value of $qR = 4.493$, where R is the radius of the particles. A suspension containing particles of multiple sizes leads to multiple points where $I \to 0$, which results in minima with non-zero intensity.

The polydispersity of the suspension can be determined from the ratio of heights of the first minimum and second maximum: the more pronounced the difference, the lower the polydispersity. Experimental form factors for each of the phases with parent volume fraction 0.2 are presented in figure 6.6. The intensity is in arbitrary units and, in the case of the three-phase samples, the intensity was scaled in order to distinguish the curves. The background scattering from the solvent was measured and subtracted from each measurement. Using the information about the relative intensities of the first minimum and second maximum we can see that the sample which ends up as a coexisting gas-frustrated fluid (bottom left in figure 6.6) has the greatest difference in the size and polydispersities of each phase, while the sample that eventually exhibits three-phase gas-liquid-solid (top and bottom right) has form factors that are visibly similar.

Table 6.1 Average core radius ($\overline{R}_{SAXS}$) and polydispersity (σ_{SAXS}) as measured by a core-shell particle model with a Schulz fit to the scattering data. All radii have error $\overline{R}_{SAXS} \pm 2$ nm, and polydispersities are $\sigma_{SAXS} \pm 0.2\%$. The two rows that are in grey were the the intermediate gas and liquid phases, extracted after a few hours of preparation. fF is used to signify that we expect the most dense fluid phase in the two-phase sample to be a frustrated fluid.

	$\phi = 0.2$	$\phi = 0.2$	$\phi = 0.3$	$\phi = 0.3$
Phase(behaviour)	$\overline{R}_{SAXS}/nm$	$\sigma_{SAXS}/\%$	$\overline{R}_{SAXS}$ σ_{SAXS}/nm	$\sigma_{SAXS}/\%$
Parent	152	6.1	152	6.1
Gas [GL(fF)]	139	13.0	142	10.5
Liquid [GL(fF)]	152	6.8	153	6.7
Gas (GLS)	152	7.7	148	8.5
Liquid (GLS)	153	7.5	153	6.4
Gas (GLS)	152	7.8	145	10.3
Liquid (GLS)	153	7.3	150	7.9
Solid (GLS)	155	7	153	6.2

The parent and 30% particles were prepared and sent to T. Narayanan at the European Synchrotron Radiation Facicilty (ESRF) in Grenoble, France to perform the SAXS; I travelled to the ESRF to perform the experiments on the subsequent 20% batch. Dilute suspensions of each phase were transported

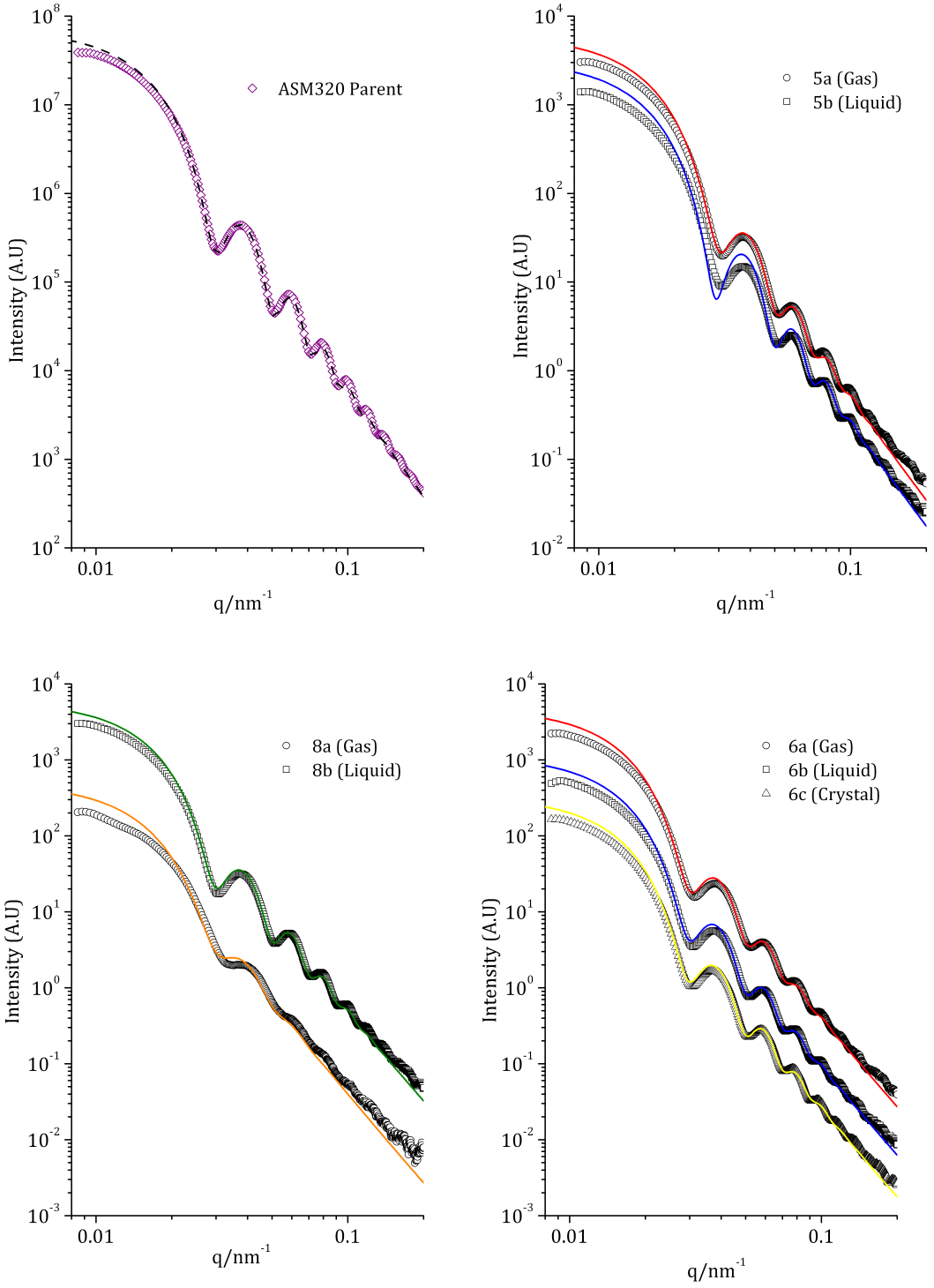

Figure 6.6 Background-subtracted, small-angle x-ray scattering data (points) and Schulz fits (lines) for ASM320 particles with parent volume fraction $\phi \approx 0.2$. Top left: parent particles, measured and fit by T. Narayanan at ESRF. Bottom left: fit to the gas-frustrated fluid phases of the sample. The different size and polydispersity of these phases can be easily distinguished in this figure. The right-hand column contains the intermediate gas-liquid (top) and final coexisting gas-liquid-solid phases (bottom) of the GLS sample; the form factors are near identical in each phase and the absolute intensity had to be scaled in order for the curves to be distinguishable.

in 1.8 ml vials to the ID02 beamline at ESRF. When there, each particle suspension was transferred to a flow-through capilliary of diameter 1.8 mm. The geometry of the experimental equipment is designed such that, by varying the sample-to-detector distance from 1 to 10 m, a scattering vector range of $0.008\ \mathrm{nm}^{-1} \leq q \leq 3\ \mathrm{nm}^{-1}$ could be covered. Measured two-dimensional scattering patterns were normalized to an absolute intensity scale and then azimuthally averaged to obtain the intensity as a function of q, $I(q)$ [24].

All form factor fitting was performed using a form-factor generating script (provided by T. Narayanan) in Origin, assuming a Schulz distribution. All fits were convolved with a instrument resolution smearing function, which smears the form factor in the low-**q** region. The original parent particles were fitted to have a shell radius of 8 ± 2 nm, so this was used as the shell thickness in each of the other fits.

The error in the fit was determined by the resolution of the fits: the average radius was distinguishable to $\pm$2nm and the polydispersity was changed in steps of 0.2%. The best fit parameters of a Schulz-distributed core-shell particle model are presented in table 6.1.

The results of the form factor fitting confirm the visual conclusions from considering the shape of the form factors in figure 6.6: the coexisting phases of the GL sample are significantly fractionated. The gas contains smaller, more polydisperse particles than the liquid. A similar trend is seen in the size and polyispersities of the coexisting GLS particles. Although the extent of the fractionation is small, the gas phase in both sets of data contains the smallest, most polydisperse particles, while the solid phase has the largest, least polydisperse particles.

Since the particles were likely not to have a Schulz distribution (since the parent particle size distribution has a negatively skewed, Weibull shape, fig 5.1), this may affect the fits to the SAXS. Indeed, it is likely to be the reason some of the fits in figure 6.6 were not good. For this reason, the exact particle size distributions of each coexisting phase was also determined using TEM.

TEM

Transmission electron microscopy was used to extract size distributions for all phases of the samples with parent volume fraction $\phi \approx 0.2$. The imaging and

processing technique is identical to that used for the fractionating hard sphere samples (chapter 5.2); the resultant distributions for each phase are shown as histograms in figure 6.7.

The first thing to note is that the distributions do not follow a Schulz shape - they are negatively skewed in all cases, with a tail of small particles. Secondly, the solid phase is not significantly less polydisperse than the parent phase, although in all cases the most concentrated phase appears to contain more of the larger particles. This echoes the results of the fractionation in coexisting fluid-solid samples in hard-sphere systems: no significant fractionation of particle size between coexisting phases was observed.

The coexisting gas-liquid samples did, however, have a notable difference in both size and polydispersity between the two phases. The average size and polydispersity as determined from these distributions are recorded in table 6.2. The dominant source of error in the measurements is the standard error of the mean, which scales inversely as the square root number of particles counted.

Table 6.2 Average radius ($\overline{R}$) and polydispersity (σ) determined by measuring the Feret diameters of particles in ImageJ from transmission electron microscope images. fF is used to signify that we expect the most dense fluid phase in the two-phase sample to be a frustrated fluid.

Phase [behaviour]	$\phi = 0.2$ $\overline{R}_{TEM}/nm$	$\phi = 0.2$ $\sigma_{TEM}/\%$	N
Parent	124(4)	12.2(4)	2201
Gas [GL(fF)]	120(4)	14.7(5)	1029
Liquid[GL(fF)]	132(5)	8.5(3)	1163
Gas (GLS)	131 (5)	7.6(3)	1104
Liquid (GLS)	124(5)	12.3(5)	1014
Gas (GLS)	125(4)	11.2(4)	1149
Liquid (GLS)	131(5)	9.7(4)	1057
Solid (GLS)	135(5)	8.3(3)	1076

Distributions obtained from transmission electron microscopy analysis have the advantage of allowing comparison between distributions from different phases without employing any fitting techniques. However, the TEM radius will always be smaller than that of the scattering measurements, due to the drying of the particles during preparation, then the exposure of the sample to the vacuum within the TEM. Consequently the polydispersity will be larger than that of the same particles in solvent and it is possible that (de)swelling is size dependent. Therefore, to consolidate the results and obtain a good estimate of the size and polydispersity of the particles, these factors must be taken into account. We wish

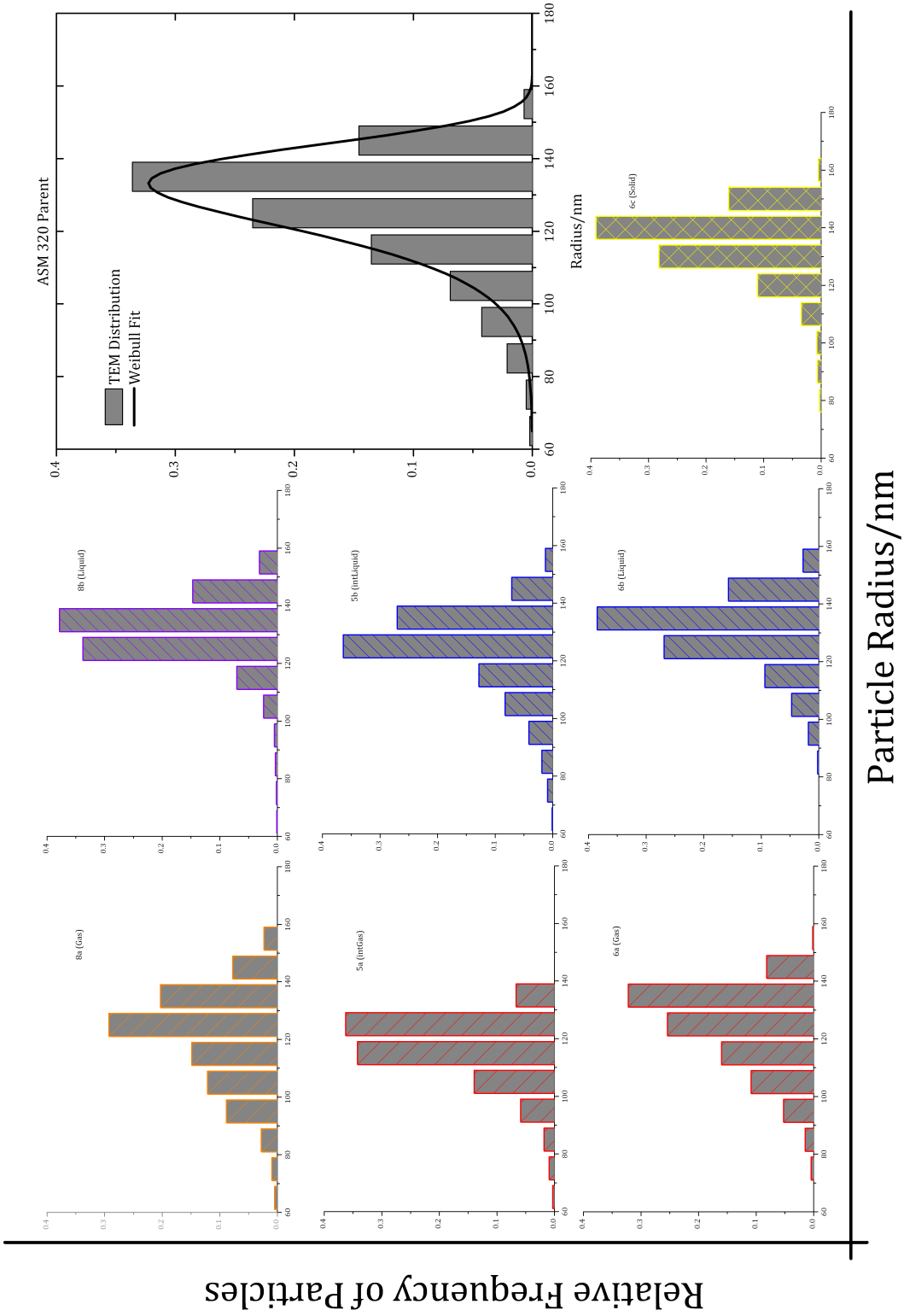

Figure 6.7 Particle size distributions of phase separating ASM320 particles, originally at 20% volume fraction. The parent particle size distribution is overlaid with a fitted Weibull distribution with mean radius 129 nm and polydispersity 10%.

to combine the accurate *in situ* radius and polydispersity measured by SAXS, with the detailed distribution information obtained from TEM.

Comparing results

When performing initial small-angle x-ray scattering experiments, we assumed the distribution of particles followed a Schulz shape. In many cases, the exact distribution is not important (see chapter 3.5) but when the details of the size and polydispersity are required in detail, for example when measuring small differences between distributions, the shape does become significant. Light scattering is concerned with the square of the volume of the particles, so scales with R^6. This means the largest particles are 'seen' more in light scattering and, by assuming a positively skewed distribution when performing a fit, it is impossible to account for the small particles in the sample, leading to a truncation of the distribution and a reduction in the polydispersity.

Electron microscopy has its own issues, described in chapter 4.2.2. In particular, the particles are required to be under vaccum to be imaged, so they will shrink. Furthermore, the stabilising layer of PHSA hairs, included in light scattering models, will collapse during the drying process. This combines to an overall decrease in the size of each particle and thus the average size, while the width of the distribution will remain more or less the same. As a result, the measured polydispersity will be larger than the *in situ.* value. Therefore in order to quantitatively compare the microscopy and scattering data, scattering form factors were calculated from the TEM distributions, using a polydisperse core-shell single particle form factor [74].

The form factors were calculated from histogram bin centres and frequencies, using a discretised form of equation 4.30 (page 57), where the shell thickness, scattering density, ρ_{shell}, and the average radius of the distribution, R_{TEMff}, were adjustable parameters. Identical swelling (a shift in the distribution) of the particles, as well as volume dependent swelling (increasing the spread of the distribution) were considered; a combination of both swelling parameters was usually the best fit to the scattering data.

The goodness of fit of the calculated form factor to the experimental data was determined by minimising the sum of the square of the residuals for each point i, $\mathrm{Min}(\Sigma_i(y_i^{exp} - y_i^{calculated})^2)$. Since scattered intensity covers many orders of

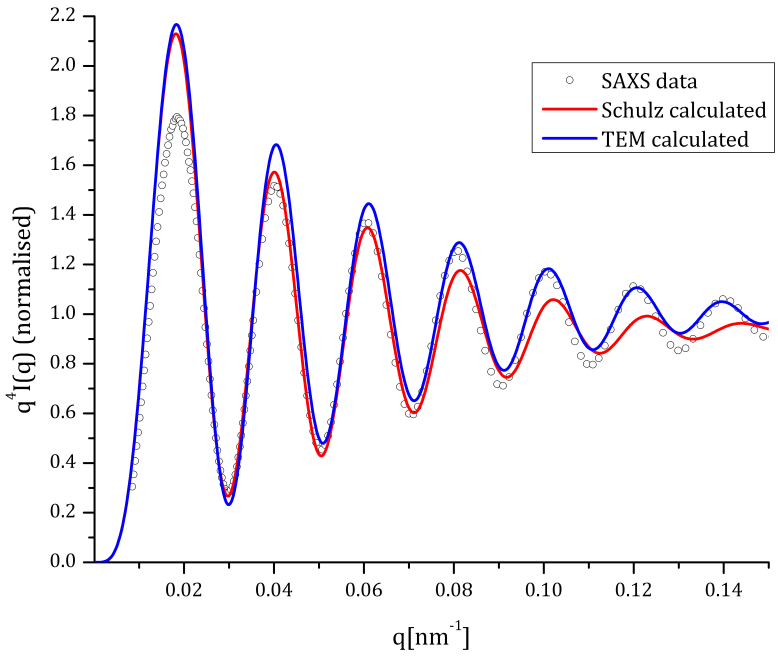

Figure 6.8 A Porod plot of form factors for the parent ASM320 particles. The points are the data as measured from SAXS, the red line is the Schulz-calculated form factor and the blue line is the form factor generated from the TEM distribution.

magnitude, fitting using residuals would preferentially fit the highest intensity data. To combat this problem, the analysis was performed on Porod plots of the data: the scattered intensity is multiplied by q^4. This results in an oscillating envelope function, as shown in figure 6.8. The results of the fits are shown in table 6.3.

Table 6.3 Average radius and polydispersity of each coexisting 20% sample as determined by calculating a form factor from TEM data then fitting to SAXS experimental form factors.

Phase [behaviour]	R_{TEMff}/nm	$\sigma_{TEMff}/\%$	Least Squares fit
Parent	146(5)	10.4(4)	0.513
Gas [GL(fF)]	139(6)	13.0(6)	2.916
fFluid [GL(fF)]	152(6)	7.5(3)	1.144
Gas [GLS]	151(6)	7.1(3)	2.122
Liquid [GLS]	145(6)	10.9(5)	0.195
Gas [GLS]	145(6)	10.5(5)	0.252
Liquid [GLS]	147(6)	9.3(4)	1.075
Solid [GLS]	153(6)	7.9(4)	1.952

Discussion

Fractionation: By calculating form factors from TEM distributions, a good estimate of the size of the particles in each phase was determined. The qualitative trend remains the same: the most dense phase contains the larger and most monodisperse particles but combining methods leads to more sources of uncertainty. Therefore, we cannot make any statistically significant quantitative conclusions about size fractionation in samples that exhibit three-phase behaviour, but the results do indicate that polydispersity increases sequentially in the solid, liquid and gas phases.

Both the SAXS and TEM results indicate that the samples which remain as two coexisting phases, GL(fF), fractionate significantly during phase separation: the gas phase contains the smaller and most polydisperse particles, while the more dense, frustrated fluid phase retains a narrower distribution of larger particles. This is likely to be due to the large difference in volume fractions between the two phases - the gas phase needs only a small proportion of the overall number of particles, therefore it is likely that they can be easily ejected from around the gas-liquid interface. It is possible that the difference in polymer concentrations between the two coexisting phases also has an effect, but the difference in average particle size between each phase is small relative to the size of the particles so it

is more likely the volume fraction of particles is having a greater effect.

There are not yet theoretical comparisons available for systems in the short range attraction regime, but detailed calculations have been made for a system with a larger size ratio [35]. Fasolo and Sollich compared calculations of their system with a universal scaling law for particles with small polydispersities proposed by Evans *et al.* [30] and experiments. From their data, a particle distribution with parent polydispersity of $\approx 10\%$ would have a difference in the gas and liquid phases of $\Delta\sigma = 5\%$. This is in agreement with our experimental data for the two-phase samples. The GLS samples did not show such a large difference in polydispersities between the phases but, since we know crystallisation is slow in these polydisperse systems, it is probable the crystal phase has not yet reached equilibrium.

Particle swelling: During the course of the analysis, indirect measurements of particle swelling and shell thickness were made. To fit the TEM-generated form factor to that of the SAXS experimental one, the distribution was shifted by a constant factor as well as a multiplicative one, allowing for the possibility that larger particles may swell more than the smaller. The percentage swelling was between 12 and 18% in all samples. Previous studies, summarised in graphical form by Poon *et al.* [84], suggest a size dependent swelling. Given that size-dependent swelling will affect the polydispersity of the size distribution, this topic would benefit from a more systematic approach, to discover if the polydispersity of a distribution can be manipulated using solvent uptake properties of the particles. Variability in particle swelling highlights the importance of characterising particles in the solvent that is to be used in the experiments.

6.4 Summary

In this chapter we have presented results of an in-depth experimental study of the effects of colloid size polydispersity in a short-range attractive hard-sphere system. These results extend previous research on the topology of the polydisperse phase diagram, revealing the fluid-solid coexistence region not only does not widen with increasing attraction, but this narrow band of fluid-solid coexistence continues to higher polymer concentrations, in agreement with mean free energy calculations of the equilibrium phase diagram topology.

Interplay of the equilibrium and non-equilibrium phase behaviours leads to novel behaviour within the binodal region of the phase diagram, not observed in monodisperse systems. Three-phase gas-liquid-solid behaviour is observed at the edge of the binodal region. Detailed analysis of each phase suggest that the gas phase contains a wider distribution of particles, with an average radius smaller than that of the liquid and solid phases. The solid phase has the most monodisperse distribution. The question remains why these samples remain as three-phase, rather than reaching the equilibrium fluid-solid behaviour. The time required for samples within the hard-sphere FS coexistence region to reach equilibrium is long (at least 28 days) but not infinite; it would be possible to determine whether the GLS samples are actually non-equilibrium fluid-solid samples (rather than metastable GLS samples) by preparing a sample in the GLS region and letting it equilibrate for longer than 28 days.

Deeper within the binodal region, crystallisation is not observed. The topology of the phase diagram suggests that this is because the 'liquid' branch of the binodal reaches high volume fractions, where crystallisation is not observed on even the longest experimental timescales; the two phases are coexisting gas and frustrated fluid. The frustrated fluid has characteristic dynamics, so it would be straightforward to test this hypothesis.

Measurements of the average radius and polydispersity were determined using SAXS, as well as detailed information about the particle size distribution using TEM. The gas phase was significantly more polydisperse and had a smaller average radius than the coexisting liquid or solid. The magnitude of the polydispersity difference between coexisting GL phases was in agreement with experiments using particles with a similar poydispersity but larger attraction range.

In order to reconcile different methods of characterising particles, a method to generate form factors from TEM distributions was developed. Using this combination of methods, it is possible to obtain a good estimation of both the average quantities and the shape of the distribution and is therefore a stronger method of characterisation than either method alone.

This is just one system at a specific particle size, polydispersity and attraction range. Although many novel features due to the particle polydispersity were discovered and explored further, no strong conclusions were made. It would be interesting to expand the experimental system, in particular to other

polydispersities and include polymers of greater sizes relative to the particles, to explore any common features in different systems.

Chapter 7

Conclusions and Future Work

7.1 Summary of results

In this work I have used visual observations, electron microscopy, light and x-ray scattering to investigate the phase behaviour of polydisperse, hard-sphere and attractive hard-sphere colloidal systems.

7.1.1 Phase behaviour in polydisperse hard-sphere systems

We made detailed observations of the phase behaviour of polydisperse colloidal particles. Even though the particles were significantly polydisperse ($\approx 11\%$ and 12%), samples within the theoretically predicted fluid-solid coexistence showed signs of crystallisation after only a few days. The width of the region did not narrow relative to the width of the monodisperse coexistence region, although calculated phase diagrams suggest that the fluid-solid coexistence region at this polydispersity should be narrower [33].

By considering the width of the coexistence region, the slow crystallisation of the particles (suggesting the system has not yet reached equilibrium) and the second solid phase observed at long times, we concluded that the coexistence region may contain both fluid-solid and fluid-solid-solid coexistence. This is the first experimental observation of phase behaviour suggesting the existence of coexisting solid phases in a polydisperse, hard-sphere system.

The coexisting fluid and solid phases were characterised individually using transmission electron microscopy to determine any size segregation (fractionation) of particles between phases: no statistically significant fractionation was observed after 28 days, but the results of a sample left for 120 days suggest that eventually the solid contains a narrower distribution of larger particles than the coexisting fluid.

At volume fractions higher than ϕ_m, the particles no longer crystallised in the bulk, even after many months. However, these non-crystallising samples appeared fluid-like, rather than an arrested glass. The dynamics of this frustrated fluid phase were investigated further using dynamic light scattering.

Dynamic light scattering

The non-crystallising, frustrated fluid samples were further studied using the cross-correlation technique of 3d dynamic light scattering (3d DLS). 3d DLS was used to minimise any contribution of multiple scattering to the measured intensity corrleation function, present due to the highly concentrated, turbid nature of these particle suspensions. The experimental results showed dynamics associated with both ergodic (fluid) systems and non-ergodic (glass) systems.

The dynamics information obtained from the intensity correlation functions were compared with Molecular Dynamics simulations of particles with different size distributions. One of the distributions was the experimental one obtained from analysis of TEM images of the polydisperse particles used in the experiments, to allow meaningful comparison of results. The simulations showed that the largest particles (the largest 10% of the distribution) were arrested, while the smallest 10% remained mobile, giving average dynamics with both features but largely similar to the slow dynamics. Furthermore, the simulations indicate that the choice of particle size distribution is important: not all distributions that were considered displayed the same disparity in dynamics between small and large particles. Both a two-tailed distribution and one wide enough to obtain a large size ratio of smallest:largest particles is required to observed the differing dynamics.

Further analysis of the experimental light scattering data showed that each curve could be easily separated into a 'slow' of 'fast' type by the steepness of the first decay; the overall dynamics were strongly influenced by the shape of the slow

curves. This is in agreement with the simulation results. These frustrated fluid samples are also characterised by the presence of inconsistent, anomalous ageing behaviour: some samples appeared to have faster dynamics when remeasured after a period of several months.

Fractionation

The crystallising, hard-sphere samples were also scrutinised further to determine any possible fractionation of particles between the coexisting fluid and solid phases. A second batch of particles, with similar polydispersity and size to the first, were used for these experiments. The phase behaviour was initially determined by experimental observations, to find the range of volume fractions for fluid-solid coexistence. Following from this, a time series of samples, each with the same volume fraction within the FS coexistence region, were prepared. For each time point, the distribution of particles in each phase was measured using transmission electron microscopy. After 28 days, there was no statistically significant size fractionation between the fluid and crystal. After 120 days, the fluid phase contained slightly smaller, more polydisperse particles than the solid, but it was difficult to resolve the small changes with sufficient statistical accuracy using this particular batch of particles.

7.1.2 Polydisperse colloid-polymer mixtures

A complete phase diagram for a polydisperse hard-sphere system was presented in chapter 6. There are two main differences of this phase diagram from an equivalent monodisperse case. Firstly, the fluid-solid region remained at a constant width even at high polymer concentrations, in agreement with previous experimental data and calculations [31, 35]. Secondly, both a three-phase, gas-liquid-solid and a two-phase, gas-liquid were present within the metastable binodal. We proposed that the intersection of the high-ϕ boundary of the fluid-solid coexistence region and the binodal was responsible for this novel behaviour.

It is unclear whether the gas-liquid-solid behaviour is truly in equilibrium or not - polydispersity is likely to decrease the gap in the free energies of the solid phase and the metastable gas-liquid, but it would only be at equilibrium if the common tangent construction allows for all three phases to have the same chemical potential and osmotic pressure. The other option is that the system

is attempting to reach a gas-solid equilibrium, but the kinetics of crystallisation in this polydisperse system is so slow that it remains a non-equilibrium state on experimental timescales. In general, it is likely that the high entropic cost for ordering particles in a polydisperse crystal means we are unlikely to observe behaviour predicted by theoretical work or simulations.

Possible fractionation between coexisting phases of samples within the binodal region was also investigated. The size and polydispersity of each phase was measured using transmission electron microscopy and small-angle x-ray scattering. The three-phase samples did not show significant size fractionation, while the two phase samples within the binodal did exhibit fractionation: the gas contained a wide distribution of smaller particles, while the liquid contained a narrower distribution of larger particles.

Throughout this thesis, transmission electron microscopy and x-ray scattering were used to characterise size and polydispersity of coexisting phases. A robust method of obtaining probability size distributions from electron micrographs was developed, as well as a technique to translate the psds into scattering form factors. A combination of both techniques is necessary to fully characterise a polydisperse system.

In conclusion, the presence of size polydispersity in hard-sphere and attractive, hard-sphere systems leads to non-trivial, qualitative differences in the phase behaviour and dynamics of the particles compared to a system of monodisperse particles. Although we discovered and investigated several features in the hard-sphere and attractive hard-sphere systems, a lack of other literature on similar systems, particularly experimental work, makes it difficult to form a complete understanding of the system. However, this does mean that there is plenty of scope for future research on this topic.

7.2 Future work

These experiments were undertaken with particles of just one polydispersity, so an obvious route for future work would be to repeat these experiments for other polydispersities. It would be particularly interesting to discover whether the shape of the particle size distribution has any effect on phase behaviour.

Similarly, only one colloid-polymer size ratio was considered in this work;

experiments to verify theoretical predictions at other size rations could reveal new phase behaviour.

Another direction to pursue would be binary colloidal systems. There are already some parallels between binary and polydisperse hard-sphere systems, namely the non-crystallising, non-equilibrium regions observed in both systems. It would be interesting to discover if there is a unifying mechanism responsible, or at what polydispersity particle suspensions change from acting like a polydisperse, frustrated fluid to a binary 'glass'. In general, the disparity between theoretically predicted equilibrium phases and the difficulties of reaching equilibrium in experimental polydisperse and binary systems would be very interesting to investigate further.

Non-crystallising behaviour is particularly interesting, and relevant to the metallic glass community, but crystal structures are also studied extensively. The combination of two polydisperse distributions of particle in a 'binary' phase diagram could be a viable method of discovering new superlattice structures.

Finally, there is much scope left in the area of colloid-polymer phase behaviour by considering attractive, binary hard-sphere mixtures.

Appendix A

Extracting PSDs from TEM micrographs

Transmission electron microscopy (TEM) was used to directly measure the probability size distributions (PSDs) of batches of particles and also to investigate the possibility of size fractionation of particles between coexisting phases (chapters 5.2 and 6.3.2). While simple image processing techniques are sufficient for well-separated, high contrast particles, the micrographs obtained were generally not so simple to process. The sequence of steps that produced reliably good PSDs was described in chapter 4.2.2; the information provided in this Appendix is to motivate the decision of using Feret's diameter, or the Feret diameter, as the measure of the particle size.

A.1 Using the Feret diameter to measure radii of particles

The image processing routine developed in Fiji outputs a selection of parameters for each particle. With a range of options to calculate the particle radii, the area of each particle is an obvious choice: the area will have the largest pixel value and circularity can be assumed. Unfortunately, the processing steps often output particles which are smaller than the actual particle, particularly when the particles are densely clustered on the image. While it is straightforward to discard all but the most circular particles from the analysis ("Circularity" is an outputted

parameter) it is not an ideal solution - if, for example, the smaller particles are more often badly segmented, discarding them will lead to a distribution that has a different shape to the true distribution.

To solve this problem, the Feret diameter was used. The Feret diameter of an object is the maximum end-to-end distance of the object, also known as the the maximum caliper. For a circular object, the maximum length the Feret diameter can be is the diameter of the circle. Furthermore, for selections that should be circular, so long as at least half of the circumference is present, the measured Feret diameter will still be the diameter of the original circle. This last point is illustrated in figure A.1: one particle was selected and copied five times. The copies then had a random area removed, shown in the left panel. The image was processed using the steps outlined in figure 4.2.2 (middle panel). To check visually that the Feret diameter outputs a reasonable 'particle', a simple script was written to overlay the Feret diameter (yellow line) and the resultant 'particle' (yellow circle) centred on the midpoint of that line.

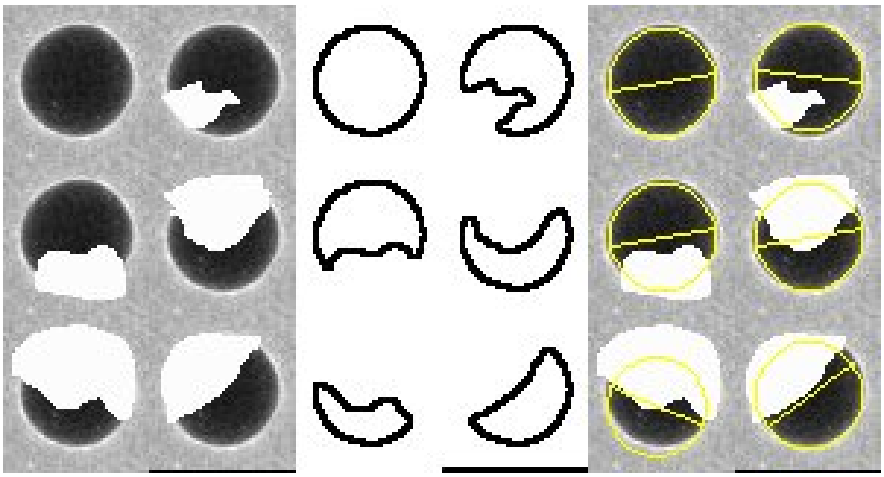

Figure A.1 Example of using the Feret diameter to measure circular particles when the image is not circular. Left panel: original particle and 5 copies with selections removed. Middle panel: output after application of particle measuring routine. Right panel: overlay of resultant Feret diameters (yellow lines) and bounding circles (yellow circles) of each line.

One of the parent distributions was also checked by measuring the particles "by hand". This is similar to a method utilised by Schöpe *et. al.* to measure PSDs from scanning electron microscope images of sterically stabilised polymer particles [103]. Their technique was as follows:

> To determine the PSD, the images obtained by SEM were printed on a poster printer on A0 paper so that each particle was not smaller

than 10 mm. Each particle diameter was measured four times in different orientations using a digital calliper. To obtain a reference measurement, a test image was generated consisting of 100 images of the same particle, arranged randomly as isolated particles, doublets, triplets, and so on. All measured PSDs were deconvoluted using this measurement to reduce instrumental uncertainty.

Similarly, the ASM320 particles were hand-counted in Fiji. Each image was zoomed in to 400× magnification so each particle was approximately 40 mm in diameter. The oval tool was selected and constrained (using the shift key) to a circle as it was drawn over a particle. The circle was measured (M key) and the corresponding area was then deleted to avoid double counting. The resultant distributions agreed in shape, with the hand-counted particles tending to have larger radii than those measured by the Feret diameter.

To determine where this error originated, one particle was copied 512 times and measured by hand. The deviations from the mode tended to be overestimations of one pixel in the radius; only one out of the 512 had a radius smaller than the mode. The conclusion from this hand-counting analysis is that using the Image processing steps and use of the Feret diameter to measure the particle radii obtains a distribuion equivalent to one that would be obtained by much more tedious hand-counting methods.

A.2 Estimation of error in the standard deviation

How good is the estimate of the polydispersity? The error in the polydispersity is a combination of the errors in the mean and the standard deviation of the distribution. Bootstrapping gives a measure of the consistency of the parameter. In other words, it gives an estimate of the error on a sample parameter which, in this case, is the standard deviation of the distribution.

The process of bootstrapping consists of generating a number of distributions obtained from one parent distribution. A list of entries is sampled with replacement to create a new list with the same number of entries, so there will be repeated entries in the list. To obtain an estimate of the sampling error in the TEM distribution measurements, a sample of 366 particles was used. 300 new distributions were obtained by sampling with replacement from those 366

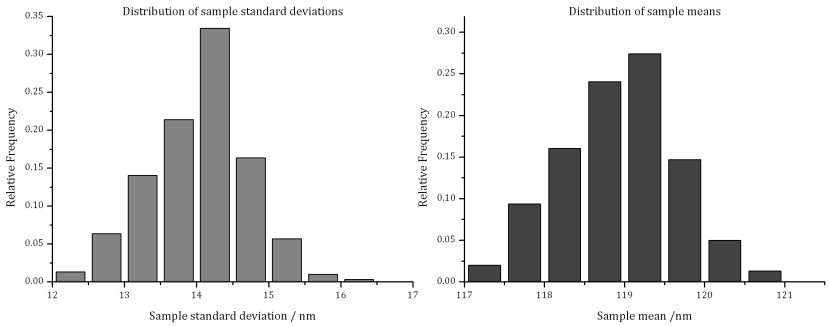

Figure A.2 Distributions of the mean (left) and standard deviation (right) of 300 resamples of 366 particles. The spread of values gives an estimate of the errors in the mean and standard deviation associated with sampling from a population.

particles. The standard deviation and mean of each new distribution was then calculated, creating a distribution of parameters, shown in figure A.2.

The results of the resampling give an average mean of 118.92 ± 0.04 nm and average standard deviation 14.04 ± 0.04 nm, which combine to give an error of $\approx 0.03\%$ in the polydispersity.

In conclusion, the combination of the image processing steps outlined in chapter 4.2.2 and the use of the Feret diameter as a measure of particle size produces a particle size distribution as good as that obtained by measuring each particle individually.

Appendix B

Binary Phase diagrams

The phase diagrams presented in the figures of this appendix were created with the aim of matching amorphous experimental points with regions on a relevant, theoretical $\phi_A - \phi_B$ phase diagram where multiple solid regions are predicted. Size polydispersity introduces quantitative and qualitative changes to single-component systems and the effect of polydispersity of the components of a binary system has not been systematically explored; it is likely that the phase topology of an experimental binary system will not match exactly with the theoretical or calculated phase boundaries. Furthermore, phase boundaries are not available for every size ratio, so we are justified in moving and stretching phase boundaries to attempt to fit better the experimental data.

The experimental data points were extracted from published data using DataThief [115]. The data was re-plotted in Excel and the graphs were imported into Inkscape [44]. Theoretical phase diagrams were also copied from published work (listed in table B.1 and re-sized in Inkscape to match the scales on the experimental plots. The theoretical boundaries were traced using a line tool to allow manipulation of each boundary. The size ratio for each experimental diagram was then matched to the closest available theoretical one, and the boundaries were manipulated with the goal to a) place crystallising points in appropriate theoretical regions and b) place amorphous points outwith fluid+crystal regions, that is, either in regions where multiple solids are predicted, at volume fractions beyond $\phi_g = 0.58$ (denoted by a grey line in the figures), or in the single-phase fluid region at low volume fractions.

The manipulated diagram is shown on the right of each pair of figures, while

on the left is the manipulated diagram, overlaid with the original theoretical phase lines (black). Many of the diagrams showed good agreement of theoretical and experimental points with only small manipulations, while others had many experimental points remaining in the 'wrong' region, even after manipulation. Many, but not all, of the amorphous experimental samples can be accounted for by their position in a multiple-solid regions of the theoretical diagram.

This background work provides motivation for a systematic study of the effects of polydispersity on binary phase diagrams, as well as an investigation of the kinetics of binary superlattice formation.

Label (Figure)	Size Ratio, α	Source
	Experimental	
w30212 (1)	0.3846	[101]
w20212 (2)	0.399	[101]
PSAB6 (2)	0.4	[100]
1fSPR (3)	0.428	[99]
1eSPR (3)	0.454	[99]
1dSPR (4)	0.476	[99]
1cSPR (4)	0.487	[99]
1bSPR (5)	0.508	[99]
w10212 (9)	0.736	[101]
	Theoretical	
TEM0.414	0.414	[114]
LISS0.4	0.4	[37]
HFD0.74	0.74	[50]
THE1a0.5	0.5	[29]
THE1b0.54	0.54	[29]
THTa0.414	0.414	[114]
THTb0.45	0.45	[114]

Table B.1 Sources and size ratios of the experimental data and theoretical diagrams used in this section.

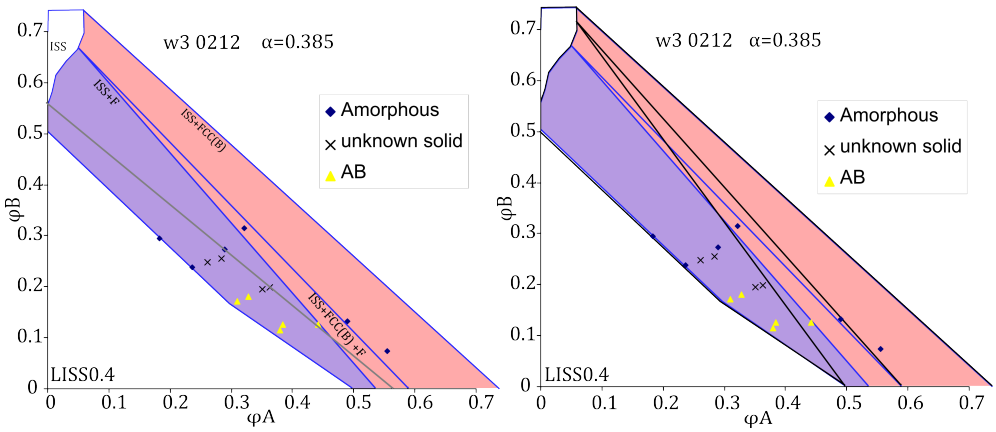
w3 0212 α=0.385
ISS
ISS+F
ISS+FCC(B)
ISS+FCC(B)+F
Amorphous
unknown solid
AB
LISS0.4
φB
φA
0
0.1
0.2
0.3
0.4
0.5
0.6
0.7
w3 0212 α=0.385
Amorphous
unknown solid
AB
LISS0.4
φB
φA

Figure B.1

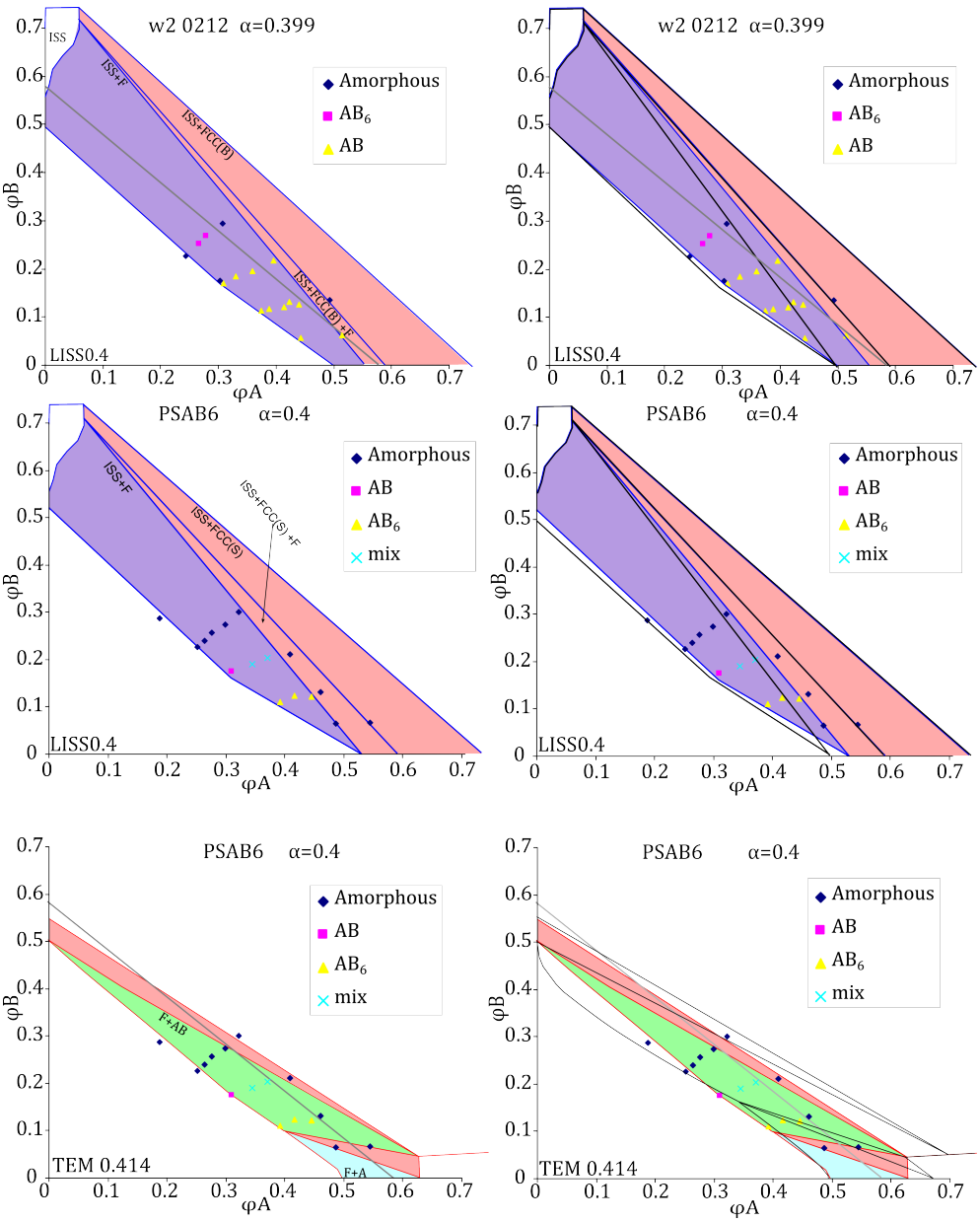
w2 0212 α=0.399
ISS
ISS+F
ISS+FCC(B)
ISS+FCC(B)+F
Amorphous
AB6
AB
LISS0.4
φB
φA
PSAB6 α=0.4
ISS+FCC(S)+F
ISS+FCC(S)
mix
F+AB
F+A
TEM 0.414

Figure B.2

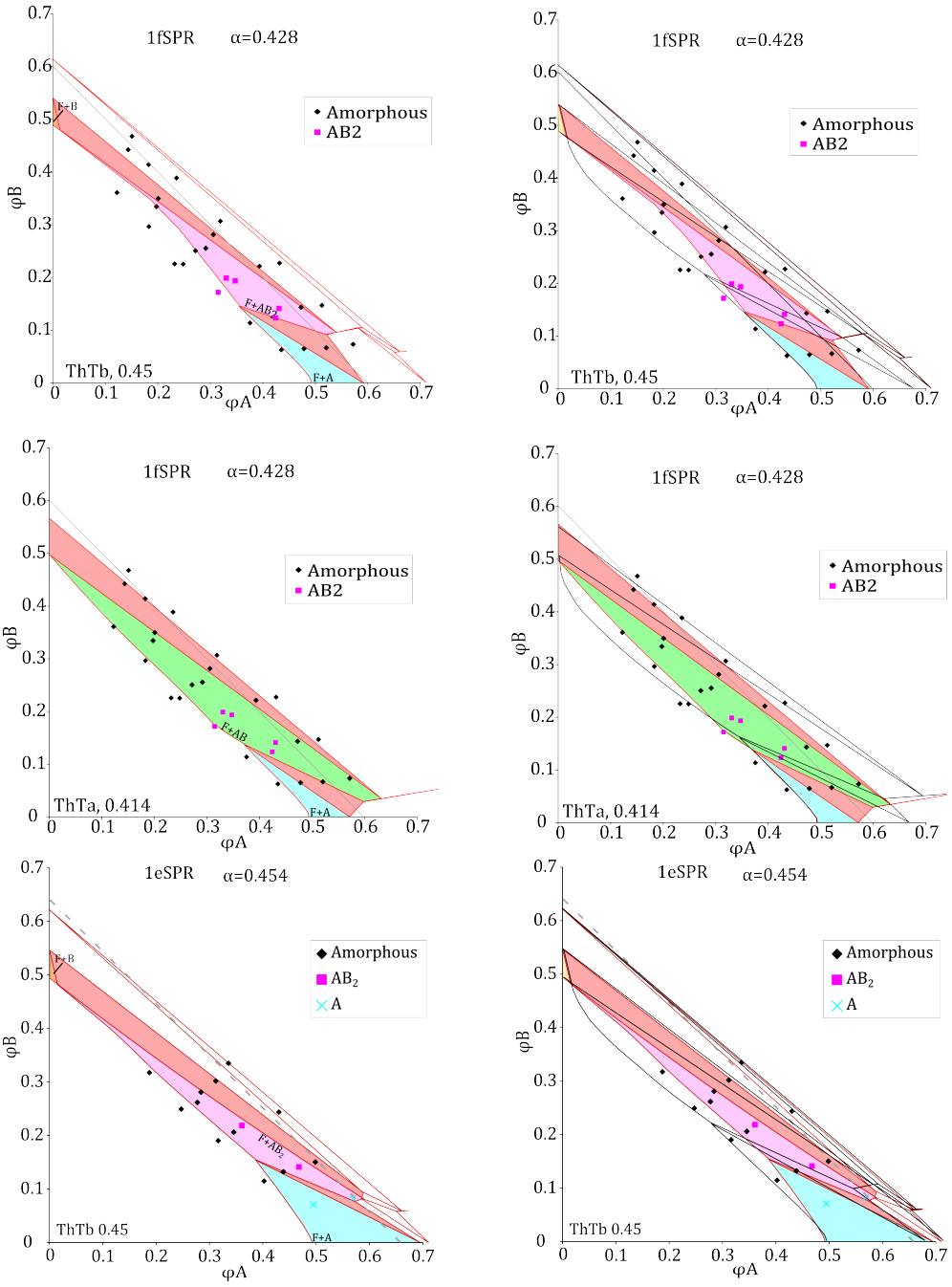
1fSPR α=0.428
Amorphous
AB2
F+B
F+AB2
F+A
ThTb, 0.45
φB
φA
1fSPR α=0.428
Amorphous
AB2
ThTb, 0.45
φB
φA
1fSPR α=0.428
Amorphous
AB2
F+AB
F+A
ThTa, 0.414
φB
φA
1fSPR α=0.428
Amorphous
AB2
ThTa, 0.414
φB
φA
1eSPR α=0.454
Amorphous
AB2
A
F+B
F+AB2
F+A
ThTb 0.45
φB
φA
1eSPR α=0.454
Amorphous
AB2
A
ThTb 0.45
φB
φA

Figure B.3

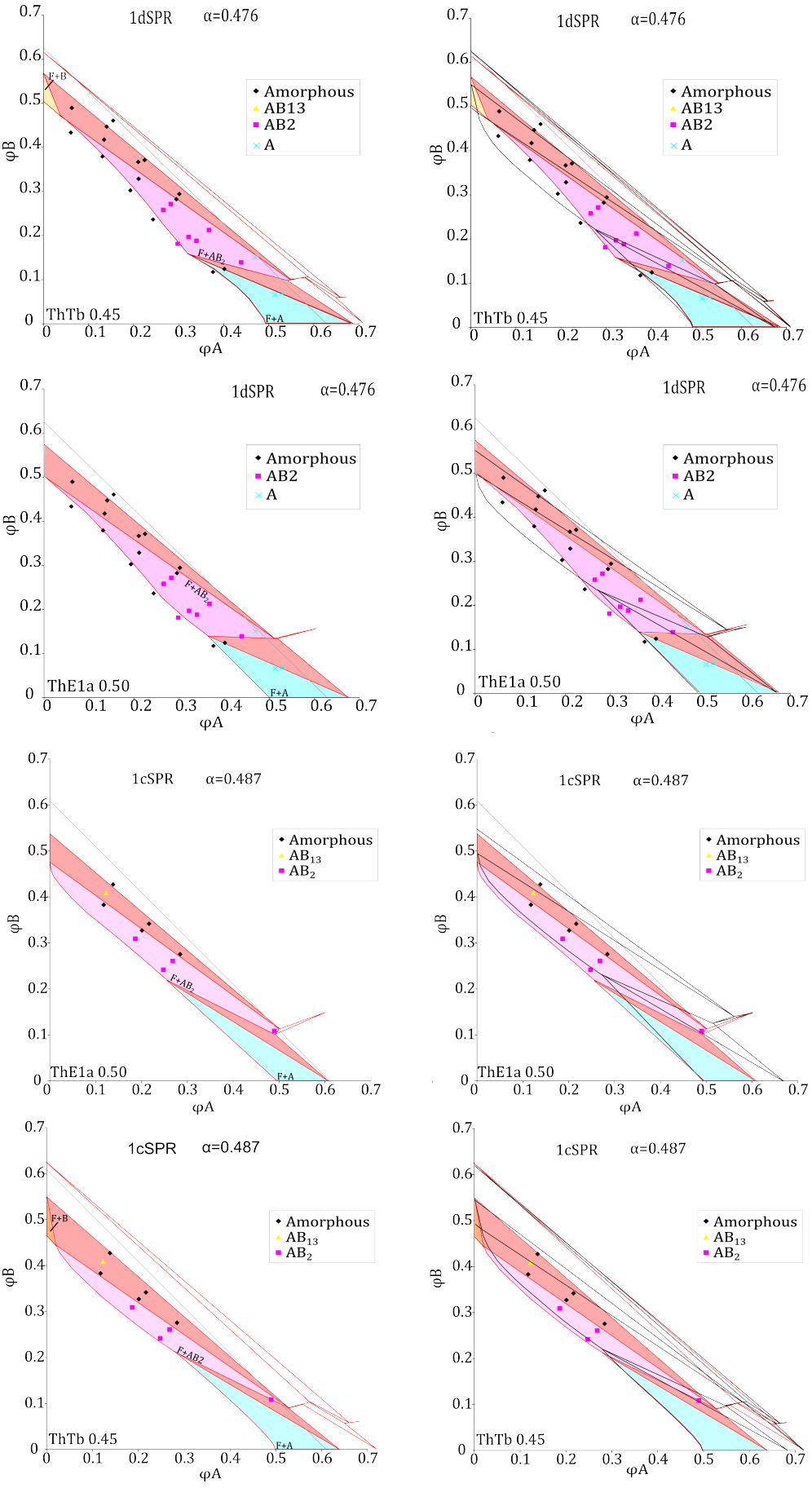
1dSPR α=0.476
Amorphous
AB13
AB2
A
F+B
F+AB2
F+A
ThTb 0.45
φB
φA
1dSPR α=0.476
Amorphous
AB13
AB2
A
ThTb 0.45
φB
φA
1dSPR α=0.476
Amorphous
AB2
A
F+AB2
F+A
ThE1a 0.50
φB
φA
1dSPR α=0.476
Amorphous
AB2
A
ThE1a 0.50
φB
φA
1cSPR α=0.487
Amorphous
AB13
AB2
F+AB2
F+A
ThE1a 0.50
φB
φA
1cSPR α=0.487
Amorphous
AB13
AB2
ThE1a 0.50
φB
φA
1cSPR α=0.487
Amorphous
AB13
AB2
F+B
F+AB2
F+A
ThTb 0.45
φB
φA
1cSPR α=0.487
Amorphous
AB13
AB2
ThTb 0.45
φB
φA

Figure B.4

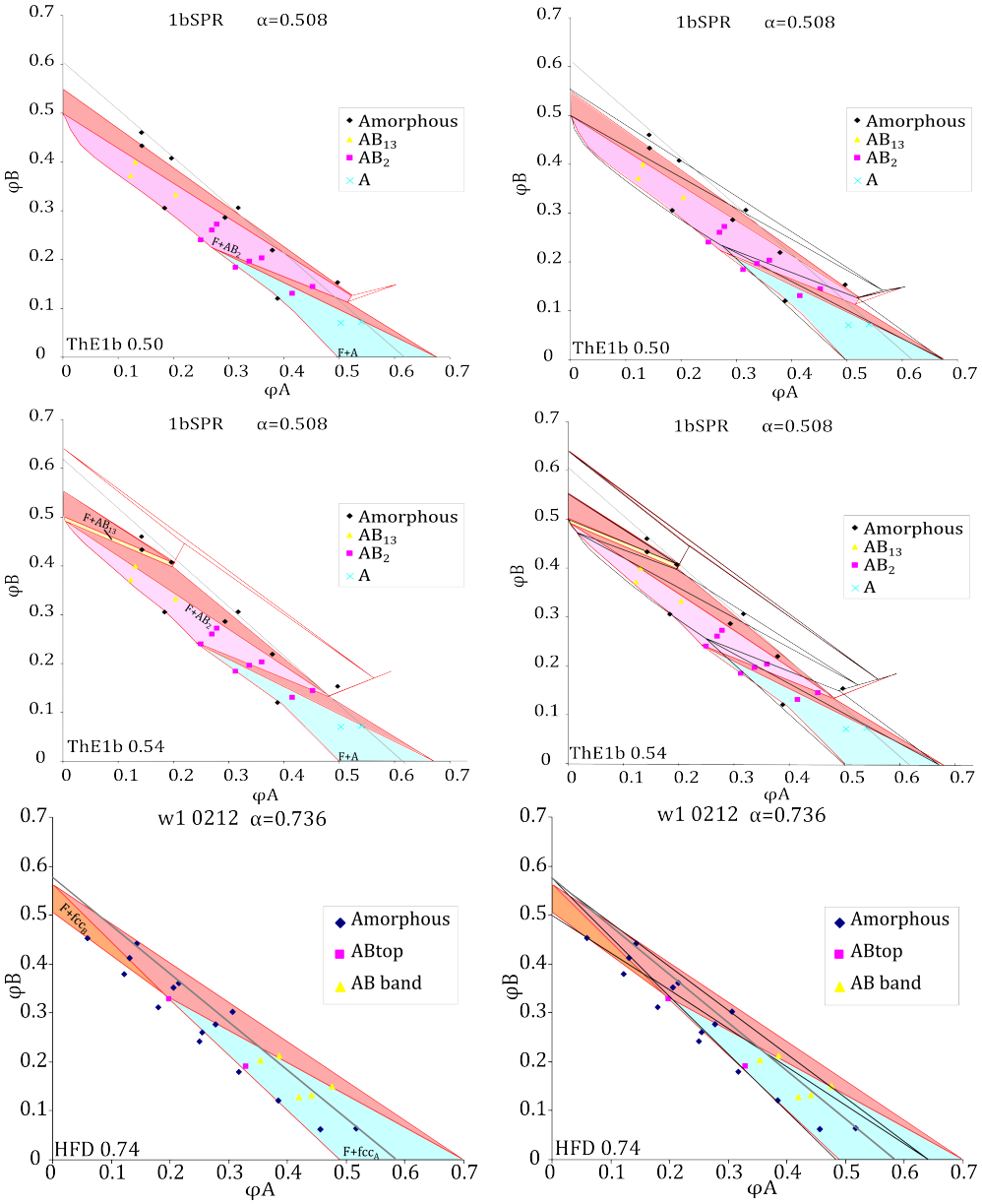
1bSPR α=0.508
Amorphous
AB13
AB2
A
F+AB2
F+A
ThE1b 0.50
φA
φB
1bSPR α=0.508
Amorphous
AB13
AB2
A
ThE1b 0.50
φA
φB
1bSPR α=0.508
Amorphous
AB13
AB2
A
F+AB13
F+AB2
F+A
ThE1b 0.54
φA
φB
1bSPR α=0.508
Amorphous
AB13
AB2
A
ThE1b 0.54
φA
φB
w1 0212 α=0.736
Amorphous
ABtop
AB band
F+fccB
F+fccA
HFD 0.74
φA
φB
w1 0212 α=0.736
Amorphous
ABtop
AB band
HFD 0.74
φA
φB

Figure B.5

Bibliography

[1] Aste, T. "Circle, sphere, and drop packings." *Physical Review E* 53, 3: (1996) 2751–2579. doi: 10.1103/PhysRevE.53.2571.

[2] Auer, S., and D. Frenkel. "Suppression of crystal nucleation in polydisperse colloids due to increase of the surface free energy." *Nature* 413, 6857: (2001) 711–3. doi: 10.1038/35099513.

[3] Barrat, J. L., and J. P. Hansen. "On the stability of polydisperse colloidal crystals." *Journal de Physique* 47: (1986) 1547–1553. doi: 10.1051/jphys:019860047090154700.

[4] Bartlett, P. "A geometrically-based mean-field theory of polydisperse hard-sphere mixtures." *The Journal of Chemical Physics* 107, October 1996: (1997) 188–196. doi: 10.1063/1.474364.

[5] Bartlett, P. "Freezing in polydisperse colloidal suspensions." *Journal of Physics: Condensed matter* 12: (2000) 275–280. doi: 10.1088/0953-8984/12/8A/335.

[6] Bartlett, P., and R. H. Ottewill. "A neutron scattering study of the structure of a bimodal colloidal crystal." *The Journal of Chemical Physics* 96, 4: (1992) 3306. doi: 10.1063/1.461926.

[7] Bartlett, P., R. H. Ottewill, and P. N. Pusey. "Superlattice formation in binary mixtures of hard-sphere colloids." *Physical Review Letters* 68, 25. doi: 10.1103/PhysRevLett.68.3801.

[8] Bernal, J. "Geometry of the structure of monatomic liquids." *Nature* 185: (1960) 68–70. doi: 10.1038/185068a0.

[9] Berne, B. J., and R. Pecora. *Dynamic light scattering : with applications to chemistry, biology, and physics / Bruce J. Berne and Robert Pecora.* New York : Wiley, 1976.

[10] Berry, G. C. "Thermodynamic and Conformational Properties of Polystyrene. I. Light-Scattering Studies on Dilute Solutions of Linear Polystyrenes." *The Journal of Chemical Physics* 44, 12: (1966) 4550. doi: 10.1063/1.1726673.

[11] Bodnár, I., J. K. G. Dhont, and H. N. W. Lekkerkerker. "Pretransitional phenomena of a colloid polymer mixture studied with static and dynamic light scattering." *The Journal of Physical Chemistry* 100, 50: (1996) 19,614–19,619. doi: 10.1021/jp962553v.

[12] Bosma, G., C. Pathmamanoharan, E. de Hoog, W. Kegel, A. van Blaaderen, and H. Lekkerkerker. "Preparation of monodisperse, fluorescent PMMA-latex colloids by dispersion polymerization." *Journal of Colloid and Interface Science* 245, 2: (2002) 292–300. doi: 10.1006/jcis.2001.7986.

[13] Brambilla, G., D. El Masri, M. Pierno, L. Berthier, L. Cipelletti, G. Petekidis, and A. B. Schofield. "Probing the equilibrium dynamics of colloidal hard spheres above the mode-coupling glass transition." *Physical Review Letters* 102, 8: (2009) 085,703. doi: 10.1103/PhysRevLett.102.085703.

[14] Brown, R. "A brief account of microscopical observations made in the months of June, July and August 1827, on the particles contained in the pollen of plants." *Edinburgh new Philosophical Journal* 358–371. (1828).

[15] Campbell, A. I., and P. Bartlett. "Fluorescent Hard-Sphere Polymer Colloids for Confocal Microscopy." *Journal of Colloid and Interface Science* 256, 2: (2002) 325–330. doi: 10.1006/jcis.2002.8669.

[16] CERN Communication Group. *LHC the guide*. CERN, 2008, cern-brochure-2008-001-eng edition. Accessed: 28-01-2014.

[17] Chaikin, P., and T. C. Lubensky. *Principles of Condensed Matter Physics*. Cambridge University Press, 1995.

[18] Chen, M. "Mechanical Behavior of Metallic Glasses: Microscopic Understanding of Strength and Ductility." *Annual Review of Materials Research* 38, 1: (2008) 445–469. doi: 10.1146/annurev.matsci.38.060407.130226.

[19] Chew, J. W., D. M. Parker, R. a. Cocco, and C. M. Hrenya. "Cluster characteristics of continuous size distributions and binary mixtures of Group B particles in dilute riser flow." *Chemical Engineering Journal* 178: (2011) 348–358. doi: 10.1016/j.cej.2011.10.020.

[20] Colvin, V. L. "From opals to optics : colloidal photonic crystals." *MRS Bulletin* 26, 8: (2001) 637–641. doi: 10.1557/mrs2001.159.

[21] Coniglio, A., A. de Candia, and A. Fierro. "Dynamical heterogeneities in the crossover region from colloidal gels to colloidal glasses." *AIP Conference Proceedings* 379: (2013) 379–383. doi: 10.1063/1.4794600.

[22] Dawson, K. A. "The glass paradigm for colloidal glasses, gels, and other arrested states driven by attractive interactions." *Current Opinion in Colloid & Interface Science* 7, 3-4: (2002) 218–227. doi: 10.1016/S1359-0294(02)00052-3.

[23] Desmond, K. W., and E. R. Weeks. "Influence of Particle Size Distribution on Random Close Packing of Spheres." *http://arxiv.org/abs/1303.4627* (2013).

[24] Di Cola, E., A. Moussaid, M. Sztucki, T. Narayanan, and E. Zaccarelli. "Correlation between structure and rheology of a model colloidal glass." *The Journal of Chemical Physics* 131, 14: (2009) 144,903. doi: 10.1063/1.3240345.

[25] Dickinson, E., and R. Parker. "Polydispersity and the fluid-crystalline phase transition." *Journal de Physique Lettres* 46, 6: (1985) 229–232. doi: 10.1051/jphyslet:01985004606022900.

[26] Dinsmore, A. D., E. R. Weeks, V. Prasad, A. C. Levitt, and D. A. Weitz. "Three-dimensional confocal microscopy of colloids." *Applied optics* 40, 24: (2001) 4152–9. doi: 10.1364/AO.40.004152.

[27] Einstein, A. "Investigations on the Theory of the Brownian Movement." *Ann. Phys.* 17. (1905).

[28] El Masri, D., G. Brambilla, M. Pierno, G. Petekidis, A. B. Schofield, L. Berthier, and L. Cipelletti. "Dynamic light scattering measurements in the activated regime of dense colloidal hard spheres." *Journal of Statistical Mechanics: Theory and Experiment* P07015. doi: 10.1088/1742-5468/2009/07/P07015.

[29] Eldridge, M. D., P. A. Madden, P. N. Pusey, and P. Bartlett. "Binary hard-sphere mixtures: a comparison between computer simulation and experiment." *Molecular Physics* 84, 2: (1995) 395–420. doi: 10.1080/00268979500100271.

[30] Evans, R. M. L., D. J. Fairhurst, and W. C. K. Poon. "Universal Law of Fractionation for Slightly Polydisperse Systems." *Physical Review Letters* 81, 6: (1998) 1326–1329. doi: 10.1103/PhysRevLett.81.1326.

[31] Fairhurst, D. J. *Polydispersity in Colloidal Phase Transitions*. Ph.D. thesis, University of Edinburgh, 1999.

[32] Fairhurst, D. J., and R. M. L. Evans. "De-mixing of polydisperse fluids: experimental test of a universal relation." *Colloid & Polymer Science* 282, 7: (2004) 766–769. doi: 10.1007/s00396-003-1019-6.

[33] Fasolo, M., and P. Sollich. "Equilibrium phase behavior of polydisperse hard spheres." *Physical Review Letters* 91, 6: (2003) 6–9. doi: 10.1103/PhysRevLett.91.068301.

[34] Fasolo, M., and P. Sollich. "Fractionation effects in phase equilibria of polydisperse hard-sphere colloids." *Physical Review E* 70, 4: (2004) 14–20. doi: 10.1103/PhysRevE.70.041410.

[35] Fasolo, M., and P. Sollich. "Effects of colloid polydispersity on the phase behavior of colloid-polymer mixtures." *The Journal of Chemical Physics* 122, 7: (2005) 074,904. doi: 10.1063/1.1851978.

[36] Fasolo, M., and P. Sollich. "Effects of polymer polydispersity on the phase behaviour of colloid-polymer mixtures." *Journal of Physics: Condensed Matter* 17, 6: (2005) 797. doi: 10.1088/0953-8984/17/6/002.

[37] Filion, L. *Self-assembly in colloidal hard-sphere systems.* Ph.D. thesis, Utrecht University, 2011.

[38] Filion, L., M. Marechal, B. van Oorschot, D. Pelt, F. Smallenburg, and M. Dijkstra. "Efficient method for predicting crystal structures at finite temperature: variable box shape simulations." *Physical Review Letters* 103, 18: (2009) 1–4. doi: 10.1103/PhysRevLett.103.188302.

[39] Fleer, G., and R. Tuinier. "Analytical phase diagrams for colloids and non-adsorbing polymer." *Advances in colloid and interface science* 143, 1-2: (2008) 1–47. doi: 10.1016/j.cis.2008.07.001.

[40] Friedrich, C., W. Gleinser, E. Korat, D. Maier, and J. Weese. "Comparison of sphere-size distributions obtained from rheology and transmission electron microscopy in PMMA/PS blends." *Journal of Rheology* 39, 6: (1995) 1411–1425. doi: 10.1122/1.550720.

[41] Gast, A., C. Hall, and W. Russel. "Polymer-induced phase separations in nonaqueous colloidal suspensions." *Journal of Colloid and Interface Science* 96, 1: (1983) 251–267. doi: 10.1016/0021-9797(83)90027-9.

[42] Groot, R. D., and S. D. Stoyanov. "Close packing density and fracture strength of adsorbed polydisperse particle layers." *Soft Matter* 7, 10: (2011) 4750. doi: 10.1039/c0sm00859a.

[43] van Gruijthuijsen, K., R. Tuinier, J. M. Brader, and A. Stradner. "Phase behaviour of colloids with short-range repulsions plus nonadsorbing polymer chains." *Soft Matter* 9, 42: (2013) 9977. doi: 10.1039/c3sm51432c.

[44] Harrington, B., and The Inkscape Team. "Inkscape v0.48.", 2013. `www.inkscape.org`. Accessed: 1-4-2014.

[45] Higgs, P. W. "Broken Symmetries and the Masses of Gauge Bosons." *Physical Review Letters* 13, 16: (1964) 508–509. doi: 10.1103/PhysRevLett.13.508.

[46] Hirata, A., P. Guan, T. Fujita, Y. Hirotsu, A. Inoue, A. Yavari, T. Sakurai, and M. Chen. "Direct observation of local atomic order in a metallic glass." *Nature Materials* 10, 1: (2011) 28–33. doi: 10.1038/nmat2897.

[47] Hoover, W. G., and F. H. Ree. "Melting transition and communal entropy for hard spheres." *The Journal of Chemical Physics* 49, 8: (1968) 3609. doi: 10.1063/1.1670641.

[48] Hu, Y., D. Lan, G. Dai, H. Jiang, L. Duan, and B. C. Wei. "Study on crystallization kinetics of binary alloys through model colloidal mixtures." *Journal of Alloys and Compounds* 504: (2010) S243–S246. doi: 10.1016/j.jallcom.2010.02.151.

[49] Hunt, N., R. Jardine, and P. Bartlett. "Superlattice formation in mixtures of hard-sphere colloids." *Physical Review E* 62, 1 Pt B: (2000) 900–13. doi: 10.1103/PhysRevE.62.900.

[50] Hynninen, A.-P., L. Filion, and M. Dijkstra. "Stability of LS and LS2 crystal structures in binary mixtures of hard and charged spheres." *The Journal of chemical physics* 131, 6: (2009) 064,902. doi: 10.1063/1.3182724.

[51] Hynninen, A. P., J. H. J. Thijssen, E. C. M. Vermolen, M. Dijkstra, and A. van Blaaderen. "Self-assembly route for photonic crystals with a bandgap in the visible region." *Nature Materials* 6, 3: (2007) 202–5. doi: 10.1038/nmat1841.

[52] Ilett, S. M., A. Orrock, W. C. K. Poon, and P. N. Pusey. "Phase behavior of a model colloid-polymer mixture." *Physical Review E* 51, 2: (1995) 1344. doi: 10.1103/PhysRevE.51.1344.

[53] Imhof, A., and J. Dhont. "Experimental phase diagram of a binary colloidal hard-sphere mixture with a large size ratio." *Physical review letters* 75, 8: (1995) 1662–1665. doi: 10.1103/PhysRevLett.75.1662.

[54] Jones, R. A. L. *Soft Condensed Matter*. Oxford University Press, 2002.

[55] Korgel, B. A., S. Fullam, S. Connolly, and D. Fitzmaurice. "Assembly and self-organization of silver nanocrystal superlattices: ordered soft spheres." *The Journal of Physical Chemistry B* 102, 43: (1998) 8379–8388. doi: 10.1021/jp981598o.

[56] Kozina, A., D. Sagawe, P. Díaz-Leyva, E. Bartsch, and T. Palberg. "Polymer-enforced crystallization of a eutectic binary hard sphere mixture." *Soft Matter* 8, 3: (2012) 627. doi: 10.1039/c1sm06699d.

[57] Kurita, R., and E. R. Weeks. "Experimental study of random-close-packed colloidal particles." *Physical Review E* 82, 1: (2010) 011,403. doi: 10.1103/PhysRevE.82.011403.

[58] Lasue, J., R. Botet, A. C. Levasseur-Regourd, E. Hadamcik, and W. Kofman. "Appearance of layered structures in numerical simulations of polydisperse bodies accretion: Application to cometary nuclei." *Icarus* 213, 1: (2011) 369–381. doi: 10.1016/j.icarus.2011.02.026.

[59] Lebowitz, J., E. Helfand, and E. Praestgaard. "Scaled particle theory of fluid mixtures." *The Journal of Chemical Physics* 43, 3: (1965) 774–779. doi: 10.1063/1.1696842.

[60] Lekkerkerker, H. N. W., W. Poon, P. N. Pusey, A. Stroobants, and P. B. Warren. "Phase-behavior of colloid + polymer mixtures." *Europhysics Letters* 20, 6: (1992) 559–564. doi: 10.1209/0295-5075/20/6/015.

[61] Liddle, S. M., T. Narayanan, and W. C. K. Poon. "Polydispersity effects in colloidpolymer mixtures." *Journal of Physics: Condensed Matter* 23, 19: (2011) 194,116. doi: 10.1088/0953-8984/23/19/194116.

[62] Lindemann, F. A. "The calculation of molecular natural frequencies." *Physikalische Zeitschrift* 11: (1910) 609–612.

[63] Liu, J., and M. C. Hersam. "Recent developments in carbon nanotube sorting and selective growth." *MRS Bulletin* 35, April: (2010) 315–322. doi: 10.1557/mrs2010.554.

[64] Martin, S., G. Bryant, and W. van Megen. "Crystallization kinetics of polydisperse colloidal hard spheres: Experimental evidence for local fractionation." *Physical Review E* 67, 6: (2003) 1–11. doi: 10.1103/PhysRevE.67.061405.

[65] Martinez, V. A., R. Besseling, O. A. Croze, J. Tailleur, M. Reufer, J. Schwarz-Linek, L. Wilson, M. A. Bees, and W. C. K. Poon. "Differential dynamic microscopy: A high-throughput method for characterizing the motility of microorganisms." *Biophysical journal* 103, 8. doi: 10.1016/j.bpj.2012.08.045. (2012).

[66] Martinez, V. A., G. Bryant, and W. van Megen. "Slow dynamics and aging of a colloidal hard sphere glass." *Physical Review Letters* 101, 13: (2008) 1–4. doi: 10.1103/PhysRevLett.101.135702.

[67] McRae, R., and a. D. J. Haymet. "Freezing of polydisperse hard spheres." *The Journal of Chemical Physics* 88, 2: (1988) 1114. doi: 10.1063/1.454230.

[68] van Megen, W., and S. R. Williams. "Comment on "Probing the equilibrium dynamics of colloidal hard spheres above the mode-coupling glass transition"." *Physical Review Letters* 104, 16: (2010) 169,601. doi: 10.1103/PhysRevLett.104.169601.

[69] Michler, G. "Problems Associated with the Electron Microscopy of Polymers." In *Electron Microscopy of Polymers*, Springer Berlin Heidelberg, 2008, 175–183.

[70] Miracle, D. B. "A structural model for metallic glasses." *Nature materials* 3, 10: (2004) 697–702. doi: 10.1038/nmat1219.

[71] Miracle, D. B., D. V. Louzguine-Luzgin, and A. Inoue. "An assessment of binary metallic glasses: correlations between structure, glass forming ability and stability." *International Materials Reviews* 55, 4: (2010) 218–256. doi: 10.1179/095066010X12646898728200.

[72] Pandey, R., and D. Tripathi. "Schulz distribution function and the polydispersity of the binary suspension of charged macroions." *Colloids and Surfaces A: Physicochemical and Engineering Aspects* 190, 3: (2001) 217–227. doi: 10.1016/S0927-7757(01)00707-5.

[73] Paulin, S., and B. Ackerson. "Observation of a phase transition in the sedimentation velocity of hard spheres." *Physical review letters* 64, 22: (1990) 2663–2666. doi: 10.1103/PhysRevLett.64.2663.

[74] Pedersen, J. S. *Neutrons, x-rays and light: scattering methods applied to soft condensed matter*. Amsterdam: North-Holland Elsevier, 2002.

[75] Peker, A., and W. L. Johnson. "A highly processable metallic glass: Zr41.2Ti13.8Cu12.5Ni10.0Be22.5." *Applied Physics Letters* 63, 17: (1993) 2342. doi: 10.1063/1.110520.

[76] Perrin, J. *Brownian Movement and Molecular Reality*. London: Taylor and Francis, 1910, translated edition.

[77] Pham, K. N., S. U. Egelhaaf, P. N. Pusey, and W. C. K. Poon. "Glasses in hard spheres with short-range attraction." *Physical Review E* 69: (2004) 011,503. doi: 10.1103/PhysRevE.69.011503.

[78] Phan, S.-E., W. B. Russel, J. Zhu, and P. M. Chaikin. "Effects of polydispersity on hard sphere crystals." *The Journal of Chemical Physics* 108, 23: (1998) 9789. doi: 10.1063/1.476453.

[79] Poon, W. C. K. "Colloids as Big Atoms." *Science* 304: (2004) 830. doi: 10.1126/science.1097964.

[80] Poon, W. C. K., A. Pirie, M. Haw, and P. N. Pusey. "Non-equilibrium behaviour of colloid-polymer mixtures." *Physica A: Statistical and Theoretical Physics* 235, 1-2: (1997) 110–119. doi: 10.1016/S0378-4371(96)00332-9.

[81] Poon, W. C. K., A. D. Pirie, and P. Pusey. "Gelation in colloid-polymer mixtures." *Faraday Discussions* 101: (1995) 65. doi: 10.1039/fd9950100065.

[82] Poon, W. C. K., L. Starrs, S. P. Meeker, A. Moussaïd, R. M. L. Evans, P. N. Pusey, and M. M. Robins. "Delayed sedimentation of transient gels in colloid-polymer mixtures: dark-field observation, rheology and dynamic light scattering studies." *Faraday Discussions* 112, 2: (1999) 143–154. doi: 10.1039/A900664H.

[83] Poon, W., J. Selfe, M. B. Robertson, S. M. Ilett, A. D. Pirie, and P. N. Pusey. "An experimental study of a model colloid-polymer mixture." *Journal de Physique II* 3: (1993) 1075. doi: 10.1051/jp2:1993184.

[84] Poon, W., E. R. Weeks, and C. P. Royall. "On measuring colloidal volume fractions." *Soft Matter* 8, 1: (2012) 21. doi: 10.1039/c1sm06083j.

[85] Puertas, A. M., M. Fuchs, and M. E. Cates. "Dynamical heterogeneities close to a colloidal gel." *The Journal of chemical physics* 121, 6: (2004) 2813–22. doi: 10.1063/1.1768936.

[86] Pusey, P. N. "The effect of polydispersity on the crystallization of hard spherical colloids." *Journal de Physique* 48: (1987) 709–712. doi: 10.1051/jphys:01987004805070900.

[87] Pusey, P. N. *Neutrons, x-rays and light: scattering methods applied to soft condensed matter*. Amsterdam: North-Holland Elsevier, 2002.

[88] Pusey, P. N., and W. van Megen. "Phase behaviour of concentrated suspensions of nearly hard colloidal spheres." *Nature* 320, 6060: (1986) 340–342. doi: 10.1038/320340a0.

[89] Pusey, P. N., E. Zaccarelli, C. Valeriani, E. Sanz, W. C. K. Poon, and M. E. Cates. "Hard spheres: crystallization and glass formation." *Philosophical transactions. Series A, Mathematical, physical, and engineering sciences* 367, 1909: (2009) 4993–5011. doi: 10.1098/rsta.2009.0181.

[90] Rayleigh, L. "The incidence of light upon a transparent sphere of dimensions comparable with the wave-length." *Proceedings of the Royal Society of London A* , 84. doi: 10.1098/rspa.1910.0054.

[91] Reiss, H., H. L. Frisch, and J. L. Lebowitz. "Statistical mechanics of rigid spheres." *The Journal of Chemical Physics* 31, 2: (1959) 369. doi: 10.1063/1.1730361.

[92] Rieker, T., A. Hanprasopwattana, Aand Datye, and P. Hubbard. "Particle size distribution inferred from small-angle x-ray scattering and transmission electron microscopy." *Langmuir* , 7: (1999) 638–641. doi: 10.1021/la9810713.

[93] Roerdink, J. B. T. M., and A. Meijster. "The watershed transform: definitions, algorithms and parallelization strategies." *Fundamenta Informaticae* 41: (2000) 1–40.

[94] Royall, C. P., W. C. K. Poon, and E. R. Weeks. "In search of colloidal hard spheres." *Soft Matter* 9, 1: (2013) 17. doi: 10.1039/c2sm26245b.

[95] Sanders, J. V. "Close-packed structures of spheres of two different sizes. I. Observations on natural opal." *Philosophical Magazine A* 42, 6: (1980) 705–720. doi: 10.1080/01418618008239379.

[96] Schatzel, K. "Suppression of multiple scattering by photon cross-correlation techniques." *Journal of Modern Optics* 38, 9: (1991) 1849–1865. doi: 10.1016/S1359-0294(99)00036-9.

[97] Schindelin, J., I. Arganda-Carreras, E. Frise, V. Kaynig, M. Longair, T. Pietzsch, S. Preibisch, C. Rueden, S. Saalfeld, B. Schmid, J.-Y. Tinevez,

D. J. White, V. Hartenstein, K. Eliceiri, P. Tomancak, and A. Cardona. "Fiji: an open-source platform for biological-image analysis." *Nature Methods* 9, 7: (2012) 676–82. doi: 10.1038/nmeth.2019.

[98] Schneider, C. A., W. S. Rasband, and K. W. Eliceiri. "NIH Image to ImageJ: 25 years of image analysis." *Nature Methods* 9, 7: (2012) 671–675. doi: 10.1038/nmeth.2089.

[99] Schofield, A. B., P. N. Pusey, and P. Radcliffe. "Stability of the binary colloidal crystals AB2 and AB13." *Physical Review E* 72, 3: (2005) 1–10. doi: 10.1103/PhysRevE.72.031407.

[100] Schofield, A., P. Pusey, R. Christianson, U. Gasser, A. Bailey, V. Prasad, S. Manley, P. Segre, L. Cipelletti, D. Weitz, M. Doherty, S. Sankaran, A. Jankovsky, B. Shiley, J. Bowen, K. Dendorfer, J. Eggers, J. Koudelka, C. Kurta, and T. Lorik. "AB6 Binary Crystal Structures.", 2002. Unpublished.

[101] Schofield, A. B. `http://www2.ph.ed.ac.uk/~abs/Phasediagrams.html`, . Accessed: 20-9-2013.

[102] Schöpe, H. J., G. Bryant, and W. van Megen. "Small changes in particle-size distribution dramatically delay and enhance nucleation in hard sphere colloidal suspensions." *Physical Review E* 74, 6: (2006) 1–4. doi: 10.1103/PhysRevE.74.060401.

[103] Schöpe, H. J., G. Bryant, and W. van Megen. "Effect of polydispersity on the crystallization kinetics of suspensions of colloidal hard spheres when approaching the glass transition." *The Journal of chemical physics* 127, 8: (2007) 084,505. doi: 10.1063/1.2760207.

[104] Sear, R. "Phase separation and crystallisation of polydisperse hard spheres." *Europhysics Letters* 44, September 1998: (1998) 1–4. doi: 10.1209/epl/i1998-00500-3.

[105] Segre, P. N., W. V. Megen, P. N. Pusey, K. Schatzel, and W. Peters. "Two-colour dynamic light scattering." *Journal of Modern Optics* 42, 9: (1995) 1929–1952. doi: 10.1080/09500349514551681.

[106] Senff, H., and W. Richtering. "Temperature sensitive microgel suspensions: Colloidal phase behavior and rheology of soft spheres." *The Journal of Chemical Physics* 111, 4: (1999) 1705. doi: 10.1063/1.479430.

[107] Sollich, P. "Predicting phase equilibria in polydisperse systems." *Journal of Physics: Condensed Matter* 14: (2002) R79. doi: 10.1088/0953-8984/14/3/201.

[108] Sollich, P., and N. B. Wilding. "Crystalline phases of polydisperse spheres." *Physical Review Letters* 104, 11: (2010) 1–4. doi: 10.1103/PhysRevLett.104.118302.

[109] Sollich, P., and N. B. Wilding. "Polydispersity induced solid-solid transitions in model colloids." *Soft Matter* 7, 9: (2011) 4472. doi: 10.1039/C0SM01367F.

[110] Sollich, P., and M. Cates. "Projected free energies for polydisperse phase equilibria." *Physical Review Letters* 80, 7: (1998) 1365–1368. doi: 10.1103/PhysRevLett.80.1365.

[111] Spahn, P., C. E. Finlayson, W. M. Etah, D. R. E. Snoswell, J. J. Baumberg, and G. P. Hellmann. "Modification of the refractive-index contrast in polymer opal films." *Journal of Materials Chemistry* 21, 24: (2011) 8893. doi: 10.1039/c1jm00063b.

[112] Starrs, L., W. C. K. Poon, D. J. Hibberd, and M. M. Robins. "Collapse of transient gels in colloid-polymer mixtures." *Journal of Physics: Condensed Matter* 14, 10: (2002) 2485. doi: 10.1088/0953-8984/14/10/302.

[113] Torquato, S., and F. H. Stillinger. "Jammed hard-particle packings: From Kepler to Bernal and beyond." *Reviews of Modern Physics* 82, 3: (2010) 2633–2672. doi: 10.1103/RevModPhys.82.2633.

[114] Trizac, E., M. D. Eldridge, and P. Madden. "Stability of the AB crystal for asymmetric binary hard sphere mixtures." *Molecular Physics* 90, 4: (1997) 675–678. doi: 10.1080/00268979709482651.

[115] Tummers, B. "DataThief III.", 2006. `<http://datathief.org/>`.

[116] Urban, C., and P. Schurtenberger. "Characterization of turbid colloidal suspensions using light scattering techniques combined with cross-correlation methods." *Journal of Colloid and Interface Science* 207, 1: (1998) 150–158. doi: 10.1006/jcis.1998.5769.

[117] Warren, P. B. "Phase transition kinetics in polydisperse systems." *Physical Chemistry Chemical Physics* 1, 9: (1999) 2197–2202. doi: 10.1039/a809828j.

[118] Warren, P. "Phase behavior of a colloid + binary polymer mixture: theory." *Langmuir* 7463, 16: (1997) 4588–4594. doi: 10.1021/la970198.

[119] Whiteflash. `http://www.whiteflash.com/about-diamonds/jewelry/black-opal-gemstone-fireworks.htm`, . Accessed: 16-08-2013.

[120] Widom, B. "Intermolecular forces and the nature of the liquid state." *Science* 157, 3787: (1967) 375–382.

[121] Wilding, N. B., and P. Sollich. "Phase behavior of polydisperse spheres: simulation strategies and an application to the freezing transition." *The Journal of Chemical Physics* 133, 22: (2010) 224,102. doi: 10.1063/1.3510534.

[122] Yethiraj, A., and A. Van Blaaderen. "A colloidal model system with an interaction tunable from hard sphere to soft and dipolar." *Nature* 421, 6922: (2003) 513–517. doi: 10.1038/nature01376.1.

[123] Zaccarelli, E., S. Liddle, and W. C. K. Poon. "On polydispersity and the hard-sphere glass transition." *in preparation* .

[124] Zhang, I., C. P. Royall, M. a. Faers, and P. Bartlett. "Phase separation dynamics in colloid polymer mixtures: the effect of interaction range." *Soft Matter* 9, 6: (2013) 2076. doi: 10.1039/c2sm27119b.

[125] Zheng, M., A. Jagota, E. D. Semke, B. a. Diner, R. S. McLean, S. R. Lustig, R. E. Richardson, and N. G. Tassi. "DNA-assisted dispersion and separation of carbon nanotubes." *Nature materials* 2, 5: (2003) 338–42. doi: 10.1038/nmat877.

[126] Zhu, J., M. Li, R. Rogers, and W. Meyer. "Crystallization of hard-sphere colloids in microgravity." *Nature* 387, June: (1997) 1996–1998.